MECHANICAL BEHAVIOR OF FRICTION STIR PROCESSED Mg ALLOY

Ph.D. THESIS

by

RAJA A

DEPARTMENT OF METALLURGICAL & MATERIALS ENGINEERING
INDIAN INSTITUTE OF TECHNOLOGY ROORKEE
ROORKEE- 247667, INDIA
JULY, 2018

MECHANICAL BEHAVIOR OF FRICTION STIR PROCESSED Mg ALLOY

A THESIS

Submitted in partial fulfilment of the
requirements for the award of the degree

of

DOCTOR OF PHILOSOPHY

in

METALLURGICAL & MATERIALS ENGINEERING

by

RAJA A

DEPARTMENT OF METALLURGICAL & MATERIALS ENGINEERING
INDIAN INSTITUTE OF TECHNOLOGY ROORKEE
ROORKEE- 247667, INDIA
JULY, 2018

INDIAN INSTITUTE OF TECHNOLOGY ROORKEE ROORKEE

CANDIDATE’S DECLARATION

I hereby certify that the work which is being presented in the thesis entitled **“MECHANICAL BEHAVIOR OF FRICTION STIR PROCESSED Mg ALLOY”,** in partial fulfilment of the requirements for the award of the Degree of Doctor of Philosophy and submitted in the Department of Metallurgical & Materials Engineering of the Indian Institute of Technology Roorkee, Roorkee, is an authentic record of my own work ingeniously carried out during the period from July, 2013 to July, 2018 under the supervision of Dr. Vivek Pancholi, Associate Professor, Department of Metallurgical and Materials Engineering, Indian Institute of Technology Roorkee, Roorkee.

The matter presented in the thesis has not been submitted by me for the award of any other degree of this or any other institute.

(RAJA A)

This is to certify that the above statement made by the candidate is correct to the best of my knowledge.

Dated: _____________

(Vivek Pancholi)
Supervisor

DEDICATION

I am dedicating this thesis

with love and affection **TO MY MOTHER** *who is a retired nurse,*

enjoyed her past ages serving thousands of mothers to bring their children

to the world.

ACKNOWLEDGEMENTS

Thanks to Avvaiyar, a prominent poetess of Tamil literature and her poignant quote *“கற்றது கையளவு, கல்லாதது உலகளவு”*, which is to be read as “*katrathu kaialavu kallathathu ulagalavu”*. It means “what is learnt is just fistful, what is not learnt, is the size of the world” which created a quest to learn, always. The learning habit helped me to develop myself as a researcher. My first research article was published on my father’s death anniversary, May 1st, 2017, might be his blessing and must be an auspicious beginning. Thanks to my father, Mr. M.P. Allavikutty, for his love and support. He would be happy to see me, what I am doing now and how I am proceeding in my life. I am really glad to acknowledge my mother and sister Laitha and Seema, it would have been impossible to complete my thesis without their strength, courage, love and support.

I am indebted to express my gratitude and veneration to my respected supervisor Dr. Vivek Pancholi, Associate Professor, Department of Metallurgical and Materials Engineering, Indian Institute of Technology, Roorkee for his valuable guidance at different stages of this research program. His working principle and moto of IIT Roorkee are one and the same, *“श्रमम् विना न किमपि साध्यम्” (“śramam vinā na kimapi sādhyam”)* which means “Without effort, nothing is possible”. Hard work, it helped me to get my research works published in good journals. His able guidance, helped me to carry out my research work systematically and give a final shape to the thesis.

It is a great privilege for me to pay my deep gratitude to Prof. B.K. Mishra, Department of Mechanical and Indsutrial Engineering, Indian Institute of Technology, Roorkee for his valuable guidance on fracture mechanics related work and Dr. K.S. Suresh, Assistant Professor, Department of Metallurgical and Materials Engineering, Indian Institute of Technology, Roorkee for his valuable discussions and guidance on texture analysis.

I express my deepest sense of reverence and indebtedness to the Head, Department of Metallurgical and Materials Engineering and esteemed members of my SRC committee Prof. Ujjwal Prakash (SRC and DRC Chairman), Department of Metallurgical and Materials Engineering, Indian Institute of Technology, Roorkee, Dr. Vikram Dabhade (internal expert), Associate Professor, Department of Metallurgical and Materials Engineering, Indian Institute of Technology, Roorkee, Prof. D.K. Dwivedi (external expert), Department of Mechanical and

Industrial Engineering, Indian Institute of Technology, Roorkee and Prof. B.S.S.Daniel, Department of Metallurgical and Materials Engineering, Indian Institute of Technology, Roorkee for their valuable suggestions and eternal encouragement in all my research endeavors. I thank all the faculty members of the Department of Metallurgical and Material Engineering and non – teaching staffs, for generously providing various research related resources and for maintaining the experimental facilities.

A very special gratitude to Prof. R. Jayaganthan, Department of Engineering Design, Indian Institute of Technology, Madras, Dr. P. Gopinath, Associate Professor, Department of Biotechnology, Indian Institute of Technology, Roorkee and Dr. M. Sankar, Associate Professor, Department of Chemistry, Indian Institute of Technology, Roorkee for their support and motivation during the research period.

I am also grateful to Mr. S.P. Madhavan, Manager, Foundry and Forging Division, Hindustan Aeronautics Limited, Bangalore, India, for generously providing AZ91 alloys for this research work. He was one of the brother I made here in Indian Institute of Technology during my Masters along with Mr. G. Chandramohan, Mr. V. Vickranandh, Mr. K. Jayakanthan and Mr. P.Raja. Thank you to all for your friendliness and motivation.

I learned things and worked mutually with my colleagues Guru Prakash, Rahul Gupta, Dr. Devasri Fuloria, Sudhir, Ravi, Gurujinder, Vinod, Sathiesh and lab mates Suresh Sonkar, Rahul Kumar and Anirudh Malakar, who helped me to work easily in the labs and department. My benevolent thanks to them and all other research scholars in the Metallurgical and Materials Engineering Department. A special thanks to my brother and friend S. Raj Kumar, research scholar at Center of Nanotechnology, IIT Roorkee and all my dear friends elsewhere for their support.

A memorable thanks to Mr. V. Dhanasekaran, Senior SAP Enterprise Asset Management Consultant, Alfanar, Saudi Arabia who helped me to select my course during my undergraduate admission counselling at Regional College of Engineering, Trichy (present day National Institute of Technology, Trichy). I am extremely grateful to my friend indeed, Dr. Chandan Kumar Pandey, M.B.B.S and his family, who generously helped me financially for course registration on the very first day of my undergraduate way back in 2002, at College of Engineering Guindy, Anna University, which paved me the path to pursue Ph.D.

While we try to teach our children all about life, our children teach us what life is all about. I am thankful to my cousin, R.V. Raghul, 14 years old, who is inquisitive about my work while I taught him, his homework and it helped me to understand things while finding answers to his questions. I am thankful to all other brothers and students, whom I had taught, supported and learned.

Last but not the least, I am grateful for your love, for your support, for your integrity, for Pallavi Gupta.

RAJA A

ABSTRACT

Microstructure having mixture of coarse and fine grained microstructure (bimodal or layered) in Al and few wrought Mg alloys were reported to exhibit superior mechanical properties when compared to the homogeneously fine grained microstructure but such studies were not carried out in as-cast Mg alloys. Motivated by the gap in the literature, layered microstructure containing fine grain and as-cast microstructure was generated using friction stir processing (FSP) and its effect on mechanical behavior was studied in this work. Preliminary studies were carried out on the tensile and fracture toughness behavior of as-cast material in solutionized (T4) and aged (T6) conditions. Then, layered microstructure with the mixture of fine grain and as-cast microstructure was obtained by multipass friction stir processing (FSP) using three tools with different pin lengths. Change in the as-cast microstructure after FSP, as well as effect of the tool pin length on the FSPed microstructure were analyzed before studying the effect of layered microstructure on the mechanical behavior of the material. Finally, a constitutive equation was developed for the superplasticity of FSPed AZ91 Mg alloy and its parameters are correlated with the microstructural evolution happened during the superplastic deformation.

In the preliminary study on as-cast material, the alloy was heat treated to 416ºC for 48 hours and air quenched to get T4 condition (solutionized). Further, T4 solution treated alloy was heat treated at 167ºC for 24 hours and air quenched, to get T6 condition (solutionized and aged). The tensile test and fracture toughness test of AZ91 alloy in as-cast, T4 and T6 conditions were carried out. The tensile tests showed improvement in strength from approximately 80 MPa in cast alloy to 132 MPa in T4 condition and the corresponding improvement in ductility from 0.8% to 4.7%. After aging (T6 condition) the strength remains almost same, 130 MPa, but the ductility reduced to 2%. The tensile fractographs of as-cast and T6 samples exhibited cleavage facets and river patterns while T4 samples exhibited quasi-cleavage fracture morphology. The fracture toughness was measured using J-integral method. The J_{IC} value increased from 1.7 kJ/m^2 in as-cast material to 4.2 kJ/m^2 after solution treatment but reduced to 3.2 kJ/m^2 after aging. Crack bridging due to second phase particles was observed in the fatigue pre-crack regions. Precipitate/matrix interface resists crack growth at the crack front. This resistance force decides the fracture toughness of the samples.

After studying the mechanical behavior of cast material, multipass FSP was performed using tools with different pin lengths. Three tools: PL_4 with 4 mm pin length, PL_5 with 5 mm pin length and PL_7 with 7 mm pin length, were used. The effect of tool pin length on the microstructure and tensile properties were studied. Three zones were observed from the processed regions. ZONE I was only affected by the tool shoulder, ZONE II was influenced by both the shoulder and the pin while ZONE III was affected only by the tool pin. ZONE I and ZONE II were present in the processed region of the samples FSPed using all the three tools. Semi-circular ring patterns were observed at ZONE III in samples processed using tools PL_5 and PL_7. ZONE III was absent in the material processed by tool PL_4. There were no differences in the phases formed and their distribution after process using the three tools. The tensile strength increased from 290 MPa in tensile sample processed by tool PL_4 to 340 MPa in tensile sample processed by tool PL_7 and the ductility remains nearly same in all the cases. The results confirmed that the variations in the properties with increasing thickness of the processed region was insignificant. It ensures that the properties of layered microstructure (in subsequent chapters) can be analyzed considering similarity in the processed region using three tools with different pin length.

Three kinds of layered microstructures was generated through the thickness of the material, namely, HFG, SFG and FFG by multipass FSP. Its effect on room temperature mechanical behavior were studied. Tensile test, notch fracture toughness test and high cycle fatigue test were conducted to understand the effect of layered microstructure on mechanical properties. The tensile properties, namely, yield strength, tensile strength and percentage elongation of AC material were found to be 92 MPa, 100 MPa and 0.8% respectively and the corresponding values for FFG were found to improve to 242 MPa, 327 MPa and 4.7%. For HFG and SFG, these values were found to follow the rule of mixture. Grain size strengthening as well as solid solution strengthening have contributed in improvement of the strength after FSP. The fracture morphology was intragranular cleavage in as-cast region and intergranular in FSPed region. The apparent fracture toughness (K_Q) values of single edge notch bend (SENB) samples without precrack were compared, and the results showed improvement from 6.2 MPa$\sqrt{m}$ in AC to 12.3 MPa$\sqrt{m}$ in FFG material. SFG material showed pop-in phenomenon as crack originated from the as-cast region was arrested by the tougher FSPed region on both the surfaces. Number cycles to failure during high cycle fatigue also found to increase with the increase in FSPed region.

To study the effect of layered microstructures (HFG, SFG and SFG) on the superplastic behavior high temperature tensile tests were carried out at 350 °C using three different initial strain rates i.e. 5×10^{-3} s^{-1},1×10^{-3} s^{-1} and 5×10^{-4} s^{-1}. The FFG material showed superplasticity at all strain rates and highest ductility of 680 % was achieved at the strain rate of 5×10^{-4} s^{-1}. The AC and HFG material displayed very low elongation while SFG material exhibited superplasticity of 388 %. The superplastic behaviour in SFG was due to increase in the fraction of fine grain microstructure and modification of as-cast microstructure on both the surfaces. Microstructure and texture studies revealed that grain boundary sliding accommodated by grain boundary migration and grain rotation were responsible for superplasticity in FSPed region.

The constitutive equation for the superplasticity of full thickness fine grained material was developed using tensile data of the high temperature deformation performed at temperatures (150 °C, 250 °C and 350 °C) and at three different strain rates (5 x 10^{-3} s^{-1}, 1 x 10^{-3} s^{-1} and 5 x 10^{-4} s^{-1}). Maximum elongation of 818 % was observed at 250 ºC and at a strain rate of 1 x 10^{-3} s^{-1}. Strain hardening was observed in the flow behavior of samples tested at 250 ºC and 350 ºC. Variation in parameters of the constitutive equation with increasing strain were observed. The strain hardening observed at 250 ºC, at a strain rate of 5 x 10^{-4} s^{-1} and at 350 ºC, at the strain rates of 1 x 10^{-3} s^{-1} and 5 x 10^{-4} s^{-1} was attributed to dynamic grain growth caused by GBS. Thus the variation in material parameters with increasing strain was due to the non-steady flow caused by dynamic grain growth during superplastic deformation in FSPed AZ91 Mg alloy.

LIST OF PUBLICATIONS

International Referred Journals

From thesis work

1. ***A Raja***, P. Biswas, V. Pancholi, "Effect of layered microstructure on the superplasticity of friction stir processed AZ91 Mg alloy", Material science and engineering A,vol.725, pp. 492-502, *2018*.
2. ***A. Raja***, V. Pancholi, "Effect of friction stir processing on tensile and fracture behaviour of AZ91 alloy," J. Mater. Process. Technol., vol. 248, pp. 8–17, 2017
3. ***A. Raja***, V. Pancholi, "Superplastic constitutive equation of friction stir processed AZ91 Mg alloy", (to be communicated).
4. ***A. Raja***, P. Kumar, V. Pancholi, "Fracture toughness evaluation of AZ91 Mg alloy" (to be communicated).

Other works

5. V. Pancholi, ***A. Raja***, and K. Rohit, "Deformation Behavior of Inhomogeneous Layered Microstructure," Mater. Sci. Forum, vol. 879, pp. 1437–1442, 2017.
6. V. Pancholi, K. Rohit, and ***A. Raja***, "Effect of Different Proportion of Coarse and Fine Grain Microstructure on Superplastic Forming Characteristics," Mater. Sci. Forum, vol. 838–839, pp. 528–533, 2016.

Conference proceedings

1. ***A. Raja***, V. Pancholi, and B. K. Mishra, "Layered Microstructure Generated by Multipass Friction Stir Processing in AZ91 Alloy and Its Effect on Fatigue Characteristics," in Proceedings of Fatigue, Durability and Fracture Mechanics, Springer, Singapore, pp. 213–222, 2018.

Conferences

From thesis work

1. ***A. Raja***, P. Kumar, V. Pancholi, “Crack resistance behaviour of AZ91 Mg alloy”. BITS Pilani Goa campus, NMD – ATM conference, Goa, India, 2017.
2. ***A. Raja***, V. Pancholi, “Influence of microstructural variation on the strengthening mechanisms of AZ91 Mg alloy produced by multipass friction stir processing (FSP)”. IIT Kanpur, NMD – ATM conference, Kanpur, India, 2016.
3. ***A. Raja***, B. K. Mishra, V. Pancholi, “Layered microstructure generated by multipass friction stir processing in AZ91 alloy and its effect on fatigue characteristics”. Institute of Structural Integrity and Failure Studies, Fatigue Durability - International conference, IISc Bangalore, India, 2016.

Other works

4. ***A. Raja***, V. Pancholi, “EBSD coupled in-situ tensile test of Al 5052 alloy”. BITS Pilani Goa campus, NMD – ATM conference, Goa, India, 2017.
5. A. Patel, ***A. Raja***, V. Pancholi, “Effect of number of passes on the wear behavior of friction stir processed AZ91/SiC surface composite”. IIT Roorkee, AMPCO International conference, Roorkee, India, 2017.
6. Anurag, ***A. Raja***, V. Pancholi, “Circular friction stir processing, microstructural variations and its effect on thinning factor during superplastic bulge formation of Al 5086 alloy”. IIT Bombay, SMF conference, Mumbai, India 2016.
7. V. Kumar, ***A. Raja***, V. Pancholi, “Study on thickness variation during superplastic forming of Friction Stir Processed Al -5086 alloy”. IIT Roorkee, PFAM XXIII International conference, Roorkee, India, December 2014.

TABLE OF CONTENTS

Page No.

ACKNOWLEDGEMENTS i

ABSTRACT v

LIST OF PUBLICTIONS ix

TABLE OF CONTENTS xi

LIST OF FIGURES xvii

LIST OF TABLES xxiii

LIST OF ABBREVIATIONS xxv

LIST OF SYMBOLS xxvii

Chapter 1: INTRODUCTION 01

Chapter 2: LITERATURE REVIEW 09

2.1 Magnesium and its alloys 11

2.2 AZ91 Mg alloy 13

- 2.2.1 Chemical composition 13
- 2.2.2 Mechanical properties 14
- 2.2.3 Strengthening mechanisms 15
  - 2.2.3.1 Grain size strengthening 15
  - 2.2.3.2 Solid solution strengthening 16
  - 2.2.3.3 Orowan strengthening 16
- 2.2.4 Deformation mechanisms 17

2.3 Friction stir processing (FSP) 21

2.4 Factors influencing FSP 22

- 2.4.1 Tool material 22

  2.4.2 Tool design 23
  2.4.3 Process parameters 25
  2.4.4 Pre-heating and cooling 26
  2.4.5 Multipass FSP 27
2.5 FSPed microstructure 29
2.6 Deformation mechanism responsible for FSPed microstructure 30
2.7 Influence of FSP on mechanical properties 31
  2.7.1 Tensile properties 31
  2.7.2 Fracture toughness 34
  2.7.3 Fatigue 34
  2.7.4 Superplasticity 35
2.8 Property enhancement by grain size inhomogeneous microstructure 37
2.9 Summary of literature review 38
2.10 Literature gap 39
2.11 Objective 39
Chapter 3: MATERIAL AND METHODS 41
3.1 Material 43
3.2 Solutionizing and aging of as-cast alloy 43
3.3 Multipass FSP 44
3.4 Mechanical testing 45
  3.4.1 Room temperature tensile test 45
  3.4.2 Fracture toughness test 46
  3.4.3 Fatigue test 47
  3.4.4 High temperature tensile test 48
3.5 Material characterization 48

Chapter 4: MECHANICAL BEHAVIOR OF AS-CAST MATERIAL 51

4.1 Results 53

- 4.1.1 Microstructure 53
- 4.1.2 Tensile properties 56
- 4.1.3 Fracture toughness 58

4.2 Discussion 60

4.3 Conclusions 63

Chapter 5: EFFECT OF TOOL PIN LENGTH ON FSPED MICROSTRUCTURE 65

5.1 Results 67

- 5.1.1 Material flow under the tool 67
- 5.1.2 Microstructure 69
- 5.1.3 Microtexture 71
- 5.1.4 Phase distribution 72
- 5.1.5 Tensile properties 73

5.2 Discussion 74

- 5.2.1 Semi-circular ring patterns 74
- 5.2.2 FSPed microstructure 75
- 5.2.3 Deformation mechanism and texture 75

5.3 Conclusions 77

Chapter 6: LAYERED MICROSTRUCTURE AND ROOM TEMPERATURE PROPERTIES 79

6.1 Results 81

- 6.1.1 Microstructure 81
- 6.1.2 Tensile properties 82
- 6.1.3 Apparent notch fracture toughness 85

    6.1.4 Fatigue 87
6.2 Discussion 89
    6.2.1 Rule of mixture 89
    6.2.2 Strengthening mechanisms 90
    6.2.3 Fracture morphology and elongation 91
    6.2.4 Fracture toughness behavior 92
6.3 Conclusions 93
CHAPTER 7: LAYERED MICROSTRUCTURE AND SUPERPLASTICITY 95
7.1 Results 97
    7.1.1 Microstructure post friction stir processing 97
    7.1.2 Superplastic deformation 98
    7.1.3 Strain rate sensitivity 99
    7.1.4 Fracture surfaces 101
    7.1.5 Microstructure and texture after superplastic deformation 102
7.2 Discussion 104
    7.2.1 Superplastic behavior of inhomogeneous microstructure 104
    7.2.2 Deformation mechanism 106
7.3 Conclusions 108
Chapter 8: CONSTITUTIVE EQUATION 109
8.1 Results 111
    8.1.1 Superplastic deformation 111
    8.1.2 Strain rate sensitivity 113
    8.1.3 Stress exponent 114
    8.1.4 Activation energy 116
    8.1.5 Constitutive equation 117

8.2 Discussion 118

8.3 Conclusions 121

Chapter 9: CONCLUSIONS AND SUGGESTIONS FOR FUTURE WORK 123

References 129

LIST OF FIGURES

Fig. No.	Title	Page No.
Fig. 1.1	(a) Magnesium production from 2002 to 2014, (b) World motor vehicle production from 1950 to 2013, (c) Global greenhouse gas emissions by sectors and (d) Global CO2 emission by countries.	3
Fig. 1.2	Typical yield strength and elongation of some metal alloys	5
Fig. 2.1	Mg-Al binary phase diagram	13
Fig. 2.2	Slip systems in Mg (a) basal slip, (b) prismatic slip and (c) pyramidal slips	17
Fig. 2.3	(a) tensile twin and (b) compression twin	18
Fig. 2.4	Schematic of FSP	21
Fig. 2.5	FSP tool shoulder shapes and features	23
Fig. 2.6	(a) tool diameter versus workpiece thickness and (b) relation between tool diameters (pin and shoulder)	24
Fig. 2.7	FSPed region on AZ91 alloy showing stretched stir zone on advancing side and retreating side without any stretch zone	28
Fig. 2.8	Macrostructure of multipass FSPed plate showing overlapping towards (a) retreating side and (b) advancing side	29
Fig. 2.9	Stress–strain curves of as-cast and friction stir-processed AZ91 Mg alloy	33
Fig. 2.10	Microstructural collage of layered microstructure in ZK60 Mg alloy generated by multipass FSP.	37
Fig. 3.1	Schematic temperature profile of T4 and T6 treatment	43
Fig. 3.2	Schematic of multipass FSPed plate with location of tensile sample for room temperature tensile test	45
Fig. 3.3	(a) SENB specimen for fracture toughness test, and (b) notch details	46
Fig. 3.4	SENB specimen geometry generated for XFEM analysis (a) showing meshes with 4 node quadrilateral element and (b) showing fatigue pre-crack position and boundary conditions	46

Fig. 3.5 Continuous fillet fatigue sample 47

Fig. 3.6 Schematic of multipass FSPed plate with location of tensile sample for high temperature tensile test 48

Fig. 4.1 Microstructure of as-cast AZ91 Mg alloy (a) optical image, (b) secondary electron image showing dendritic region (A) and interdendritic region (B). 53

Fig. 4.2 Microstructures of T4 solution treated samples obtained after holding different time at 416ºC and air cooled. 54

Fig. 4.3 Microstructures of T6 heat treated samples obtained after different holding time at 167ºC and air cooled 55

Fig. 4.4 Optical microstructures of AZ91 Mg alloys in (a) as-cast and after (b) T4, and (c) T6, heat treatment 56

Fig. 4.5 True stress versus true strain curve of the material in as-cast, T4 and T6 conditions. 57

Fig. 4.6 Fractograph of tensile tested specimen with cleavage facets indicated by solid arrows in (a) as-cast, (b) quasi cleavage by long-dashed arrows in T4 condition (c) river patterns by short-dashed arrow inT6 condition. 57

Fig. 4.7 Load vs. LLD curve of (a) as-cast, (b) T4 & (c) T6 and J vs. Δa curve of (d) as-cast, (e) T4 & (f) T6 sample. 58

Fig. 4.8 Finite element analysis of strain distribution at the crack tip of (a) as-cast (b) T4 and (c) T6, SENB samples. 60

Fig. 4.9 Schematic illustration of extrinsic and intrinsic damage/toughening mechanism 61

Fig. 4.10 T4 condition; (a) Crack path after J-integral test, (b) crack-tip, (c) fatigue pre-crack propagation through brittle dendrites and crack bridging by precipitates and (d) crack origin 61

Fig. 4.11 T6 condition; (a) Crack path after J-integral test, (b) crack-tip, (c) fatigue pre-crack propagation cutting the brittle dendrites and crack bridging by precipitates and (d) crack origin. 62

Fig. 5.1 Schematic of multipass FSPed plate showing processed region along the transverse direction (Y-direction) and along the process direction (X-direction). 67
Fig. 5.2 Stitched optical images showing inhomogeneity in the microstructure in XZ plane of FSPed region processed by using; (a) PL4, (b) PL5 and (c) PL7. 68
Fig. 5.3 Four distinct microstructure regions observed from macrostructures along the transverse plane a) as cast microstructure, b) FSPed fine grained microstructure; c) microstructure of transition region; d) transition region in higher magnification; e) inhomogeneous microstructured region and f) magnified microstructural inhomogeneities. 69
Fig. 5.4 Phase identification in as-cast and FSPed material by XRD peaks. Disappearance of certain peaks indicate dissolution of second phase in to the matrix. 70
Fig. 5.5 EBSD analysis of FSPed region of sample processed by tool3; (a) Inverse pole figure map, (b) (0001) and $(10\bar{1}0)$ pole figures and (c) grain boundary misorientation distribution 71
Fig. 5.6 SEM image of the samples FSPed by the tools; (a) PL4, (b) PL5 and (c) PL7. 72
Fig. 5.7 Phase analysis by XRD peaks obtained in FSPed regions of samples processed by the three tools. 73
Fig. 5.8 True stress vs. True strain curve of FSPed region obtained from tools with different pin lengths. 74
Fig. 5.9 a) Grain size map, (b) GOS map, (c) IPF map obtained at processed region from transverse plane sample processed by PL5. 76
Fig. 6.1 Macrostructure of (a) AC, (b) HFG, (c) SFG and (d) FFG samples. As-cast microstructure regions, fine grained regions (FG), transition regions and semi-circular ring patterns are mentioned. Arrows x, y and z represent process direction, transverse direction and thickness direction respectively. 82

Fig. 6.2 True stress versus True strain curve of samples with different microstructural configurations. 82

Fig. 6.3 Fractographs of uniaxial tensile tested samples with the fracture surfaces in process plane; (a) AC, (b) HFG, (c) SFG, (d) FFG (e) transcrystalline fracture in as cast region and (f) intergranular fracture in FSPed regions. 83

Fig. 6.4 Optical images of tensile sub-surfaces of (a) AC, (b) HFSP, (c) SFSP and (d) FFSP along the transverse plane which is parallel to the loading axis and FE-SEM images of fracture profile of (e) as-cast region, (f) FSPed region without inhomogeneities and (g) FSPed region with inhomogeneities. 84

Fig. 6.5 Notch fracture toughness test results of samples with different microstructural configurations (a) load vs. crack opening displacement (COD) curve and (b) comparison of apparent notch fracture toughness. 85

Fig. 6.6 Fractograph of SENB samples; (a) AC, (b) HFG, (c) SFG and (d) FFG with their crack origins marked inside the box and respective magnified images in (e)–(h). 86

Fig. 6.7 Fractograph of fatigue tested samples at specific stress amplitudes (a) AC at 40 MPa, (b) AC at 45 MPa, (c) HFG at 40 MPa, and (d) HFG at 45 MPa with (e), (f), (g) and (h) are respective magnified fatigue crack growth regions marked in boxes, similarly (i) SFG at 70 MPA (j) SFG at 80 MPa, (k) FFG at 70 MPa and (l) FFG at 80 MPa while (m), (n), (o) and (p) are respective magnified fatigue growth regions. Dotted arrows indicate inhomogeneities and solid arrows indicate crack growth direction. 88

Fig. 6.8 Comparison of experimental result with the rule of mixture for (a) yield strength and (b) tensile strength. At 0%, 50%, 67% and 100% of FSPed region are indicated as AC, HFG, SFG and FFG samples respectively. 90

Fig. 7.1 Macrostructure of samples; a) AC, b) HFG, c) SFG and d) FFG. The process direction, transverse direction and thickness direction are represented by arrows X, Y and Z respectively. 97

Fig. 7.2 True stress versus true strain curves and corresponding deformed samples after deformation at 350ºC and at strain rates of a) 5×10^{-3} s^{-1}, b) 1×10^{-3} s^{-1} and c) 5×10^{-4} s^{-1}. 99

Fig. 7.3 Fig. 7.3: (a) Flow stress vs. strain rate and (b) elongation vs. strain rate 100

Fig. 7.4 Low magnification fractographs of tensile samples tested at 350ºC and at a strain rate of 1 × 10-3 s-1; (a) AC, (b) HFG, (c) SFG and (d) FFG. Higher magnification fractographs reveal (e) brittle fracture region in AC material, (f) brittle and ductile mix mode fracture regions in AC material, (g) ductile fracture in as-cast region of HFG material, (h) intergranular fracture in FSPed region in HFG material, (i) intergranular fracture in FSPed region of SFG material and (j) fibres due to grain separation at high strain in FFG material 101

Fig. 7.5 IPF maps obtained from EBSD scans of FSPed region in x-z plane close to the fracture surface of tensile tested samples; (a), (b) and (c) are from HFG material, (d), (e) and (f) are from SFG material and (g), (h) and (i) are from FFG material. The ascending order of every material is corresponding to 5×10^{-3} s^{-1}, 1×10^{-3} s^{-1} and 5×10^{-4} s^{-1} 102

Fig. 7.6 IPF maps of deformed samples with tensile axis parallel to process direction (parallel to X-axis shown above) at a strain rate of 5 × 10-4 s-1; (a) AC material with highlighted (yellow) extension twins indicated by arrows in its IPF map and (b) grain boundary misorientation distribution of as-cast material showing predominant tensile twin population around 86.3º, (c) HFG, (d) SFG and (e) FFG 103

Fig. 7.7 Comparison of superplastic elongation in FSPed layered microstructure with the rule of mixture: a) 5×10^{-3} s^{-1}, b) 1×10^{-3} s^{-1} and c) 5×10^{-4} s^{-1}. 105

Fig. 7.8 Pole figures of FSPed region in deformed samples; (a) HFG, (b) SFG and (c) FFG at strain rate of 5×10^{-4} s^{-1} and their corresponding grain boundary misorientation distributions at (d), (e) & (f). 107

Fig. 8.1 True stress vs True strain curves of samples tensile tested at 150 ^{0}C, 250 ^{0}C and 350 ^{0}C and at three different strain rates of 5 × 10-3 s-1, 1 × 10-3 s-1 and 5 × 10-4 s-1 at each temperature. Flow stress behavior with respect to temperature at strain rates; (a) 5 × 10-3 s-1, (b) 1 × 10-3 s-1 and (c) 5 × 10-4 s-1. Flow stress behavior with respect to strain rate at temperatures: (a) 150 °C, (b) 250 °C and (c) 350 °C 112

Fig. 8.2 Elongation versus Temperature at different strain rates 113

Fig. 8.3 a) Plot of ln (σ) vs ln ($\dot{\varepsilon}$) to evaluate m value at a true strain of 0.2 and (b) Plot showing variation of *m* with strain 114

Fig. 8.4 Plots to evaluate stress exponent “n” 115

Fig. 8.5 Variation of stress exponent “n” with true strain 115

Fig. 8.6 Plot of ln (σ) vs 1000/T at a true strain of 0.2 to find the slope and calculate activation energy 117

Fig. 8.7 Variation of activation energy with strain during the superplastic deformation at (a) 250°C and (b) 350°C 117

Fig.8.8 Optical microstructure at the fractured tip and at grip of the sample tensile tested at 150°C and at a strain rate of 5×10^{-4} s^{-1}. 119

Fig. 8.9 Optical microstructures at the fractured tip and at grip of the samples tensile tested at 250°C 120

Fig. 8.10 Optical microstructures at the fractured tip and at grip of the samples tensile tested at 350°C 120

LIST OF TABLES

Table No.	Title	Page No.
Table 2.1	Alloying elements of Mg and its effect	12
Table 2.2	Slip systems in Mg	17
Table 2.3	Key benefits of FSW/FSP	20
Table 2.4	Tensile properties of as-cast and FSPed AZ80 Mg alloy	32
Table 2.5	Literature data on high temperature superplasticity of AZ91 alloy	36
Table 3.1	Experimental conditions used to obtain microstructural variation in through thickness direction to study room temperature mechanical behavior	44
Table 3.2	Experimental conditions used to obtain microstructural variation in through thickness direction to study high temperature mechanical behavior (superplasticity)	45
Table 4.1	Elemental distribution in dendrites and interdendrites of as-cast AZ91 Mg alloy	54
Table 5.1	Elemental distribution obtained using EDS, at different regions marked in Fig. 5.3.	70
Table 6.1	Fatigue test results of samples with different microstructural composition showing No. of cycles to failure at different stress amplitudes	87
Table 7.1	Strain rate sensitivity measured at peak load	100

LIST OF ABBREVIATIONS

GWP	Gross World Product
SPD	Severe Plastic Deformation
FSP	Friction Stir Processing
FSW	Friction Stir Welding
HCP	Hexagonal Closed Packed
ECAP	Equal Channel Angular Pressing
ARB	Accumulative Roll Bonding
RCS	Repetitive Corrugation and Straightening
HSDSR	High Speed rolling with Differential Speed Ratio
OM	Optical Microscope
SEM	Scanning Electron Microscope
EDS	Energy Dispersive Spectroscopy
XRD	X-Ray Diffraction
EBSD	Electron Back Scattered Diffraction
HCF	High Cycle Fatigue
GBS	Grain Boundary Sliding
DRX	Dynamic Recrystallization
DDRX	Discontinuous Dynamic Recrystallization
CDRX	Continuous Dynamic Recrystallization
GDRX	Geometric Dynamic Recrystallization
SFE	Stacking Fault Energy
HAGBs	High Angle Grain Boundaries
LAGBs	Low Angle Grain Boundaries
TMAZ	Thermo-Mechanically Affected Zone
CRSS	Critically Resolved Shear Stress
ASTM	American Society for Testing and Materials
SENB	Single Edge Notch Bend specimen
XFEM	eXtended Finite Element Method
EDM	Electric Discharge Machining
CNC	Computer Numerical Control

AC	As-Cast material
HFG	Half thickness Fine Grained material
SFG	Surface modified by Fine Grained material
FFG	Full thickness Fine Grained material

LIST OF SYMBOLS

Ppm	parts per million
CO_2	Carbon di Oxide
Mg	Magnesium
Al	Aluminium
PL_4	Tool with 4 mm pin length
PL_5	Tool with 5 mm pin length
PL_7	Tool with 7 mm pin length
T4	Solution treatment
T6	Solution treatment and artificial aging
J_{IC}	Critical J integral value (kJ/m^2) under mode I loading
K_{IC}	Plane strain fracture toughness or Critical stress intensity factor ($MPa\sqrt{m}$) under mode I loading
T_m	Melting point temperature (°C)
M	Strain rate sensitivity
σ_y	Yield strength (MPa)
σ_0	Lattice frictional stress (MPa)
K	Strengthening Co-efficient in Hall-Petch relation ($MPa\sqrt{m}$)
D	Grain size (μm)
σ_{UTS}	Ultimate tensile strength (MPa)
$\sigma_{UTS,f}$	Ultimate tensile strength of fine grained region (MPa)
$\sigma_{UTS,m}$	Ultimate tensile strength of as-cast region (MPa)
$\sigma_{UTS,c}$	Ultimate tensile strength of mixed fine and as-cast region (MPa)
e_f	Elongation of fine grained region (%)
e_m	Elongation of as-cast region (%)
e_c	Elongation of mixed fine and as-cast region (%)
σ_s	Solid solution strength (MPa)
σ_g	Grain boundary strength (MPa)
σ_d	Orowan mechanism strength (MPa)

$\dot{\varepsilon}$	Strain rate (s^{-1})
X	Atomic weight fraction of solute
G	Shear modulus (MPa)
B	Burger's vector
N	Poisson's ratio
F	Volume fraction
K_Q	Apparent fracture toughness
A	Dimensionless constant
D	Diffusion Co-efficient
Q	Activation energy (kJ/mol)
T	Absolute temperature (K)
N	Stress exponent
P	Grain size exponent
K	Boltzmann constant = 1.38×10^{-23} J/K
R	Gas constant = 8.314 J mol^{-1} K^{-1}

CHAPTER 1

INTRODUCTION

OVERVIEW

This chapter begins with the necessity of Mg for the industrially developing world. The motivation of this research work is explained based on the innovative idea of using mixed coarse and fine grained microstructure to achieve improvement in the mechanical properties of the as-cast material. Further, chapters in the thesis are detailed.

CHAPTER 1

INTRODUCTION

Amidst materials like titanium, lithium and scandium which have significant impact on the quality of our life, magnesium gains attention as its global supply and demand are growing in a faster rate than the global gross domestic product which is approximately 3.3 % from 2002 to 2014. Its production had grown at a compound annual growth rate which was slightly under 6 % meanwhile its demand was closer to 7% [1].

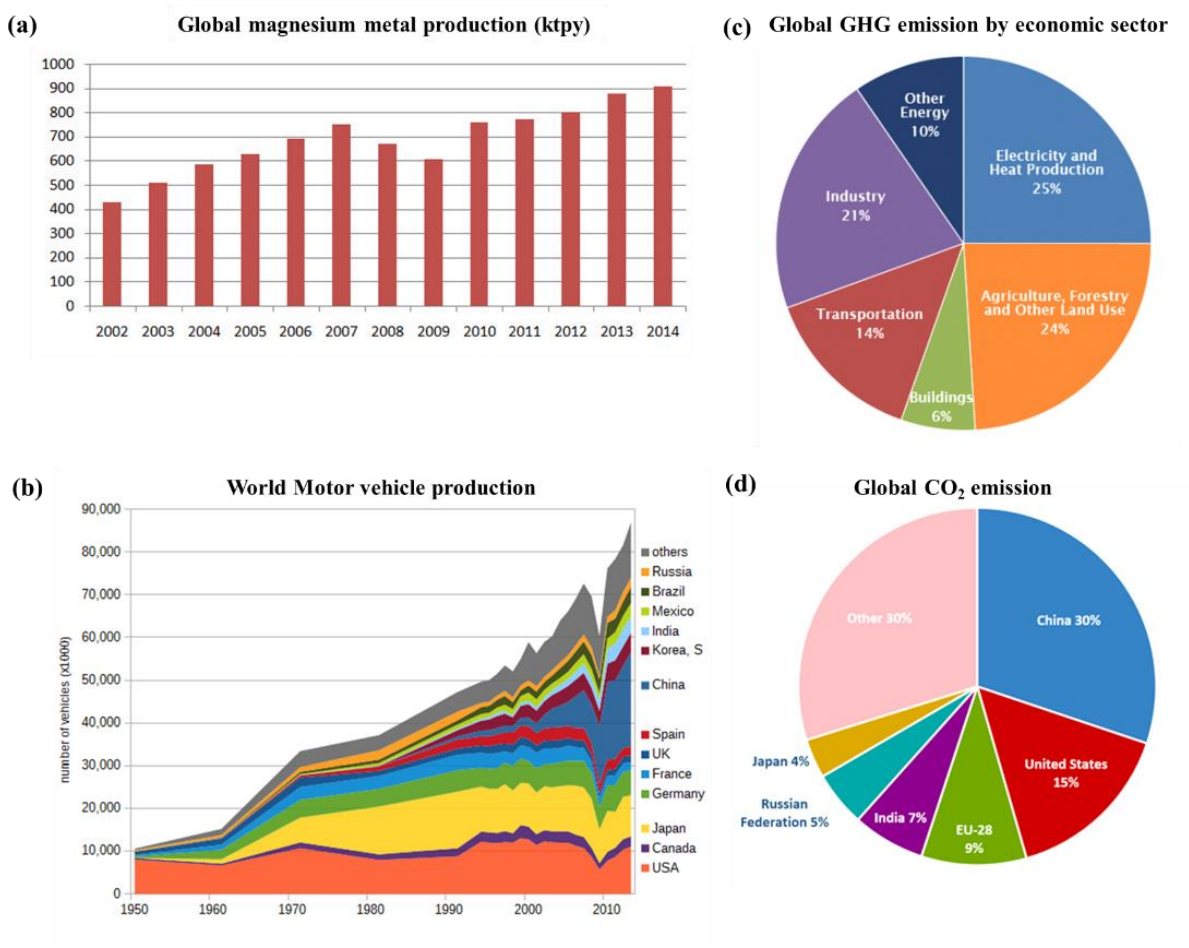

Fig. 1.1: (a) Magnesium production from 2002 to 2014 [1]**, (b) World motor vehicle production from 1950 to 2013** [2]**, (c) Global greenhouse gas emissions by sectors and** [3] **(d) Global CO_2 emission by countries** [3]**.**

The demand for Mg (Fig.1.1(a)) is due to increase in the rate of annual production of vehicles all over the world [2] (Fig.1.1(b)). Boeing has predicted the need of over 39600 airplanes over next 20 years [4]. Mg is the lightest metal capable of serving as both structural and non-structural applications therefore it is expected to replace most of the steel and aluminum in automobile and aviation sectors to incur fuel economy and to reduce CO_2 emission [5]. Since the beginning of industrial revolution(1750), anthropogenic CO_2 emissions increases from 280 ppm to 406 ppm in the early 2017 [6]. Transportation and manufacturing industries are the most emitter of CO_2 next to power and agricultural sectors (Fig.1.1(c)) and 61 % CO_2 emission was created by China, US, European Union and India (Fig. 1.1(d)) [3] . Hence, the growth rate of Mg production well in excess of GWP is a strength for economy as well as environment.

The first application of Mg in automobile was the engine piston developed by Dow Chemicals in USA for Indy 500 racing cars in 1921 [7]. Later, sand cast crank cases were commercially developed in England and Germany in 1930s. Automotive magnesium consumption reached it peaks when Volkswagen Beetle was introduced with major application of Mg in air cooled engine and gear box castings which together weighs only 20 kg. However, greater power requirement for the engines increases its operating temperature and load. It necessitates the modification of air cooled engine to water cooled engine which eliminate Mg as structural powertrain material in automobiles after 1970s. Similarly in aerospace applications Mg was main structural metal used for German military aircrafts during World War I and extensively used during World War II in US Air forces' long range bombers B-36 and B-52 [8]. Boeing used 1200 Mg parts in the airplanes built during 1962-1984 [5] but in modern aviation many of these applications were reduced due to its apparent fire hazard and limited only to non-structural parts in aerospace applications [9]. However, in recent years, with safe design practices Mg alloys found numerous application in automobiles. In aerospace applications, following the Federal Aviation Administration (FAA) conditional approval of using magnesium based materials in aircraft cabin in seat construction replacing Al based alloys reduces 30 % of total weight. This translates into 360 kg weight saving for a typical 117-seat narrow body Airbus A318 and up to 4200 kg for a 700 seat Airbus A380 wide body plane [10].

Commercially, Mg alloys can be divided into two categories; wrought alloys and cast alloys. Mg have relatively low melting point and it is easy to melt and cast. Therefore, 98 % of Mg in structural applications are cast products but the large dendrites, brittle interdendrites and casting defects like porosity reduces its strength. Its hcp crystal structure offers only two independent slip systems at room temperature leads to poor ductility. According to both Taylor's theory [11] and von Mises criteria on distortion [12,13], any material should possess five independent slip systems to deform plastically. The tensile properties of wrought Mg alloys are better than the cast alloys but have a higher asymmetry of yield [14]. Though Mg and its alloys are widely used in automobile industries, certainly, its usage by the leading aircraft manufacturers (Airbus, Boeing, and Lockheed Martin) is very limited [15,16]. The comparison of tensile properties of materials used in aerospace materials is shown in the Fig.1.2. As the desire to use magnesium for high performance application in automobiles and airplanes has been growing [7,17–24], it possess serious challenges to researchers in improving the mechanical properties of Mg alloys to compete with aluminum and steel. There are many research articles focused on improving the mechanical properties of Mg alloys by processing to obtain suitable microstructural modification which imparts one or more of the strengthening mechanisms, namely, solid solution strengthening, precipitation hardening, dislocation interactions or Orowan strengthening and grain refinement [25–32].

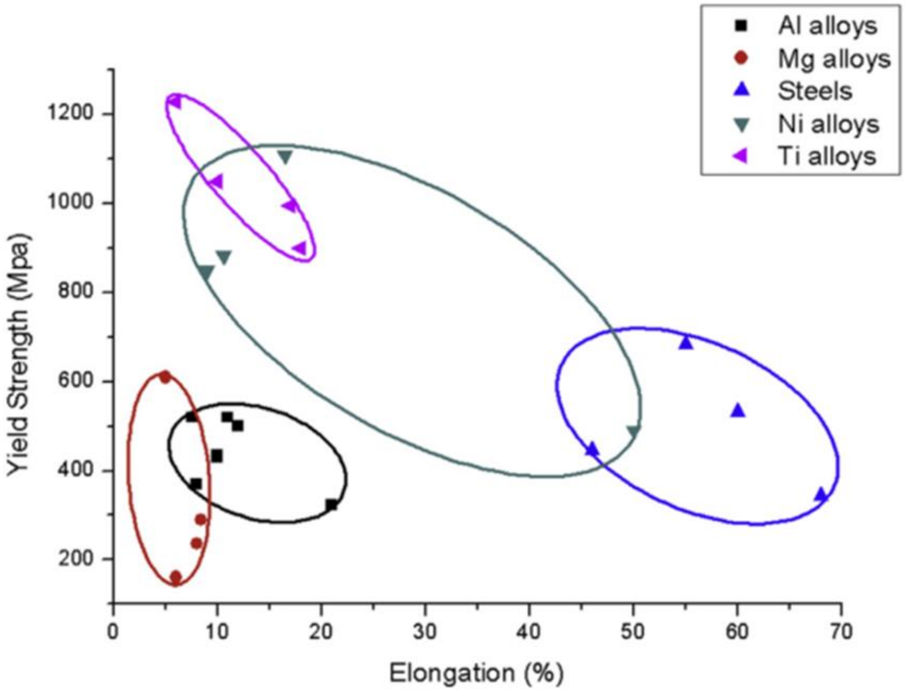

Fig. 1.2: Typical yield strength and elongation of some metal alloys [16].

Improving strength by grain refinement is one of the prominent research area in recent times. [33,34]. The Hall-Petch slope of Mg alloys is greater than Al alloys, therefore, grain refinement is more effective strengthening mechanism in Mg alloys when compared to Al alloys [35]. Grain refinement in Mg alloys can be achieved by various means. For example, conventional metal working methods like; rolling, forging and extrusion [31,36–38], severe plastic deformation (SPD) methods like; equal channel angular extrusion (ECAE), accumulative roll bonding (ARB), high pressure torsion (HPT), friction stir processing (FSP) [39–44] etc. Intense plastic deformation reported to modify the microstructure as well as impart crystallographic texture to the material [45].

FSP is a solid state processing technique for changing material properties by severely localized deformation. This deformation is caused by stirring motion when a non-consumable rotating tool is inserted in to the work piece and pushed laterally. It can also be used as bulk processing technique by performing multiple passes with 50% overlap between two consecutive passes. FSP can be used a) to reduce porosity, b) to achieve uniform distribution of second phase particles in the matrix and, c) grain refinement, d) to prepare surface composites and solid solutions [46,47], in order to improve the mechanical properties. FSP can be used for microstructural modification of surface or full thickness. The pertinent question therefore is whether one need to process full thickness or only the surface to improve the properties. According to the Griffith criterion, the surface defects are most critical and hence microstructural modification at the surface appears to be an economical alternative. In order to understand the behavior of microstructural modification on the mechanical properties in Mg alloy, hard to work, cast AZ91 Mg alloy was selected. As FSP has a distinct feature of modifying the microstructure locally, it was used to fabricate layered microstructure. The layered microstructure contain layers of as-cast coarse grains as well as FSPed fine grains through the thickness. The thickness of the fine grained region was controlled using the FSP tool pin length.

A brief description about the sequence of work performed are; initially, the properties of as-cast microstructure were studied after solution treatment and ageing conditions. Subsequently multipass FSP was performed using different tool pin lengths then layered microstructures was generated which contains the layers of as-cast and FSPed microstructure. Then its influence on mechanical properties were analyzed. Finally, a constitutive equation was developed for the superplasticity of FSPed Mg alloys.

In **Chapter 2**, the literature review is provided with detailed understanding about Mg and its alloys, methods to improve their properties, FSP in general and FSP of Mg alloys, factor affecting FSP and its influence on microstructure, texture and mechanical properties, namely;

tensile, fracture, fatigue and superplasticity. Moreover, the influence on mechanical properties due to the microstructural variation in terms of grain size are also discussed. The objective of the work is defined based on the important findings and gaps found from the reviewed literatures.

In **Chapter 3**, the experimental work is explained in detail according to the sequence of works performed. First, about the solution treatment and heat treatment of as-cast alloy; second, FSP using different tools, and third, experimental details of all mechanical tests (tensile, fracture, fatigue and superplasticity). Finally, materials characterization methods (OM, SEM, XRD, EDS and EBSD) were described and performed wherever required.

In **Chapter 4**, the microstructure and the mechanical properties of AZ91 alloy in as-cast, solution treated and aged conditions were studied. Dissolution of second phase particles was observed, during solution treatment (T4), in the optical micrograph of samples removed from furnace at different time intervals and re-precipitation of particles observed in samples after ageing treatment (T6). The tensile and the fracture toughness test of the three conditions were performed and analyzed. The fracture toughness values were evaluated using J-integral method.

In **Chapter 5**, the effect of tool pin length on the microstructure and tensile properties of FSPed AZ91 Mg alloy were studied. Three tools: PL_4 with 4 mm pin length, PL_5 with 5 mm pin length and PL_7 with 7 mm pin length, were used. The results confirmed that the variations in the properties with increasing thickness of the processed region was insignificant. It ensures that the properties of layered microstructure (in subsequent chapters) can be analyzed considering similarities in the processed region using three tools with different pin length.

In **Chapter 6**, multipass friction stir processing (FSP) was performed on as-cast (AC) AZ91 magnesium alloy with different tool pin lengths to introduce layered microstructure through the thickness, namely, HFG, SFG and FFG. Tensile tests, fracture toughness test on samples without fatigue pre-crack and high cycle fatigue (HCF) tests were conducted. Strengthening mechanisms and fracture morphologies of the tested samples were analyzed to understand the effect of layered microstructure on the mechanical properties.

In **Chapter 7**, the effect of layered microstructures (HFG, SFG and SFG) on the superplastic behavior were studied. High temperature tensile tests were carried out at 350°C using three different initial strain rates i.e. $5\times10^{-3}\ s^{-1}$,$1\times10^{-3}\ s^{-1}$ and $5\times10^{-4}\ s^{-1}$. Texture studies were performed on samples before and after the test to understand the behavior of layered microstructure during superplastic deformation and the mechanisms responsible for deformation in as-cast region as well as in FSPed region are also studied.

In **Chapter 8**, the constitutive equation for superplasticity was developed using tensile data of the high temperature deformation of FFG material. Tensile tests were carried out at 150°C, 250°C and 350°C and at three different strain rates of 5×10^{-3} s^{-1}, 1×10^{-3} s^{-1} and 5×10^{-4} s^{-1} at each temperature. The constitutive equation was derived after evaluating the material parameters from the data obtained from tested samples.

In **Chapter 9**, brief summary of the conclusions for the mechanical behavior of FSPed AZ91 magnesium alloys and scope for future work is presented.

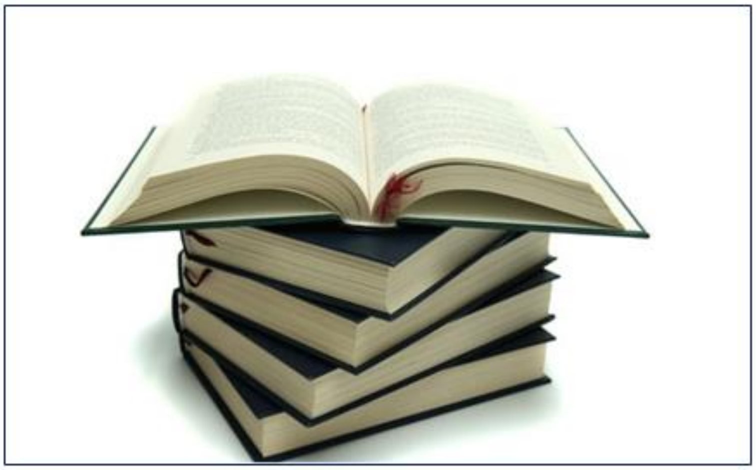

CHAPTER 2

LITERATURE REVIEW

OVERVIEW

In this chapter, the literatures that guided during the research to establish the processes and test methods and the literatures that helped to understand the important mechanisms, concepts and interesting phenomenon are reviewed.

CHAPTER 2

LITERATURE REVIEW

Friction stir processing (FSP) is a solid-state processing which is suitable for processing of hard to deform materials. FSP offers great potential to process HCP materials such as Mg alloys. Mg alloys exhibit poor ductility and hence pose a challenge to process it after casting. Since Mg is an important structural material because of its low density and high specific strength, processing of these alloy is an important problem to be solved. For example, aerospace and automobile industries see Mg as a potential replacement for steel and aluminum. Therefore, the literature review is started with an introduction to Mg and its alloys and focused on AZ91 Mg alloy in detail. Further, literature on FSP was reviewed covering factors influencing FSP and effect of FSP on the microstructure and mechanical properties. Finally, summary of literature review and identified gaps from reviewed literatures were used to formulate objectives for the research work.

2.1 Magnesium and its alloys

Magnesium (atomic no. 12 and atomic wt. 24.32) occupies a place in Group II of the Periodic table. It is the lightest of all commonly used structural materials with a density of 1.7g/cm^3, approximately one third that of aluminum. It is the third most abundant metallic element in the earth's crust. Magnesium must be alloyed with other metals for engineering applications. The alloying elements of Mg and their effects are presented in the Table 2.1. The popular commercial magnesium alloys include AZ series (Mg-Al-Zn), AM series (Mg-Al-Mn), AE (Mg-Al-RE), EZ (Mg-RE-Zn), ZK (Mg-Al-Zr) and WE (Mg-RE-Zr), where RE stands for rare earth elements. The aluminum and zinc based Mg alloys (AZ series) offer good strength, corrosion resistance and castability. These alloys are produced using sand casting or die casting. The aluminum and manganese based Mg alloys (AM series) possess good ductility and used in forged and extruded conditions. The rare-earth based alloys have good creep resistance and used for high temperature applications. Moreover, the addition of different elements like Ca, Ce, Y, Nd, Be, Li, Bi, Sb, Ag, Ti, Gd and Zr with existing AZ, AM and rare earth based Mg alloys to achieve specific properties were reported by Friedrich and Mordike [48].

Table. 2.1: Alloying elements of Mg and its effect [49].

Alloying Element	Effects of Addition
Aluminum	• most widely used in alloying due to numerous favorable effects • increases hardness, strength and castability while only increasing density minimally • average alloy contains about 2-9 weight percent of aluminum and can be heat treated with > 6 weight percent • increased amount of aluminum decreases the ductility of the alloy
Beryllium	• included only in very small quantities • significantly reduces surface melt oxidation during processing • grain coarsening can occur • can be a carcinogenic material and is being rejected for use
Calcium	• improves thermal and mechanical properties as well as assists in grain refinement and creep resistance • reduces oxidation during processing when added to cast alloys • allows for better rollability of sheet metal • additions exceeding 0.3 weight percent, increases the risk of weld cracking • reduces surface tension
Cerium	• improves corrosion resistance • increases plastic deformation capability, magnesium elongation, and work hardening rates • reduces yield strength
Copper	• assists in increasing both room and high temperature strength • negatively impacts ductility and corrosion resistance
Manganese	• increases saltwater corrosion resistance within some aluminum containing alloys • reduces the adverse effects of iron, usually present in 0.2-0.4 weight percent
Nickel	• increases both yield and ultimate strength at room temperature • negatively impacts ductility and corrosion resistance
Neodymium	• improves material strength
Rare Earth Metals	• increase in high temperature creep and corrosion resistance and strength • allows lower casting porosity and weld cracking in processing
Silicon	• can increase molten alloys' fluidity • improves elevated temperature properties, especially creep resistance • only used in pressure die casting
Strontium	• used in conjunction with other elements to enhance creep performance
Tin	• when used with aluminum it improves ductility, and reduces tendency to crack during processing
Yttrium	• enhances high temperature strength and creep performance when combined with other rare earth metals
Zinc	• second most commonly used alloying metal with magnesium • increases the alloys' fluidity in casting • when added to magnesium alloys with nickel and iron impurities, it can improve corrosion resistance • additions of 2 weight percent or greater tend to be prone to hot cracking
Zirconium	• refines grain size in sand and gravity castings (not combined with aluminum)

Mg alloy containing RE elements like thorium (HZ22) could be used at highest working temperature of 350^{o}C but are not generally used since thorium is radioactive [23]. Other rare earth elements like Nd are very expensive and rarely used due to its limited availability. This suggests that for high volume applications like automobile and aerospace, research and development of non-RE based alloys is crucial. Besides, 90 % of Mg alloys used in automobiles are cast alloys and one of the most commonly used cast alloys is AZ91 Mg alloy which is difficult to form by conventional metal working methods.

2.2 AZ91 Mg alloy

2.2.1 Chemical composition

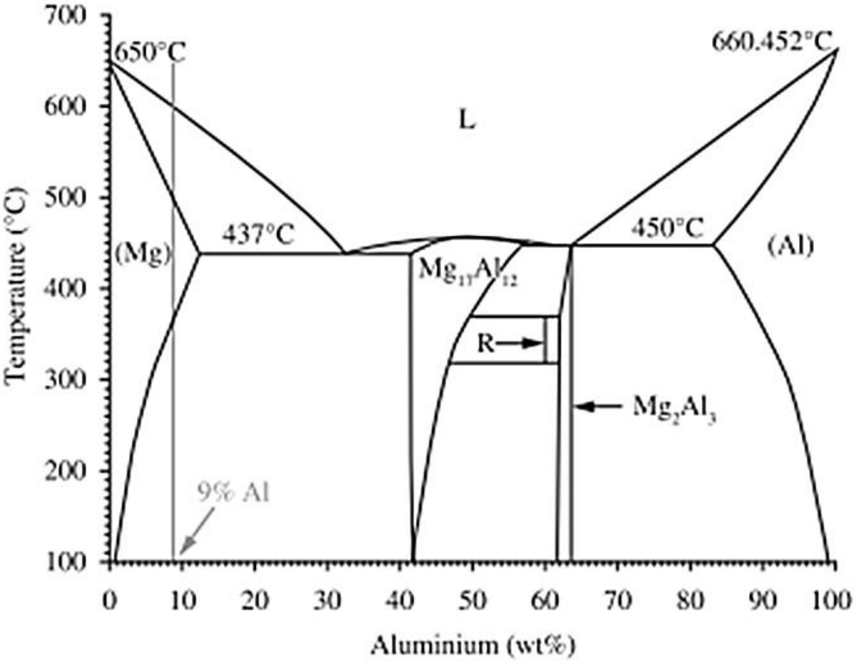

Fig. 2.1: Mg-Al binary phase diagram [50]**.**

The AZ91 Mg alloy contains 9 wt. % Al and 1 wt. % Zn. The aluminium is alloyed with Mg to improve strength, corrosion resistance and castability. The Mg-Al binary phase diagram is shown in Fig.2.1. It shows that for 9 wt. % Al alloy α-Mg starts to solidify at around 600°C and grows dendritically during solidification up to the eutectic temperature of 437°C. Although the composition lie in the single phase region but due to non-equilibrium solidification some amount of liquid undergoes eutectic reaction [51]. The eutectic mixture consist of α-Mg and β-

$Mg_{17}Al_{12}$, an intermetallic compound. In case of AZ91 alloys, zinc takes the position of Al in the β-phase as β-$Mg_{17}Al_{11.5}Zn_{0.5}$, however it is generally considered as β-$Mg_{17}Al_{12}$ phase [49]. Thus, the cast microstructure of AZ91 alloy mainly consists of α-Mg dendrites surrounded by the network of eutectic mixture. At eutectic temperature, maximum solid solubility of Al in Mg is 12.7 wt. % but the maximum solubility reduces to 3.2 wt.% at 200°C.

2.2.2 Mechanical properties

Increasing Al content in Mg alloys increases the volume fraction of β-phase which leads to increase in strength but at the cost of ductility [52]. Other than chemical composition, the method of casting and heat treatment methods decides the cast material properties. The heat treatment methods to improve the strength of AZ91 Mg alloys are solutionization (T4) and artificial aging after solutionization (T6). The mechanical properties of AZ91 alloy obtained by various casting methods [7] and heat treatment methods [53] were reported in different articles. It shows that the strength at room temperature is below 250 MPa with poor ductility.

Engineering materials designed specifically for structural applications are limited by their fracture toughness rather than by their strength. Fracture toughness is the property of a material which defines its ability to resist crack or fracture. In addition to chemical composition and microstructure this property is sensitive to defects such as porosities and inclusions. These pre-existing features can assist crack initiation and accelerates crack propagation. Although 90 % of the cast Mg alloys used in structural applications are made of AZ91 alloys, its toughness properties does not match for some of the applications in automobiles like, seat components, instrument panel and steering wheel cores [54]. Fracture toughness values of material can be evaluated by calculating the critical stress intensity factor (K_{IC} in MPa√m) or by calculating the critical energy required by the crack to grow (J_{IC} in kJ/m^2). For AZ91 Mg alloys K_{IC} values were in the range of 7.6 to 14.5 MPa√m and J_{IC} values were around 5 kJ/m^2 [55–59].

Fatigue is a failure mechanism of engineering materials, in which materials fail well below its yield strength under cyclic loading. The fatigue strength of magnesium alloys is linearly related to the tensile strength [60]. The inhomogeneities and discontinuities, like porosities, second phase particles and surface defects affect the number of cycles to failure. Absence of such adverse constituents may prolong the materials life but does not prevent fatigue failure completely. The reversible slips and twinning and de-twinning in some cases [61,62], accumulates large strain that leads to fatigue failure. As porosity and other defects are common in cast materials, there would be large scatter in its fatigue data. Among the AZ series Mg alloys AZ91 alloys shows least fatigue life [63]**.**

At high temperatures, polycrystalline materials undergo high tensile elongation of at least 200 %. Although most of the automobile components are made by castings, sheet metal forming is also an important route to manufacture parts that are complex in shape. Superplastic forming can produce components with smooth curves and contours from a sheet metal in single operation. Superplasticity is exhibited by certain polycrystalline materials at the deformation temperature of above $0.5T_m$, where T_m is the absolute melting point of the material and, strain rate ranging from 10^{-5} to 10^{-3} s^{-1}. The material should have stable, equi-axed and fine grain microstructure. Materials deformed at low temperatures resist necking by work hardening while superplastic materials resist necking due to the sensitivity of flow stress to strain rate, called strain rate sensitivity (m) [64]. Among Mg alloys ZK60 showed a best ever ductility of 3050% with an initial grain size of 0.8 μm [65]. Maximum elongations obtained by different Mg alloys vary depending on the material and initial microstructure [66–70].

2.2.3. Strengthening mechanisms

2.2.3.1 Grain size strengthening

The decrease in grain size increases the volume fraction of grain boundary. The grain boundaries are highly disordered which prevents continuous slip of dislocations. It also pins the dislocation motion and resists its further propagation. As adjacent grains have different orientation the dislocations requires more energy to change direction and propagate in to the next grain. The piled-up dislocations will delay the onset of plastic deformation and increases the yield strength of the material [71]. The grain size contribution to the yield strength (σ_y) is evaluated using the familiar Hall–Petch relation given by eqn. 2.1.

$$\sigma_y = \sigma_0 + Kd^{-1/2} \qquad 2.1$$

Where, σ_0 is intrinsic lattice resistance to basal slip, d is the grain size of the material and k is the Hall-Petch slope, which depends on material and nature of the processing route. This model was first proposed by E.O. Hall, who related the crack length or length of slip bands with grain size [72] and N.J. Petch, who related the cleavage strength with ferritic grain size at extremely low temperatures [73]. Since then, six decades of use of Hall-Petch relation on large number of materials were reviewed by Armstrong [74]. The relationship holds well not only for hardness and yield strength but also for fatigue, fracture mechanics, shear banding and strain rate sensitivity. Ductility in Mg alloys also reported to improve after grain refinement [75,76].

2.2.3.2 Solid solution strengthening

The strength of the pure metals can be improved by solid solution strengthening [77]. After alloying with solute atoms, the elastic strain around the lattice resists the dislocation motion and hinders plastic deformation. The solid solution strengthening effect of Al in Mg was investigated by Caceres and Rovera [29]. Their observations are compatible with the single crystal data of Aktar and Teghtsoonian [78] and hence, the solid solution strengthening (σ_s) contribution is evaluated according to Eq. 2.2.

$$\sigma_s = CX^{2/3} \qquad 2.2$$

where C= 197 (MPa $X^{-2/3}$) and X is the atomic fraction of solute.

2.2.3.3 Orowan strengthening

The interaction of precipitates with dislocations leads to Orowan strengthening. The size, shape and number fraction of the precipitates influences the dislocation interaction and considerably affect the mechanical properties of the material [79–82]. The Orowan strengthening (σ_d) due to plate shaped precipitates and spherical shaped precipitates are given by Eq.2.3 and Eq. 2.4 respectively by Nie [83].

$$\sigma_d = \frac{Gb}{2\pi\sqrt{1-v}\left(\frac{0.953}{\sqrt{f}}-1\right)d} \ln\frac{d}{b} \qquad 2.3$$

$$\sigma_d = \frac{Gb}{2\pi\sqrt{1-v}\left(\frac{0.779}{\sqrt{f}}-0.785\right)d} \ln\frac{0.785d}{b} \qquad 2.4$$

where G is the shear modulus (17 GPa for magnesium), **b** is the Burgers vector (3.2 x 10^{-10} m), v is the Poisson’s ratio (0.35), f is the phase fraction of β-phase and d is the mean planar diameter of the precipitates. Other than grain boundary strengthening, solid solution strengthening and precipitate hardening, dispersion hardening [84–86] also reported to contribute to the strengthening of AZ91 alloy. Further, work hardening was influenced by both solid solution and precipitate hardening [87].

2.2.4. Deformation mechanisms

Magnesium contains hexagonal close packed crystal structure. Its lattice parameters are c = 0.519 nm and a = 0.318 nm, hence it has c/a ratio of 1.624 close to the ideal c/a ratio of hexagonal materials. Initial deformation in Mg starts with basal slip, further deformation depends on other parameters such as, c/a ratio, temperature and loading condition [26]. Slip on basal plane offers only two independent slip system. According to von Mises criterion, the material must possess five independent slip system in order to deform plastically without failure. However, high shear stress is required to activate slip on prismatic and pyramidal planes which results in brittle behavior [88]. The slip planes, namely, basal, prismatic and pyramidal in Mg are shown in the Fig. 2.2(a), (b) & (c) respectively.

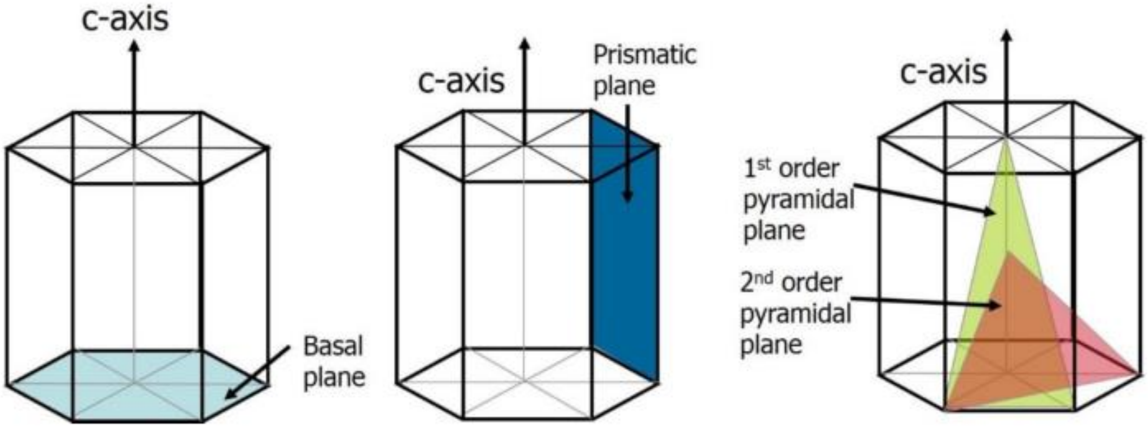

Fig. 2.2: Slip systems in Mg (a) basal slip, (b) prismatic slip and (c) pyramidal slips [3].

Table 2.2: Slip systems in Mg [33]

Direction	Plane	Slip System	Number of independent slips
$\langle a \rangle$	Basal	$\{0002\}\langle 11\bar{2}0 \rangle$	2
$\langle a \rangle$	Prismatic	$\{1\bar{1}00\}\langle 11\bar{2}0 \rangle$	2
$\langle a \rangle$	Pyramidal 1st order	$\{1\bar{1}01\}\langle 11\bar{2}0 \rangle$	4
$\langle a \rangle + \langle c \rangle$	Pyramidal 2nd order	$\{10\bar{1}1\}\langle 11\bar{2}\bar{3} \rangle$	4
$\langle a \rangle + \langle c \rangle$	Pyramidal 2nd order	$\{2\bar{1}\bar{1}1\}\langle 11\bar{2}\bar{3} \rangle$	4
$\langle a \rangle + \langle c \rangle$	Pyramidal 2nd order	$\{11\bar{2}2\}\langle 11\bar{2}\bar{3} \rangle$	4

Table 2.2 shows different slip systems in Mg and number of independent slip sytems they offer. Only basal, in case of c/a ratio approximately equal to the ideal value of 1.633, or prismatic slip, in case of c/a ratio lesser than the ideal value, will be activated at room temperature in hexagonal closed packed material. The critical resolved shear stresses for non-basal slips (prismatic and pyramidal slips) will be reduced at temperatures above 200°C. The pyramidal slips contains large burgers vector (c + a) and small interplanar distance which makes it difficult to activate at room temperature. Increasing the temperature will ease the activation process of pyramidal slip system. These additional slip planes improve ductility at higher temperatures.

Other than slip, twinning plays an important role in the deformation of Mg and its alloy. Twinning may reorient the crystal lattice which can activate other slip systems and enhance the ductility [89–91]. There are two types of twins generally observed in hexagonally closed pack materials; tension twins and compression twins. Twinning causes shear in one direction only, hence, tension twin and compression twin represents the sense of the strain developed on the c-axis of the crystal while twinning. The most common tensile twin in Mg occur in the twin plane $\{10\bar{1}2\}$ and shears in the $\langle 10\bar{1}\bar{1}\rangle$ direction (Fig. 2.3(a)) while compression twin occur in $\{10\bar{1}1\}$ plane and shears in the $\langle 10\bar{1}\bar{2}\rangle$ direction (Fig. 2.3(b)). Double twinning also found in Mg during compression at -196°C [92,93].

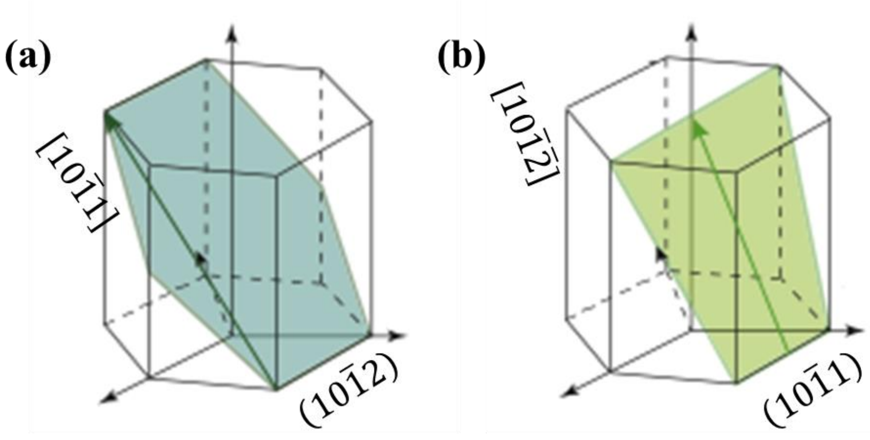

Fig. 2.3: (a) tensile twin and (b) compression twin [94]**.**

Interactions of dislocations with solutes is an important strengthening or/and deformation mechanism in Mg alloys. Tsuru and Chrzan [95] studied the solute dislocation interaction in Mg using different solute atoms. Addition of Al and Zn were reported to have less influence on the dislocation interaction when compared other solute atoms like, Y, Ca, Ti and Zr. The interaction of β-$Mg_{17}Al_{12}$ particles with basal and prismatic slips were studied by Liao et al. [96,97]. Both basal and prismatic slips have ability to shear through the matrix and precipitate/matrix interface instead of looping around the obstacle. They considered this interaction as an extreme case of Orowan mechanism where the strength of the precipitate/matrix interface is weak.

Three important deformation mechanisms at high temperature deformation are diffusion creep, grain boundary sliding (GBS) and slip by dislocation movement. The mechanisms are common to both creep and superplasticity. Diffusion creep is the vacancy movement from the parallel-to-applied stress grain boundaries which experiences tension to the transverse grain boundaries, which experiences compression (perpendicular to applied stress), . If the vacancy transfers takes place through the crystal lattice then the diffusion creep is called Nabarro-Herring creep. If the vacancy transfer occurs through grain boundaries then the diffusion creep is called Coble creep. As the vacancies occupy the transverse grain boundaries and get absorbed, a counter flux of atoms occurs towards the parallel-to-applied stress grain boundaries and cause grain elongation. Diffusion creep can be accommodated by another deformation mechanism GBS [98] and contains elongated grains [64]. The GBS that accommodating diffusion creep is called Lifshitz GBS. The other type of GBS called Rachinger GBS or simply GBS is a mechanism where adjacent grains displaced at the grain boundaries between them but the grains remain equi-axed. GBS is impeded by obstacles like triple junctions or other type of stress concentration. Hence, GBS also required accommodation process. The accommodation process for GBS are delivered by slip activities like dislocation slip, grain rotation, grain boundary migration and grain re-arrangement [99,100].

Dynamic recrystallization (DRX) is one another important deformation mechanism in many metals and alloys including Mg which produce fine grain microstructure. As fine grain microstructure is essential to improve material's mechanical properties as well as it helps in improving the superplastic elongation of the material. The important factors that influence DRX are initial grain size, second phase particles, stacking fault energy (SFE), and thermomechanical processing and severe plastic deformation conditions [101]. There are three types of DRX, namely, discontinuous DRX (DDRX), continuous DRX (DDRX) and geometric DRX (GDRX). Nucleation of new grains and grain growth at the expense of regions full of dislocations is called

DDRX [102] which is mostly observed during hot deformation of materials with low to medium SFE. In materials with high SFE, the sub grains or cell structure with low angle grain boundaries (LAGBs) formed during deformation are gradually evolved in to high angle grain boundaries (HAGBs) due to efficient dynamic recovery, which is known as CDRX [103]. In material like aluminium, the grains elongate with local serrations at high temperatures and large strain. On further increase in strain, these serrations pinch off and form high angle grain boundaries which is called GDRX [104].

Grain refinement through DRX can be achieved by different thermomechanical processing methods or severe plastic deformation methods. There are different SPD processes like equal channel angular pressing (ECAP), high pressure torsion (HPT), accumulative roll bonding (ARB), repetitive corrugation and straightening (RCS) obtained fine and ultrafine grains [105,106]. In ECAP, a rod shaped samples passed through the die with channels of equal cross section. Severe plastic strain was induced in the material and on repetitive passes the shear strain accumulates cumulatively up to 100-1000 and forms bulk fine to ultra-fine grains. However, it has several disadvantages like special shape of sample, smaller size, expensive tools and high power requirements restricts its use. HPT also requires high-power and expensive tools to operate and its parameters are difficult to control while ARB is simple as it doesn’t require any special equipment but it is detrimental to the roll life and difficult to maintain. Similarly RCS and other SPD methods have some difficulties in achieving the continuous production in industry.

Table 2.3: Key benefits of FSW/FSP [107]**.**

Metallurgical benefits	Environmental Benefits	Energy benefits
1. Solid phase process. 2. Low distortion of workpiece. Good dimensional stability and repeatability. 3. No loss of alloying elements. Excellent metallurgical properties. 4. Fine microstructure. 5. Absence of cracking.	1. No shielding gas required. No surface cleaning required. Eliminate grinding wastes. Eliminate solvents required for degreasing. 2. Consumable materials saving, such as rugs, wire or any other gases.	1. Improved materials use allows reduction in weight. Energy required for processing is as simple as milling operation.

FSP is relatively a new solid state processing technique developed by Mishra et al [108] which is comparatively an easier method to obtain grain refinement. FSP is derived from FSW which was invented at The Welding Institute of UK in 1991 [109]. It has several benefits over the SPD methods which are presented in Table 2.3. Moreover, FSP has several advantages like surface modification, modify cast microstructure, produce surface composites and can be modify the microstructure either locally or in the bulk of the material by multipass FSP.

2.3 Friction stir processing (FSP)

FSP is a solid state thermo-mechanical processing method as it softens and modify the microstructure of metallic materials by the synergy of frictional heat and severe plastic deformation. The schematic of FSP is illustrated in the Fig. 2.4. A rotating tool harder than the work piece material with a pin is plunged into the plate till its shoulder comes in contact with the surface and then traversed along the length of the plate. During the process the soften material will flow from advancing side to retreating side around the pin. Advancing side is the side of the tool in which tool rotation and traverse are in same direction whereas retreating side is the side in which tool rotation and traverse are in opposite direction. This flow of material around the pin generates a stir zone which have a microstructure different from the base material. The direction parallel to process is called process direction (X), the direction parallel to width of the plate is transverse direction (Y) and the third mutually perpendicular direction is normal direction (Z).

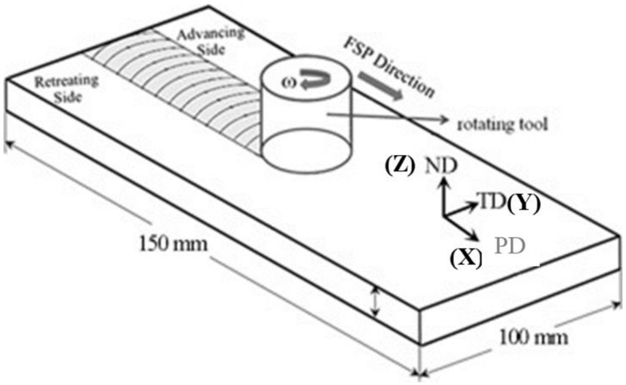

Fig. 2.4: Schematic of FSP.

FSW found its successful application in joining highly alloyed Al alloys such as 2XXX and 7XXX series. These alloys used in aerospace industries required a weld with high strength, and good fracture and fatigue resistance. Later, FSP found its application in improving the mechanical properties of cast aluminum alloys by modifying its microstructure. This commercial success of FSW/FSP of Al alloys motivated its application on other materials including steel, titanium, copper and magnesium. However, the feasibility of processing certain material depends on the nature of workpiece, proper selection of tool material, tool geometry and process parameters [110]. For example, FSP of steel and titanium alloys were highly dependent on the phase transformations due to temperature it attained during the process. In case of copper, which have 10-100 times higher thermal diffusivity than steel require low traverse speed to provide high heat input. Similarly, magnesium have large thermal expansion coefficient which cause large deformation during FSP. Hence, to obtain a good FSP in Mg alloys it was necessary to control the heat input during the process by some cooling methods. Mg and its alloys are also known for its poor room temperature formability. Therefore the feasibility study considering all the factors influencing FSP of Mg alloys were carried out and discussed further in this chapter.

2.4 Factors influencing FSP

2.4.1 Tool material

The tool material is important for FSP. The selection of tool material, shape and design depends on the workpiece material, desired tool life and operators experience and preferences. In general the tool used for FSP should possess following properties

- Good compressive yield strength
- Creep, thermal fatigue and fracture toughness to resist failure at high temperature and repeated thermal cycles
- Wear resistance to maintain dimension stability of the tool pin and shoulder and
- Good machinability, low cost and safe to process workpiece material.

. Nickel and cobalt based superalloy tools are used for FSP of harder materials like steel, titanium and copper but they are difficult to machine. Refractory materials like tungsten, molybdenum, and niobium are used as tool materials due to their high temperature strength but it is costly as it is produced through powder metallurgy route. Carbide materials, ceramic particle reinforced MMCs are also used as tool material but their brittle nature results in fracture during any mechanical action of the tool. Polycrystalline cubic boron nitride (PCBN) which is originally developed for machining of high speed steels, cast irons and superalloys also used for FSP due to their good mechanical and thermal properties but poor machinability, low fracture toughness and high cost limits its usage as a FSP tool. For soft materials like aluminum and magnesium the most widely used tool material is tool steel which is cheap and easy to machine.

2.4.2 Tool design

The material flow during FSP is highly dependent on the pin and shoulder geometry. The shoulder geometry is responsible for the frictional heat on the workpiece surface and acts as a confinement for heated material. It has outer surface, end surface and end surface features. The shape of shoulder outer surface has no influence on the process and so cylindrical outer surface is preferred generally. The end surface is used to entrap the heated material below it.

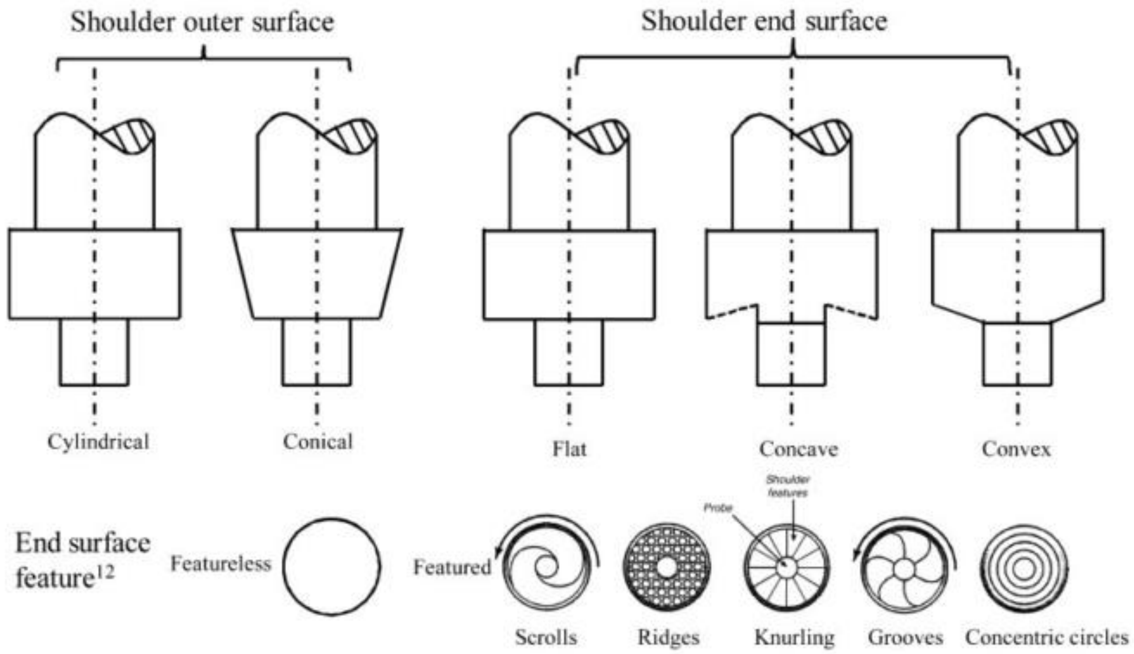

Fig. 2.5: FSP tool shoulder shapes and features [111]

There are three types of end surfaces; flat, concave and convex as mentioned in the Fig.2.5. The flat end surface is not efficient to entrap the flowing material which would flash the material out of the shoulder. To restrict materials extrusion concave shoulder end surface was designed. The concave end surface shoulder requires 1-3° to the normal direction of workpiece and against the processing direction for proper operation. Convex end surfaces are used for processing plates thickness lower than 1 mm, since the end surface shape become insignificant. The features of end surface plays a significant role in shearing the entrapped material under the end surface of shoulder at high traverse speeds. These features helps the material to flow from edge of the shoulder to the pin which eliminates the necessity of tilting the tool.

The pins are actual processing part of the tool. It deforms the material in front and moves the material behind it. Similar to shoulder, pins also have shapes and features. The shapes could be squared, cylindrical, tapered cylindrical and the features could be flat, threaded, threaded and fluted. The features may help in stirring the material effectively and considerably affect the final microstructure of the processed material. The effect of these features on FSP of Al and Mg alloys were reported by different authors [112–119]. It was found from the reviewed literatures that threaded pins with cylindrical or tapered cylindrical profiles were efficient in producing defect free welds or stir zones [120]. Moreover, threaded pins increases the vertical movement of material flow around the pin [121]. Even the pitch [122] and the orientation [123] of the threads were observed to influence the process.

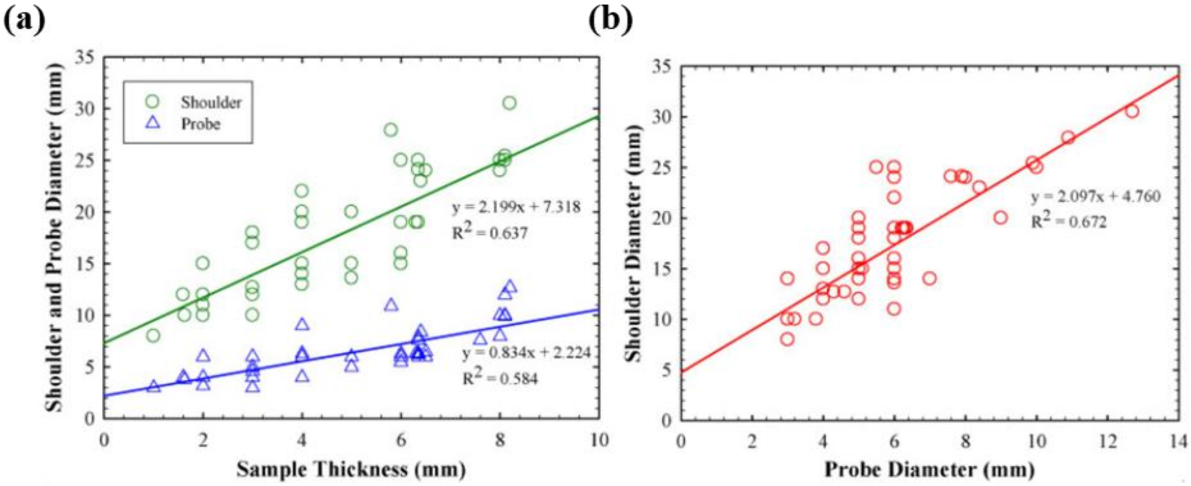

Fig. 2.6: (a) tool diameter versus workpiece thickness and (b) relation between tool diameters (pin and shoulder) [111]**.**

Mironov et al [116] studied the feasibility of FSW on ZK60 Mg alloy with samples of different thickness. They reported that thickness of the plate used for FSW have strong influence on the quality of the weld or process. The dimensions of shoulder and pin are empirically calculated as a function of sheet thickness. In Fig 2.6(a) the shoulder and pin diameters are plotted against sheet thickness. It implies that as the sheet thickness increases it requires more energy. Thus the larger shoulder diameter generate more heat and providing it as energy input. In Fig. 2.6(b) shoulder diameter was plotted against pin diameter. The shoulder diameter is 2.1

times the probe diameter plus 4.8 mm. However, the most commonly used ratio of shoulder-to-probe diameter is 3. The effect of the ratio of shoulder diameter (D) to pin diameter (d) on FSP of AZ31 plates was studied by [117]. The D/d ratio was varied from 2.25 to 5. The ratio greater than 3.5 exhibited defects like surface galling and flashes but the average D/d ratio equal to 3.3 produced good FSP without defects. Moreover, the shoulder diameter also plays significant role in plasticizing the material under the tool. The tool with larger area allow heat to concentrate during FSP and produced large plastic deformation. The microstructure generated by such large diameter tools were found to be stable even at high temperatures [115].

2.4.3 Process parameters

The process parameters that govern FSP are tool rotational speed, traverse speed, and tool tilt angle. The tool rotation speed and traverse speed controls the heat input, strain rate and grain size while tool tilt angle controls the flow of material under the shoulder and around the pin. Johnson [124], in his work, mentioned that FSW on Mg alloys can be successfully achieved at lower processing parameters when compared to aluminium alloys of same thickness. Cerri and Leo [125] reported the difficulty in FSP of AZ91 alloy due to formation of tunneling defects at higher rotational speeds of above 2000 rpm and at a traverse speed of 30 mm/min.

Chang et al [126] conducted FSP on AZ31 Mg alloy to study the effect of rotation speed on FSP. The traverse speed was kept constant at 90 mm/min and the rotational speed was varied from 180 to 1800 rpm. The grain size, strain rate and temperature were found to increase with the increasing tool rotation speed. The average grain size generally decreases with increasing strain rate and decreasing temperature. At 180 rpm, they obtained a finest grains of average size 2.2 μm under the temperature and strain rate conditions of 300ºC and 5.4 s^{-1} respectively. Lan et al [127] performed similar study on hot rolled AZ31 Mg alloy. At rotational speeds of 1300, 1500 and 1700 rpm and at a constant traverse speed the grain sizes obtained were 11.82 μm, 12.93 μm and 14.50 μm respectively.

Hutter et al [128] worked on the optimization of process parameters for FSP on pure Mg and AZ91 Mg alloy by varying both rotational speed and traverse speed. They carried out FSP using tool rotational speed in the range of 400 to 1500 rpm and traverse speed in the range of 30 to 52 mm/min. At a rotational speed of 1200 rpm pores were observed but at a rotational speed of 900 rpm or less and at traverse speed of 30 mm/min they obtained a pore free and homogeneous microstructure. The optimized process parameters were reported as 900 rpm and/or 400 rpm with 30 mm/min for AZ91 Mg alloy and 900 rpm with 30 mm/min for pure Mg.

In a work by Wang et al [129] AZ31B Mg alloy was friction stir processed using the traverse speed of 45 and 90 mm/min and rotational speed varied in the range of 800 to 1400 rpm. Though they didn’t reported any defects or imperfections in the processed plate in the range of process parameters used but found variation in the observed grain sizes. The grain size after FSP found to increase with increasing rotational speed and decreasing traverse speed. The minimum average grain size of 2.6 µm was obtained at 800rpm and 90 mm/min while maximum average grain size of 6.1 µm at 1400 rpm and 45 mm/min. Loke et al [130] also obtained good FSPed region using the different combination of process parameters; 490 rpm, 970 rpm, 63.5 mm/min and 190.5 mm/min. Generally the process parameter used for FSP of Mg alloys were below 1 m/min and 1500 rpm. However, Hutsch et al [131] performed single and multipass FSP on AZ31 Mg alloy using high traverse speed in the range of 1-10 m/min and high rotational speeds of 2000-3500 rpm. They termed it as high speed FSP and obtained defect free process zone with fine grains of 2 µm. Increasing the traverse speed results in decrease in size of the second phase particles and further influences the mechanical properties of the material [132]. The contribution of FSP process parameters on the hardness was analyzed using analysis of variance (ANOVA) method by Ramaiyan et al [133]. Traverse speed influences 52 %, tool profile 20 % and rotational speed accounted for 17 % of the property enhancement.

The effect of tool tilt angle during FSP of an aluminum alloy was studied by Long et al [134]. The zero tilt angle produces defect while the tilt angle of 2º increases compressive normal stress on the rear side of the tool, increase the local temperature, soften the material and aids in better material movement around the pin. Hence, no defects were observed in FSPed region at 2º tool tilt angle.

2.4.4 Pre-heating and cooling

Pre-heating and cooling was done to obtain control over the process and final microstructure. Rey at al [135] studied effect of pre-heating and cooling during the FSP of AZ61 and AZ91 Mg alloy. The coarse grain and cast microstructure of AZ91 requires pre heat to obtain a sound process zone. In case of rolled AZ61 Mg alloy, it was comparatively easy to process without any preheating. Heat extraction or cooling during the process was achieved by processing the plate over one of steel backing plate, copper backing plate or copper backing plate containing liquid nitrogen. The rapid cooling using copper backing obtained fine grained microstructure and liquid nitrogen cooling generated nano sized grains. Alavi Nia at al [136] used rapid cooling system during multipass FSP of AZ31 Mg alloy. The material was cooled rapidly after every pass to prevent the thermal effects on successive passes. It also helped in keeping the multipass process continuous without stopping intermittently for cooling. However, they didn't mention anything about the effect of tool heating on the continuous multipass FSP. The FSP performed by submerging the workpiece under water reported to exhibit extensive improvement in ductility [137]. Shen et al [138] used liquid nitrogen cooling for FSW of hot extruded AZ31 Mg alloy. The grain size of stir zone was decreased while the grain size of TMAZ increased. Moreover, using water for cooling during FSP caused oxide formation on the surface [139]. The oxide formation affects the final grain size of the FSPed microstructure. Hence, surfaces of the samples were sand blasted after every pass.

2.4.5 Multipass FSP

Multipass FSP can be performed by overlapping the first pass to the next pass. The overlapping ratio can be anywhere between 0 to 100 %. The overlapping ratio (OR) is measured using the equation, OR= 1- (*l*/d), where *l* is the distance between two passes and d is the diameter of the pin. Zero percent OR represents the distance between two passes equal to the pin diameter while 100 % OR represents second pass exactly on and above the first pass. Abbasi et al [140] performed multiple passes with 100 % overlap to achieve good mechanical properties. Rouhi et al [141] reported that 100 % overlapping passes in AZ91 alloy generated microstructure with much finer grains, more homogenized and more dissolution of β-$Mg_{17}Al_{12}$ phase when compared to the single pass FSPed materials.

In order to modify microstructure to certain width of the plate, multipass FSP need to be performed with the overlapping condition; 0 % < OR < 100 %. Sato et al [142] produced large scale plate of highly formable AZ91 Mg alloy using multipass FSP with 0 % overlap. Su et al [143] also produced large-area, bulk and ultra-fine grained aluminium alloy with relatively uniform microstructure using multipass FSP with 33 % overlap between passes. Govindaraju et al [144] studied the effect of *l* during the FSP of AE42 Mg alloy. They varied *l* from 0.5 to 2.5 mm. There were no effect in the extent of grain refinement but as *l* increases unprocessed regions were found between the processed zones. As tool dimensions were not mentioned in the work, the OR was not calculated. Venkateswaralu et al [145] used 0 %, 50 % and 100 % OR in FSP of AZ31B Mg alloy and compared with single pass FSP and base metal. The hundred percent overlapped material had shown better microstructural improvement in terms of grain refinement and homogenization but the work was not intended to process along the full width of the plate.

Moreover, the effect of direction of passes, that is, direction of first pass to next pass were studied by Tripathi et al [146] during multipass FSP of AZ31 Mg alloy. After first pass, the second pass was performed in the same direction, reverse direction and transverse direction. There were no apparent effect on grain refinement after the second pass but there was a morphological texture observed after the second pass performed in the same direction as well as the in reverse direction. Such morphological texture was not observed in the multipass FSPed material after transverse direction second pass.

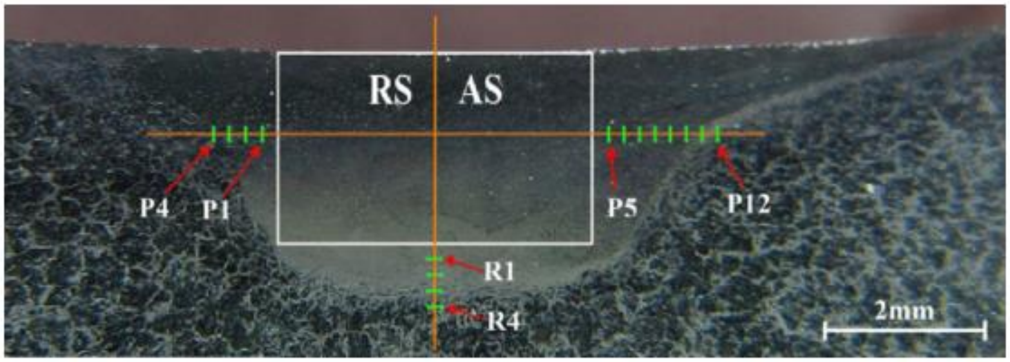

Fig. 2.7: FSPed region on AZ91 alloy showing stretched stir zone on advancing side and retreating side without any stretch zone [147]**.**

During multipass FSP, the tool can be moved, between passes, either towards advancing side or retreating side. Material flow simulations were studied during single pass FSP of Al and Mg alloys [148,149]. In one such simulation work by Asadi et al [147]**,** it was found that the stir zone was stretched towards advancing side and slight backward movement was observed in retreating side in AZ91 alloy as shown in Fig.2.7. The effect of overlapping direction during multipass FSP of AA 5083-H111 alloy with 50 % OR was studied by Gandra et al [150]. In Fig. 2.8(a) the overlapping was towards the retreating side which have wavy surface on the processed region throughout the width. In Fig. 2.8(b) the overlapping was towards the advancing side, which resulted in smooth surface after FSP. The wavy surface was obtained on overlapping towards retreating side probably due to the flashes curling over subsequent passes on advancing side, whereas these curls were destroyed while overlapping towards advancing side. There were no microstructural difference between the two overlapping methods but the mechanical property was best obtained on the material which multipassed by overlapping on retreating side. Johnson [124] found that good quality weld was obtained by placing the material on retreating side while FSW of dissimilar Mg alloys.

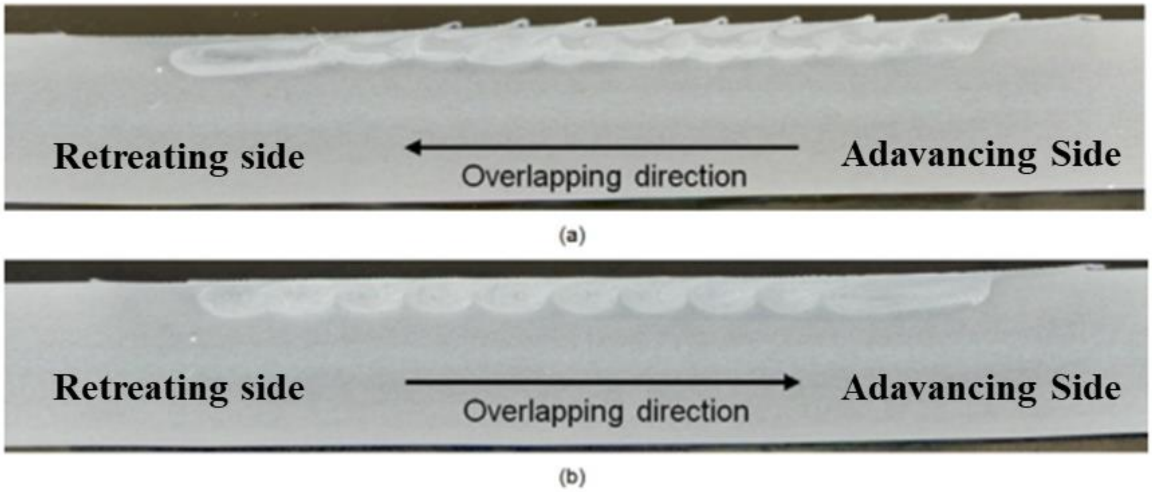

Fig. 2.8: Macrostructure of multipass FSPed plate showing overlapping towards (a) retreating side and (b) advancing side [150].

2.5 FSPed microstructure

During FSP, the region under the tool pin, called stirred zone, will be subjected to high temperature and severe plastic deformation which results in recrystallized grains and development of texture. As the temperature due to frictional heat increases to more than $0.5T_m$, the material in and around the stir zone will undergo precipitate dissolution and coarsening.

Ma et al [151] performed FSP on cast light alloys including Mg-Al-Zn alloys. They brought out two main functions of FSP are; i) refine, homogenize the microstructure and densify the maerial and ii) to dissolve β particles in to magnesium matrix. The threaded pin during FSP induce plastic deformation at very high strain rate and strain of the order of 10^2 s^{-1} and 40. The peak temperature under the pin was measured in the range of 300 - 420ºC. This temperature, strain and strain rate resulted in recyrstallization, severe break-up of β particles and supersaturation of α-Mg. The increased dislocation density cause pipe diffusion to occur which increases the diffusion rate of Al in Mg by 1000 times. Due to broken precipitates, FSP also reduces the diffusion distance of Al considerably and hence reduces the time required for complete dissolution of Al. Feng and Ma [152] performed FSP on cast Mg-Al-Zn and found significant breakup and dissolution of β particles, with 89 % of Al dissolve into the α-Mg matrix and remarkable grain refinement. Traditional solution treatment method requires approximately 40 hours for complete dissolution of Al in Mg due to slow diffusion [153] but during FSP, the dissolution of β-precipitates in α-Mg happened in minutes due to the frictional heat raising the local temperature to the eutectic melting point. Similar observation was reported by Darrus et al [154] after FSP on AZ31 Mg alloy.

Though the reasons given by many authors for reduced volume fraction and finely distributed β-particles after FSP were dissolution and mechanical break-up, Robson et al [155] found that the high diffusion rate of Al due to broken up precipitates by Ma et al [151] was an unreliable argument as it is inconsistent with the fundamental studies carried out by Kilpatrick and Balluffi [155]. So, in his work, the pin was deliberately broken and the material was quenched rapidly to freeze the microstructure. The frozen microstructure revealed no broken up particles but eutectic melting which indicated the occurrence of partial melting followed by dendritic growth.

Yuan et al [156] performed single pass and two pass FSP on cast AZ91 Mg alloy. The large plate like precipitates and porosity in the as-cast microstructure were eliminated completely. There was considerable grain refinement due to DRX after FSP but the grain size was larger (2.8 μm) than that obtained after second pass (0.5 μm) and the microstructure was heterogeneous in single pass FSP. Primary reason for the difference between microstructure obtained was the initial microstructure before first and second pass. The smaller grain size after second pass FSP was attributed to homogeneous distribution of finer β-particles which pins boundary migration and hinders the grain growth. Similar results were observed in pure Al after single and double pass FSP by Yadav and Bauri [157].

2.6 Deformation mechanism responsible for FSPed microstructure

Park et al [158] studied the microstructure evolution during FSP of thixomolded AZ91 Mg alloy. Homogeneous, fine grained and supersaturated α-Mg was obtained after FSP due to DRX as the peak temperature obtained during the process was higher than the material's recrystallization temperature. The two types of DRX that influence Mg alloys during FSP are DDRX in which grains nucleate followed by grain growth and CDRX in which the LAGBs gradually deforms to HAGBs. Moreover, CDRX requires less activation energy when compared to DDRX [159]. The orientation of grains, stacking fault energies and stored strain energy are the factors influencing the type of DRX. Grains with high Schmidt factor are easy to deform, so they are called soft orientations which are capable of achieving large strain and stores large strain energy. The converse is true for hard orientations. Similarly, lower stacking fault energy materials are susceptible to stacking faults which blocks dislocation slip and store strain energy. On the other hand cross-slip is easy in high stacking fault energy materials. It means low SFE can store high strain energy and favors DDRX while high SFE facilitate deformation and assists CDRX [160].

Yadav and Bauri [161] studied the reason for grain refinement after FSP in commercially pure aluminium. TEM studies revealed dislocations, generated due to deformation during FSP, were piled-up in a particular plane due to dynamic recovery and form LAGBs. These LAGBs converted to HAGBs due to dynamic recovery of the dislocations [162]. In AZ91 Mg alloy, during FSW, grain refinement due to discontinuous DRX, was simulated and compared with experimental results by Asadi et al [163].

Chai et al [164] studied the deformation mechanism during FSP on AZ91 Mg alloy under two conditions. First one was FSP in air and second was FSP under water. The grain refinement and properties were better achieved in the case of underwater FSP. Based on microstructure, deformation temperature and a model criterion based on critical value for nucleation they predicted CDRX as deformation mechanism in air FSP while both CDRX and DDRX operated in underwater FSP.

Tripathi et al [165] reported a mechanism for the microstructural origin during FSP of AZ31 Mg alloy. Initially the coarse grains sheared off in to thin circumferential bands then equiaxed grains developed at HAGBs between these layers. These equiaxed grains undergo rapid grain coarsening up to 2 to 4 μm by slow cooling. In case of rapid cooling, grain sizes were only few 100 nm in which case the deformation was accommodated by GBS as in superplastic deformation.

2.7. Influence of FSP on mechanical properties

2.7.1 Tensile properties

Most of the factors that influences FSP, namely, process parameters, cooling and number of passes have a significant effect on the microstructure and texture of the FSPed material. Microstructure and texture considerably controls the mechanical properties of the material. The effect of process parameters of FSP were discussed in detail in section 2.4.3. It gave an idea that low rotational speed and high traverse speed produces sound weld and fine grain microstructure.

Similarly, Valle et al [166] studied the tensile properties of AZ91 Mg alloy after FSP by different cooling methods. As the effect of cooling increases the grains become finer and the yield strength increased.

Table 2.4: Tensile properties of as-cast and FSPed AZ80 Mg alloy [167].

Conditions	Yield strength (MPa)	Ultimate tensile strength (MPa)	Elongation (%)
As-cast	84.1	120.9	4.1
As-cast + solutionizing	94.3	176.5	8.8
Single pass FSP	134.6	188.8	3.0
Single pass FSP and then aged	156.5	213.3	1.2
Solutionized and then FSP	109.2	308.8	25.2
Aged and then FSP	169.2	336.5	16.8
Two pass FSP	136.7	327.3	25.0
Two pass FSP and then aged	192.8	355.7	17.0

Feng et al [167] studied the effect of solutionizing and aging treatment on AZ80 Mg alloy both before and after FSP. The results of their work are shown in the Table 2.4. Yuan et al [156] studied the effect of aging after FSP on AZ91 Mg alloy. The results of their work are shown in the Fig.2.9. FSP on solution treated and aged alloys showed significant improvement in the strength and ductility when compared to the FSP on as-cast alloy. However, improvement in strength of post FSP aged materials were negligible with a reduction in percentage elongation.

Jamili et al [168] studied the effect of texture in enhancing the strength of FSPed WE43 Mg alloy. They found that grain refinement, second phase dissolution as well as texture hardening also reason for the improvement in mechanical property. In ZKX50 Mg alloy the tensile strength of FSPed material was not observed to follow Hall-Petch relation, instead the strengthening mechanism was attributed only to the texture formation [169]. In rolled magnesium alloys, initial basal texture was found to become random texture which resulted in reduction of strength. Woo et al [170] studied the tensile properties of rolled AZ31B Mg alloys after FSP and correlated with texture obtained through neutron diffraction measurements. The base metal possess rolling texture with high intensities of basal plane normal, parallel to normal direction. After FSP, the basal texture was weakened at the stir zone and reduces the yield strength. Yu et al [171] also found that the strength of FSPed plated were found to be lesser than the hot rolled plate while the ductility improved with decreasing heat input due to favorable orientation of basal slips with Schmidt factor 0.5 in hot rolled AZ31B Mg alloy. In a work by Woo et al [172] the reduction in yield strength in the process direction was attributed to the reduced residual stress along the process center line.

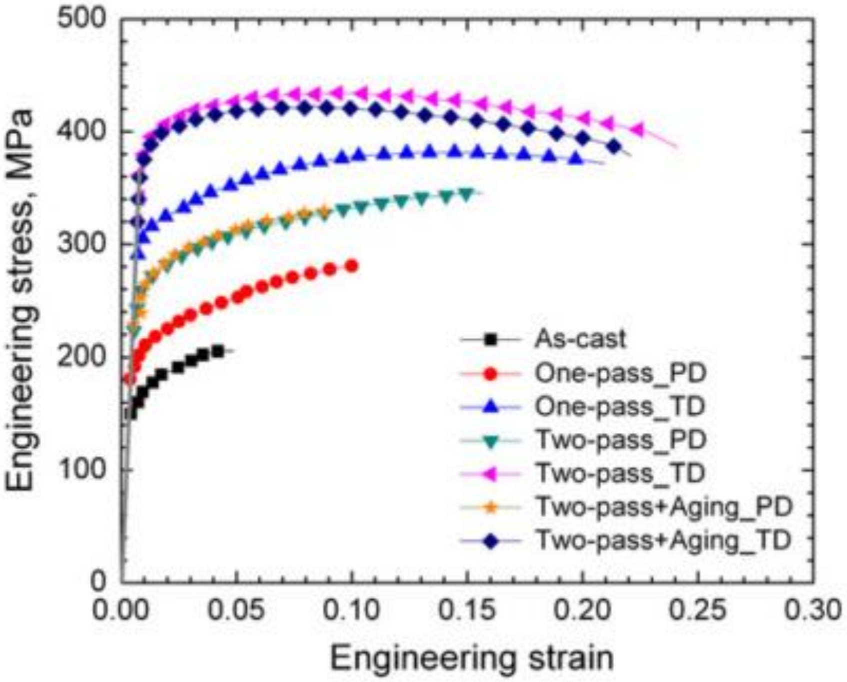

Fig. 2.9: Stress–strain curves of as-cast and friction stir-processed AZ91 Mg alloy [156].

In case of cast Mg alloys, basal texture was predominant on the plane normal to processing plane [137,173] after FSP. Jain et al [173] found yield anisotropy in FSPed AZ91 Mg alloy. The yield strength was found to be more for samples with tensile axis parallel to transverse direction when compared to the samples with tensile axis parallel to process direction. The anisotropy was due to strong basal texture in process direction tilted 30-40° with respect to the normal direction. Ageing treatment of FSPed samples found to reduce the yield anisotropy ratio to 1.12 from 1.73 due to twin-precipitate interaction while deforming the samples in process direction [174].

2.7.2 Fracture toughness

The fracture toughness of Mg and its alloys in as-cast condition as well as after grain refinement methods were studied scarcely, even though acoustic emission methods were also used to evaluate K_{IC} value of AZ91 Mg alloy [175]. Guao et al [176] studied the effect of grain refinement on fracture toughness of AZ31 Mg alloy and found that for the decrease in grain size from 32.2 to 9.4 µm the K_{1C} value increased from 17.9 to 18.6 MPa √m. Similarly, the effect of grain size on the fracture toughness of ECAPed AZ31 Mg alloy was studied by Xia et al [177]. As the grain size varied from 16.47 µm to 1.75 µm the fracture toughness value increased from 21.1-28.6 MPa √m. Dadashpour et al [178] evaluated fracture toughness of FSPed AZ91 Mg alloy and reported in the range of 13 – 16 MPa √m.

2.7.3 Fatigue

The fatigue properties of as-cast Mg and Al alloys are prone to casting defects [179]. Munoz et al [180] artificially created pores and surface defects in an aluminum alloy. It was observed that the stress and strain concentration surges when pores interact with surfaces. The pores interaction with surfaces were also proved by finite element methods [181,182]. Sharma et al [183] found improvement in the fatigue properties A356 aluminium alloy after FSP. The cast A356 alloys contained α-Al, eutectic Al-Si particles with size of nearly 80 µm and high volume fraction of porosity. After FSP, the Si particles were broken-up and distributed uniformly and also the porosities were reduced considerably. It leads to improvement in the fatigue property of approximately 80 %.

Tajiri et al [184] also studied the fatigue properties of A356-T6 alloy after FSP using two rotational speeds, 500 and 1000 rpm. The fatigue properties were improved after FSP, the lower tool rotational speed enhanced the fatigue properties further when compared to the higher rpm. Ni et al [185] found improvement in fatigue property of AZ91 Mg alloy after FSP due to grain refinement, elimination of coarse β particles and porosities. In addition to high cycle fatigue test Cavaliere and Marco [186] performed fatigue crack growth test in FSPed AZ91 Mg alloy. The calculated crystal plasticity size at the crack tip was equivalent to the pore size in as-cast material whereas after FSP the crystal plasticity size becomes 10 times the grain size. So, for crack to grow, the plastic region in front of crack had to cross 10 grains. This confirmed finer grains improved the fatigue properties.

However, exceptions in the improvement in fatigue property after FSP was observed by Afrinaldi et al [187] while performing FSP on extruded flame resistant Mg alloy AMX602. Though the microstructure was modified after FSP, neither the hardness followed Hall-Petch relation nor the fatigue property was enhanced. The strong texture with high Schmidt factor after FSP was the reason for reduced mechanical properties. Similar to tensile properties, anisotropy in fatigue properties was also observed due to strong texture formation [188].

The crack path during fatigue failure of as-cast or aged AZ91 materials displayed deflected crack path due to the presence of interdendritic regions and coarse grains whereas the FSPed materials failed with fracture along a straight line due to its fine grain nature [189]. They emphasized that the banded structure formed during FSP had no effect on the fatigue failure.

2.7.4 Superplasticity

Improvement in superplasticity through FSP on Al and Mg alloys have been explored comprehensively. The FSPed microstructure with fine and stable grains exhibited exceptional superplasticity when compared to unmodified alloys [190–192]. The literature data on the superplasticity of AZ91 Mg alloy after grain refinement method was presented in the Table 2.8. The conventional methods, namely, FSP, ECAP and high speed rolling with differential speed ratio (HSDSR) yield finer grain sizes and larger elongation when compared to the traditional rolling and extrusion. Grain boundary sliding was responsible deformation mechanism in Mg and its alloys meanwhile grain growth and cavities coalescence was reported as main failure mechanism during superplastic deformation. Cavities observed to nucleate at large particles and excessive cavities coalescence occurred at large strain of about 1.5 [193].

Table 2.5: Literature data on high temperature superplasticity of AZ91 alloy

Grain size (μm)	Processing technique	Test Temperature (K)	Elongation to failure (%)	Reference
0.5	FSP	473	350	[194]
0.7	FSP	473	350	[194]
0.7	ECAP	423, 448, 473, 523	650	[195]
0.8	ECAP	473, 523, 573	560	[67]
0.9-1.4	HSDSR	473, 493, 523, 553	550	[196]
1.2	FSP	573, 628, 648	1200	[197]
1.7	Extrusion	548	350	[198]
3	FSP	573, 623	1600	[199]
3.1	ECAP+HT	448, 473, 523	950	[195]
4	FSP	498, 523, 548, 573	1050	[200]
5	Extrusion	523, 548, 573	420	[201]
6.3	Extrusion	493, 553, 573	550	[196]
7.2	Extrusion	573, 598, 623, 648	512	[202]
7.6	Chips Extrusion	573	230	[203]
7.8	FSP	623, 648	554	[197]
9.1	Extrusion	573	300	[201]
11	Rolling	623, 678, 698	450	[204]
16.4	Extrusion	573	150	[201]
30	Rolling	573, 598, 623, 648, 673	200	[205]

2.8 Property enhancement by grain size inhomogeneous microstructure

Mansoor and Ghosh [206] studied the effect of multi-pass FSP on extruded ZK60 Mg plate. They found improvement in room temperature mechanical properties of processed alloy, which was attributed to layered micro-structure with grain size of 2–5 μm and 100 μm as in the Fig. 2.10.

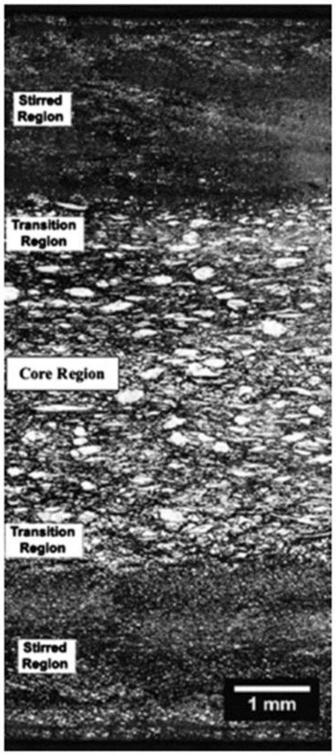

Fig. 2.10: Microstructural collage of layered microstructure in ZK60 Mg alloy generated by multipass friction stir processed [206].

Similarly, Witkin [207] and Oskooie et al [208] worked on Al alloys through cryo-milling and high energy planetary ball milling methods respectively to fabricate mixed coarse and fine grain structures and obtained optimum strength and ductility. Wang et al [209] achieved enhanced strength and ductility in Cu after thermomechanical treatment with a mixed grain size distribution of micrometre-sized grains embedded inside a matrix of nanocrystalline and ultrafine (<300 nm) grains. The matrix grains impart high strength whereas, the coarse grains facilitate strain hardening mechanisms to give high tensile ductility. Moreover, modifying the surfaces were reported to improve fracture and fatigue properties. Caceres and Selling [210] mentioned that the area fraction of defects on the fracture surface influences the tensile properties rather than the bulk defect content. Begum et al [211] found that that the fatigue cracks were originated from the surfaces with large grains. Perron et al. [212] performed molecular dynamic simulation on polycrystalline Al samples and found a linear relationship between grain size and surface roughness to an extent of applied strain, while, Liu et al [213] reported that surface modification by shot peening decreases surface roughness due to grain refinement and becomes reason for improvement in mechanical properties in Mg alloy.

At high temperature, the effect of fine grains is substantial, even room temperature superplasticity was observed after HPT in pure Mg [65] and in Mg-Li alloy [214]. However, few studies showed superplasticity in coarse grain Mg alloys also. Watanabe et al. [215] achieved superplastic elongation of 196% in AZ31 Mg alloy with an average grain size of 130 µm. Wu and Liu [216] reported superplasticity of 320% in hot rolled AZ31 Mg alloy with a mean grain size of 300 µm. Although, grain size was found to reduce to 25µm during deformation due to dislocation slip and climb. Hence the idea of mixed grain size microstructure which showed promising improvement in room temperature mechanical properties were explored at high temperature also. Fan et al [217] observed more superplastic elongation in AA8090 Al-Li alloy which inherently contain three distinct microstructural layers through the thickness when compared to superplasticity of surface layers (equi-axed grains) and middle layers (elongated grains) alone. Pancholi and Kashyap [218] obtained better bulge profile during superplastic bulge forming of AA8090 Al-Li alloy. Later, Pradeep and Pancholi [219] deliberately fabricated layered microstructure containing coarse and fine grains in Al 5082 alloy using FSP and found that the inhomogeneous microstructures possess superior superplastic formability than the homogeneously grain sized materials. Álvarez-Leal et al [220] observed superplasticity in extruded ZK30 Mg alloy. During deformation the complex as received microstructure evolved into bimodal microstructure.

2.9 Summary of literature review

The summary of the literature review is presented below;

1. The strength as well as ductility of Mg and its alloys can be improved by FSP.
2. FSP has potential to eliminates casting defects and modify microstructures either locally or in bulk.
3. Bimodal grain size or layered inhomogeneous microstructures showed better mechanical properties than homogeneous fine grain microstructure.

2.10 Literature Gap

Critical review of the literature suggested that there are few gaps in the understanding of FSP of Mg alloys and effect of selective microstructural modification on mechanical properties. Few of the gaps are highlighted below;

1. FSP has been tried mostly on Al alloys or wrought Mg alloys however, few studies are reported on cast Mg alloys.
2. Effect of almost all the processing parameters of FSP on microstructure and properties is reported but effect of tool pin length is hardly investigated.
3. Mostly mechanical properties are studied after single pass or 100 % overlapped multipass FSP – that implies limited volume of material is processed and studied.
4. Effect of layered coarse and fine grain microstructures on fracture toughness and fatigue behaviour is rarely reported.
5. Research work on influence of texture on mechanical behaviour after FSP are few, especially in cast Mg alloys.

2.11 Objective

The objective of the work was intended;

i) to obtain microstructural modifications in an as-cast AZ91 Mg alloy using multipass FSP; only on the surfaces, through half of the thickness and through the full thickness.

ii) to study the efect of this FSP modified microstructure, containing layers of fine grain and as-cast microstructure on the mechanical properties, namely, tensile strength, fracture toughness, fatigue and superplasticity.

iii) to study the influence of microstructure and texture on the mechaical behavior and

iv) to explore the deformation mechanisms operating in the layered microstructure of AZ91 Mg alloy.

Material

Solution and heat treatment of as-cast alloy

Multipass friction stir processing

Mechanical testing methods

Characterization techniques

CHAPTER 3

MATERIAL AND METHODS

OVERVIEW

The material used and experimental methods are described. The experimental methods are divided into 4 sections. First section describes solution and heat treatment method. Second section describes about the method to generate layered microstructure using friction stir processing. Third section detailed about the material testing methods (room temperature tensile test, fracture, fatigue, and high temperature tensile test). The fourth section describes about the material characterization techniques used in this work.

CHAPTER 3

MATERIAL AND METHODS

3.1 Material

The material used in this work is AZ91 Mg alloy which contains approximately 9 wt. % of Al and 1 wt. % of Zn. The as-cast AZ91 Mg alloy billets were received from Hindustan Aeronautics Limited (HAL). The billets were machined in to plates of size; 10 mm thick, 100mm wide and 110 mm length and used for processing and experiments.

3.2 Solutionizing and aging of as-cast alloy

In order to understand the mechanical behavior of as-cast AZ91 Mg alloy, tensile and fracture toughness was performed on as-cast AZ91 alloy and also in its T4 and T6 treated conditions. T4, is a solution treatment method to dissolve the brittle β-phase in as-cast alloy in to the α-Mg matrix. As shown in Fig 3.1 the as-cast alloy need to be heated up to 416 ºC, hold in the same temperature, inside a furnace for 24 to 48 hours and air quench to get the solution treated AZ91 alloy. To optimize the time for T4 solution treatment 9 samples were heated to 416 ºC and held them for different durations starting from 16 hours to 48 hours at an interval for 4 hours. The samples were air cooled immediately after the specific samples holding time and characterized.

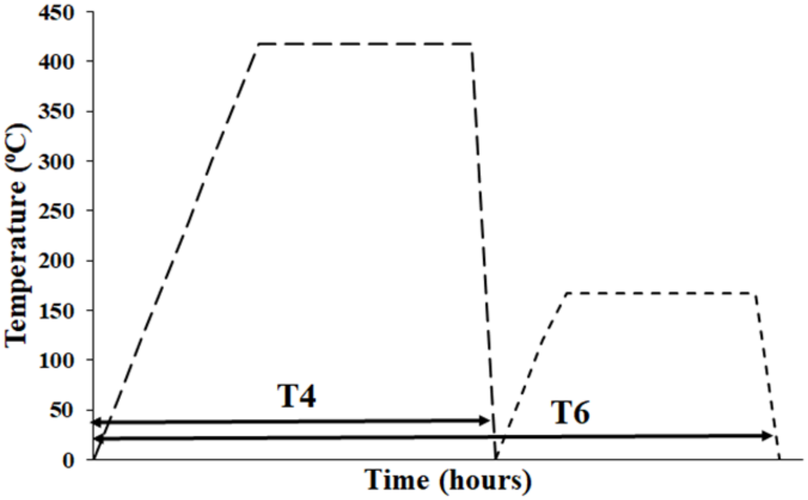

Fig. 3.1: Schematic temperature profile of T4 and T6 treatment.

T6 aging heat treatment was performed after T4 solution treatment. The material in T4 condition was heated up to 165-170 ⁰C, held it in furnace for up to 24 hours and cooled it in air to get age hardened AZ91 Mg alloy. Similarly, the six of the optimized T4 solution treated samples were heated up to 167 ⁰C and holding them for different durations starting from 4 hours to 24 hours at an interval of four hours. The samples were then air cooled and characterized.

3.3 Multipass FSP

The machined plates were subjected to multipass FSP at a tool rotational speed of 720 rpm and a traverse speed of 150 mm/min with a tool tilt angle of 3°. During FSP, copper backing plate was used to avoid tunneling defect by effective transfer of heat generated due to friction between the tool shoulder and the sample.

Table 3.1: Experimental conditions used to obtain microstructural variation in through thickness direction to study room temperature mechanical behavior.

	Processing configurations		
	HFG (half thickness fine grained microstructure)	**SFG (surface modified fine grained microstructure)**	**FFG (full thickness fine grained microstructure)**
FSPed surface	Processed on one surface	Processed on both surfaces.	Processed on one surface
FSP tool pin height	5 mm	4 mm	7 mm
Material removed after FSP	2 mm from both the surfaces	2 mm from both the surfaces.	1 mm from top and 3 from bottom surface.
Final condition of 6 mm thick plate	Top 3mm FSPed and bottom 3 mm as-cast (AC).	Top and bottom 2 mm FSPed. Middle 2 mm AC	Full Thickness, 6 mm, FSPed

Tools with same shoulder diameter of 28 mm and threaded conical pin of diameter 8 mm at shoulder and 4 mm at tip but with different pin lengths were used. The pin lengths were designed to control the extent of microstructure variation required in through thickness direction. The FSP was performed on 10 mm thick plate because during preliminary experiments it was observed that thin plates (below 8mm) cracked while performing multipass FSP, probably due to lower ductility of AZ91 Mg alloy. The experimental details to generate layered microstructure to study room temperature and high temperature mechanical behavior are presented in Table 3.1 and Table 3.2 respectively. Approximately, 70 mm of 100 mm width of the plate was processed, which required 30–35 passes with 50% overlap towards the retreating side.

Table 3.2: Experimental conditions used to obtain microstructural variation in through thickness direction to study high temperature mechanical behavior (superplasticity).

	Processing configurations		
	HFG (half thickness fine grained microstructure)	**SFG (surface modified fine grained microstructure)**	**FFG (full thickness fine grained microstructure)**
FSPed surface	Processed on one surface	Processed on both surfaces.	Processed on one surface
FSP tool pin length	5 mm	4.5 mm	5 mm
Material removed after FSP	3.5 mm from both the surfaces	3.5 mm from both the surfaces	1 mm from top and 6 mm from bottom surface.
Final condition of 3 mm thick plate	Top 1.5 mm FSPed and bottom 1.5 mm as-cast (AC).	Top and bottom 1 mm FSPed. Middle 1 mm AC	Full Thickness, 3 mm, FSPed

3.4 Mechanical testing

3.4.1 Room temperature tensile test

Tensile specimens with gauge dimensions of 25 mm×6mm×6mm were machined parallel to the processing direction according to the standard ASTM B557M.

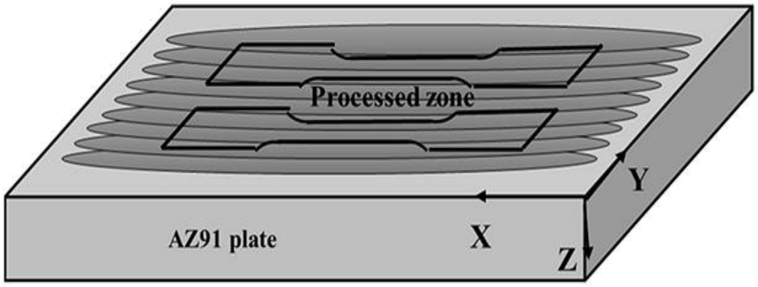

Fig. 3.2: Schematic of multipass FSPed plate with location of tensile sample for room temperature tensile test.

The cross head speed of 1.5 mm/min was used to conduct tensile test at a strain rate of 1×10^{-3} s^{-1}. The tensile sample for room temperature tensile test and its location from FSPed plate is shown in the Fig. 3.2. The directions X, Y and Z are process direction, transverse direction and thickness direction respectively.

3.4.2 Fracture toughness test

The fracture toughness tests were performed using the single edge notch bend (SENB) specimen or three point bend specimen. The sample dimensions were; thickness 6 mm, width 24 mm and span length of 100 mm, with notch parallel to the process direction in FSPed samples. The SENB sample and its notch details are shown in Fig. 3.3(a) & (b) respectively. The notches were made using CNC wire-cut electro – discharge machining (EDM).

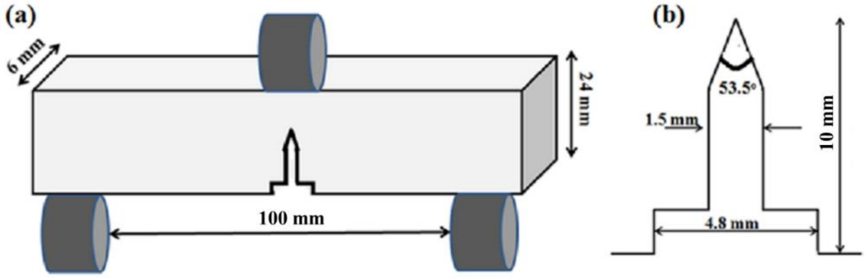

Fig 3.3: (a) SENB specimen for fracture toughness test, and (b) notch details.

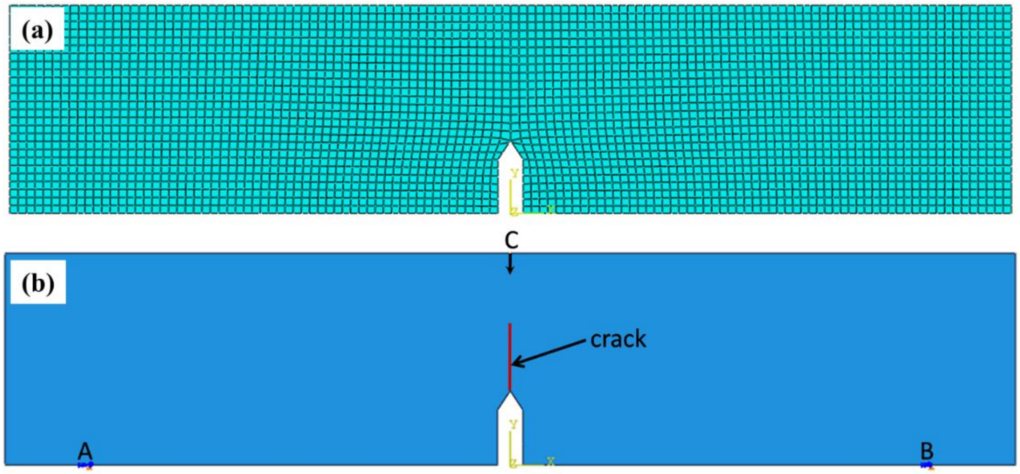

Fig. 3.4: SENB specimen geometry generated for XFEM analysis (a) showing meshes with 4 node quadrilateral element and (b) showing fatigue pre-crack position and boundary conditions.

To study the fracture toughness of received material in as-cast T4 and T6 conditions, J-integral test was performed. The SENB samples were fatigue pre-cracked before actual J-integral test. The fatigue pre-cracking was executed using increasing ΔK method. The fatigue pre-crack was started from the tip of 10 mm notch and up to half of the specimen width, i.e., 12.5 mm. Step reduction of load was done to keep the maximum ΔK under the predefined value, calculated according to the standard ASTM E1820. Then, the J integral test procedure was followed to obtain the J_{IC} value.

The experimental J test was simulated using extended finite element method (XFEM) in a finite element (FE) software Abaqus. A 2-D model of three point bend specimen was generated and four node quadrilateral elements are used to mesh the domain in which 6500 nodes as shown in Fig. 3.4(a). A crack of same magnitude obtained during pre-cracking was also considered in the meshed domain. The applied boundary conditions were same as in the experimental work. The lower edges of specimen at A and B points were constrained in all the directions as well as applied displacement boundary condition at point C as shown in the Fig. 3.4(b).

The fracture resistance behavior of layered microstructured material generated by FSP together with AC and fully FSPed material were compared using apparent notch fracture toughness (apparent K_Q) values. The layered microstructure material have variation in microstructure through the thickness, the pre-crack would not be uniform and it would violate the standard measurement of crack length. Hence, K_{IC} test was performed without precrack in the layered microstructured material. The cross head speed was maintained at 1.5 mm/min in order to correlate the fracture characteristics with the tensile failure.

3.4.3: Fatigue test

High cycle fatigue (HCF) test specimens with continuous radius between ends with 6 mm thickness, 12 mm width were used. Other dimensions related to specimen design are shown in the Fig.3.5. The specimen was designed according to ASTM E466 standard. HCF experiments were conducted at stress ratio, R=0 and at a frequency of 20 Hz under constant load controlled axial fatigue testing method at different stress amplitudes (σ_a).

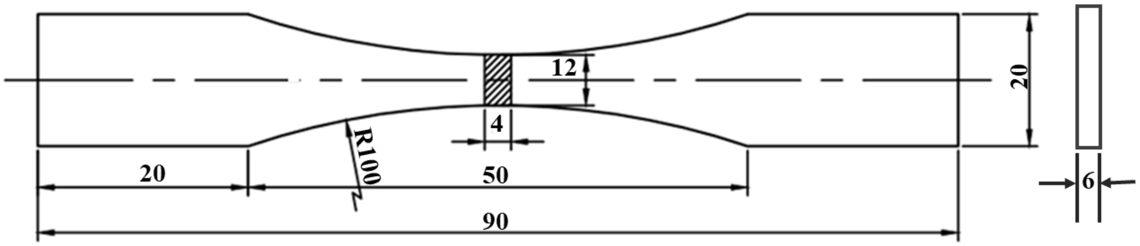

Fig. 3.5: Continuous fillet fatigue sample

All the room temperature mechanical tests were performed on Instron 8800 servo hydraulic testing system. Serrated hydraulic grips were used for tensile and fatigue test whereas three-point bend fixture was used for fracture toughness test. Bluehill, J-Integral, K_{1C} and Wavematrix were the software suites used for performing tensile, J-Integral, K_{1C} and fatigue test respectively.

3.4.4: High temperature tensile test

To study the superplasticity of layered microstructure material tensile specimens machined parallel to the processing direction as shown in the Fig.3.5. The gauge dimensions of specimens were 10 mm×6 mm×3 mm and tested at 350ºC. Tensile test was carried out at three different strain rates of 5×10^{-3} s^{-1}, 1×10^{-3} $s^{-1}$and 5×10^{-4} s^{-1}.

The final sets of experiments with nine samples were tensile tested at high temperatures to understand the nature of superplastic behavior of fully fine grain microstructured material generated by FSP. The sample dimensions were similar to that in Fig.3.6 and the tests were performed at three strain rates (5×10^{-3} s^{-1}, 1×10^{-3} $s^{-1}$and 5×10^{-4} s^{-1}) and at three different temperatures (150 ºC, 250 ºC and 350 ºC). Constitutive equation was developed using the test results and its parameters were analyzed with variation in strain to understand the microstructure evolution occurred during high temperature deformation.

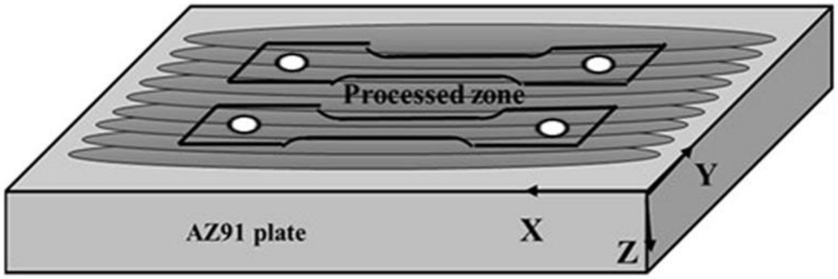

Fig. 3.6: Schematic of multipass FSPed plate with location of tensile sample for high temperature tensile test.

3.5 Material characterization

Microstructural characterization was carried out by optical microscope (Leica DMI 5000). Field emission scanning electron microscope (FESEM – FEI Quant 200F) was used for microstructural characterization, energy-dispersive spectroscopy (EDS) as well as for fracture surface characterization. Rigaku Smart Lab X-ray diffractometer was used for phase identification in AZ91 alloy before and after FSP. Analysis of diffraction peaks was accomplished using X'pert Highscore Plus software. The specimens for optical microscopy and scanning electron microscopy (SEM) were prepared by mechanical polishing using SiC papers with grit size in the sequence of 320, 800, 1200, 1500 and 2000 and water as lubricant. Subsequent polishing was performed using diamond paste of 6 µm, 3 µm and 1 µm and ethanol as lubricant. After mechanical polishing, etching was done by immersing the sample in acetic-picral solution (6 g picric acid, 5 ml acetic acid, 100 ml ethanol, 10 ml water) for 15–20 s.

For electron backscattered diffraction (EBSD) the sample surface was polished in Buhler Ecomet 250 grinder/polisher using chemomet cloth and 0.02 µm particle sized colloidal silica using methanol as lubricant. The EBSD analysis was performed in TSL OIM Analysis 7 software. The texture plots were obtained using harmonic series expansion with triclinic symmetry, series rank L=22 and Gaussian half width of 5°. The EBSD scans were taken from XZ plane before and after deformation in order to compare and understand both the microstructure and the microtexture aspects of the deformation process.

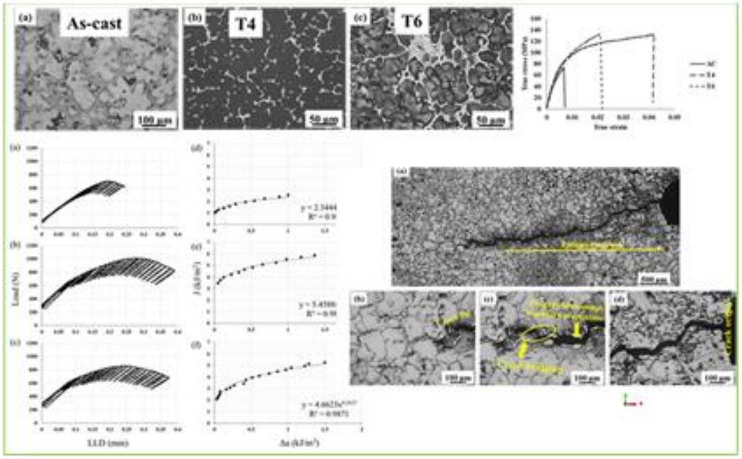

CHAPTER 4

MECHANICAL BEHAVIOR OF AS-CAST MATERIAL

OVERVIEW

The room temperature tensile and fracture toughness properties of AZ91 Mg alloy received from HAL were studied in its as-cast condition, as well as in T4 and T6 treated conditions.

CHAPTER 4

MECHANICAL BEHAVIOR OF AS-CAST MATERIAL

In this chapter, mechanical properties of AZ91 Mg alloy in as-cast condition, as well as in T4 and T6 treated conditions is presented. The temperatures for T4 and T6 treatment were selected from Mg-Al binary alloy phase diagram. Microstructures obtained after different holding times were studied to select holding time for T4 and T6 heat treatment. The as-cast (AC), T4 and T6 samples were tested to evaluate tensile and fracture toughness properties. The fracture toughness of the samples were studied by J-integral approach and finite element analysis was carried out to understand strain localization at the crack tip.

4.1 Results

4.1.1 Microstructure

The optical microstructure of the as-cast material is shown in the Fig. 4.1(a) and secondary electron image in Fig. 4.1(b). Both the images clearly show dendritic region (A) and interdendritic region (B). The microstructure contain dendritic region of 100 μm average size and interdendritic region with network of plate like precipitates. The elemental composition of regions A and B is presented in the Table.4.1. Fig. 4.1(b) in conjunction with Table 4.1 brings out that dendritic region (A) contains 94.8 wt. % Mg and 5.2 wt. % Al whereas, interdendritic region (B) contains 63.1 wt. % Mg, 34.4 wt.% Al and 2.5 wt.% Zn. Hence the dendrites are composed of α-Mg whereas the interdendrites are β-$Mg_{17}Al_{12}$ intermetallic precipitates.

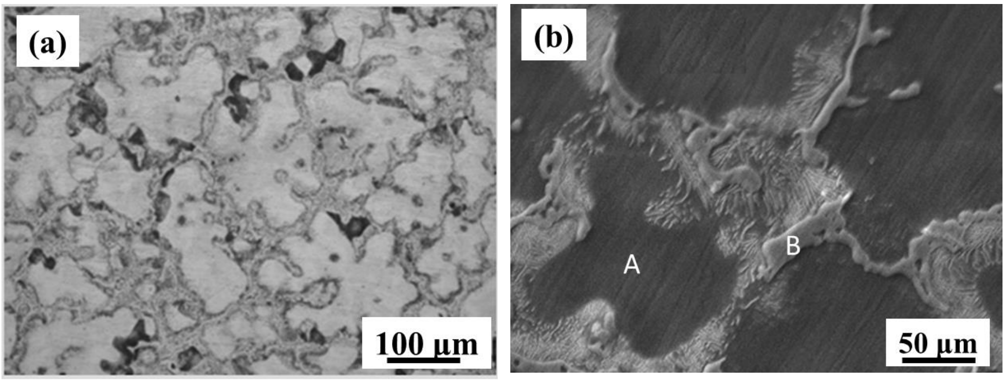

Fig. 4.1: Microstructure of as-cast AZ91 Mg alloy (a) optical image, (b) secondary electron image showing dendritic region (A) and interdendritic region (B).

Table 4.1: Elemental distribution in dendrites and interdendrites of as-cast AZ91 Mg alloy

	Mg (wt. %)	Al (wt. %)	Zn (wt. %)
A	**94.8**	**5.2**	**-**
B	**63.1**	**34.4**	**2.5**

The microstructures of the as-cast sample heated to 416 ⁰C and different holding times starting from 16 hours to 48 hours are shown in the Fig.4.2. The microstructures remain more or less similar up to the holding time of 36 hours. After holding time of 40 hours the dissolution of β-phase started and appear to be completed after 44 hours. The thick plate of β precipitates in the microstructure dissolved to give thin grain boundary network which remained similar after holding time of 48 hours. Hence, the T4 solution treatment was given by heating the samples to 416 ⁰C in a furnace, hold them for 48 hours and air cooled.

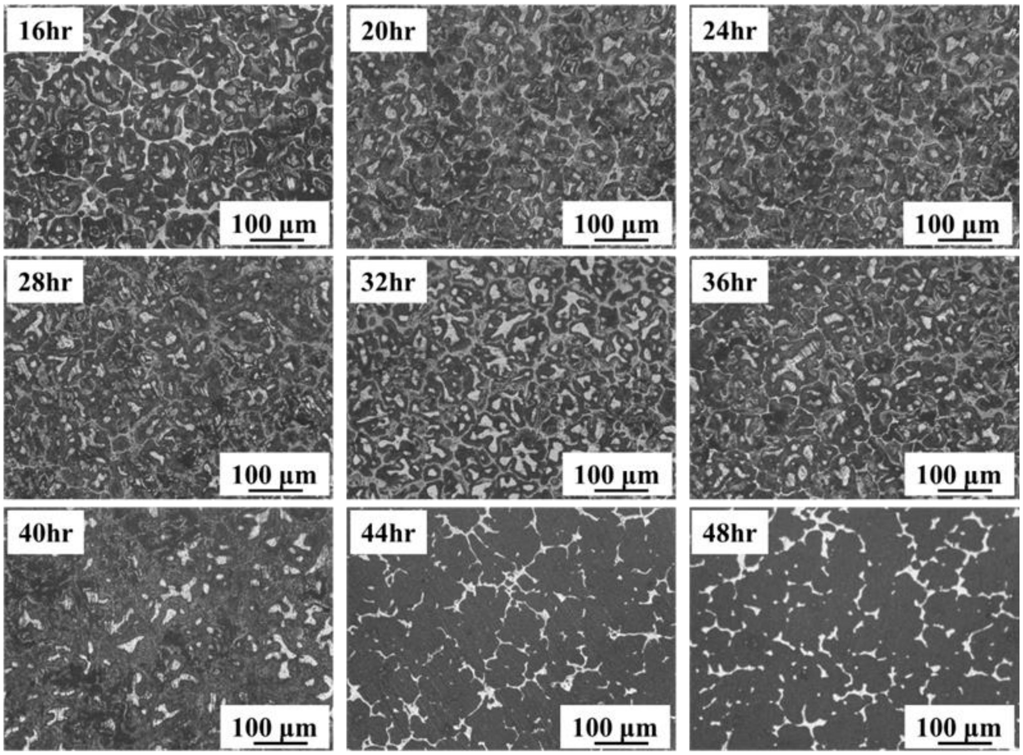

Fig. 4.2: Microstructures of T4 solution treated samples obtained after holding different time at 416 ⁰C and air cooled.

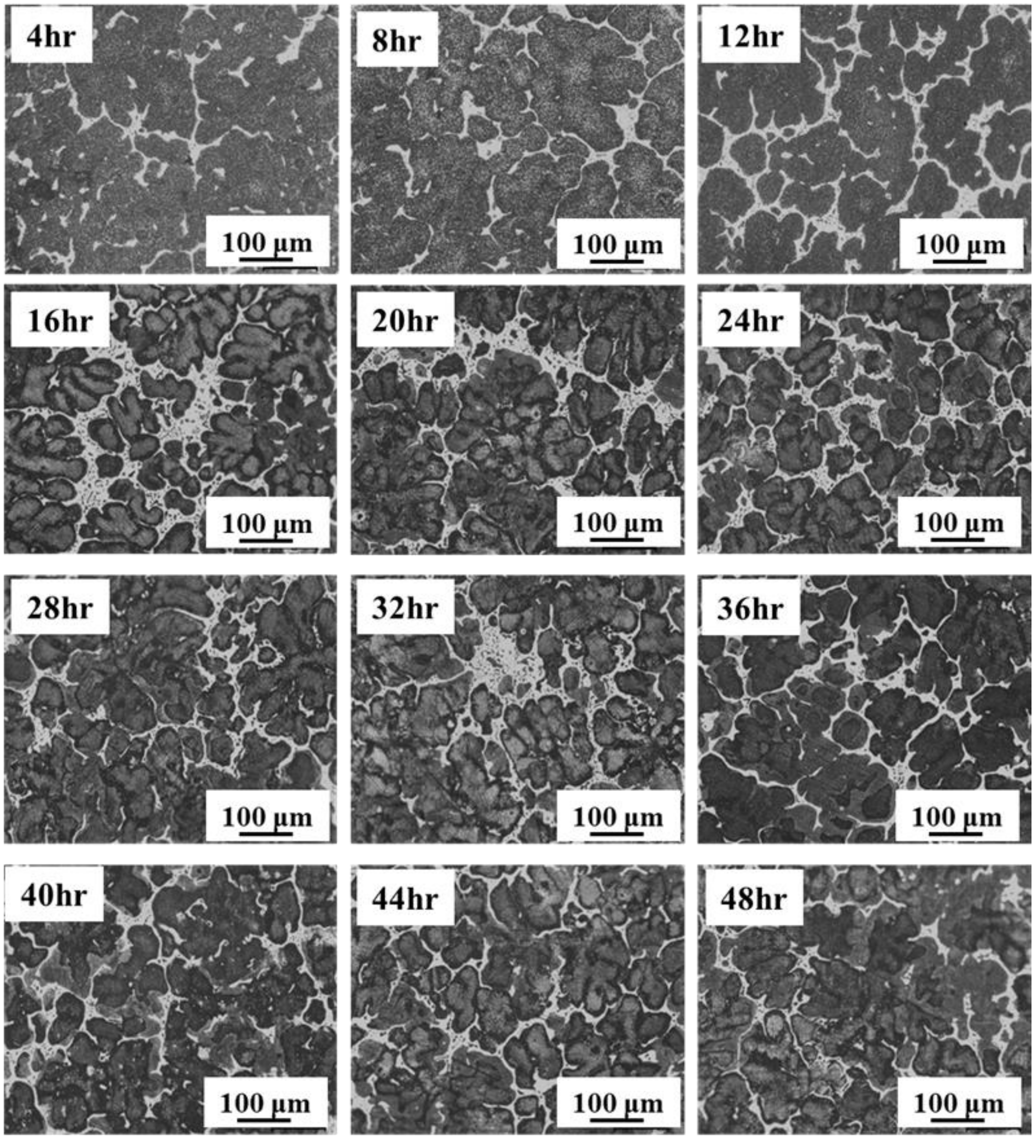

Fig. 4.3: Microstructures of T6 heat treated samples obtained after different holding time at 167 ^{0}C and air cooled.

Similarly, for T6 aging treatment the T4 solution treated samples were heated to 167^{0}C and held for different time durations from 4 hours to 48 hours. The microstructures of the samples are shown in the Fig. 4.3. Gradual thickening of the β phase occurred between 4 to 12 hours of holding time. After 16 hours of holding time, coarse network of β-particles are ostensible with some particles in the α-matrix because of re-precipitation due to aging treatment. The microstructure remained almost similar between holding time of 16 hours to 48 hours. Hence, for T6 heat treatment, the T4 solution treated samples were heated to 167 ^{0}C in a furnace and held them for 24 hours and air cooled.

The microstructures of as-cast, T4 and T6 conditions are shown in the Fig. 4.4(a), (b) and (c) respectively. Samples with these microstructural conditions were tested for tensile and fracture toughness properties.

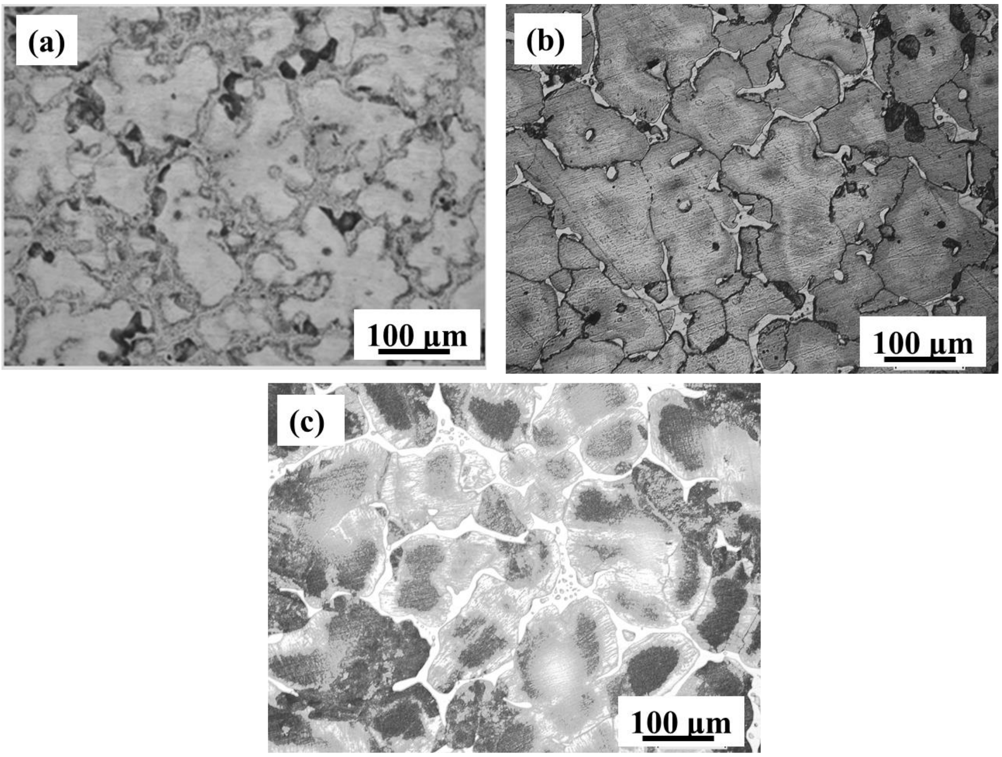

Fig. 4.4: Optical microstructures of AZ91 Mg alloys in (a) as-cast and after (b) T4, and (c) T6, heat treatment.

4.1.2 Tensile properties

The tensile properties of AZ91 Mg alloys in as-cast, T4 and T6 conditions were tested and the true stress vs true strain curves are presented in Fig.4.5. The as-cast material showed lowest tensile properties of 80 MPa and 0.8 % elongation. Solution treated (T4) sample due to solid solution strengthening and absence of brittle network of β-phase showed comparatively higher strength and elongation of 132MPa and 4 % respectively. The T6 sample which was solution treated and then aged showed similar tensile strength, 130 MPa, as that of T4 sample but its elongation reduced to 2 % due to the re-precipitation of the second phase β-particles. The effect of as-cast microstructure, solution treatment and aging on the mechanical properties can be observed from the fractographs. The fractograph of as-cast material in Fig. 4.6(a) shows clear facets in between the brittle fractures of interdendrites. In the fractograph of T4 sample (Fig.

4.6(b)) facet morphology is different from that in Fig. 4.6(a). However, quasi-cleavage features are more prominent which suggests small amount of plastic deformation before fracture.

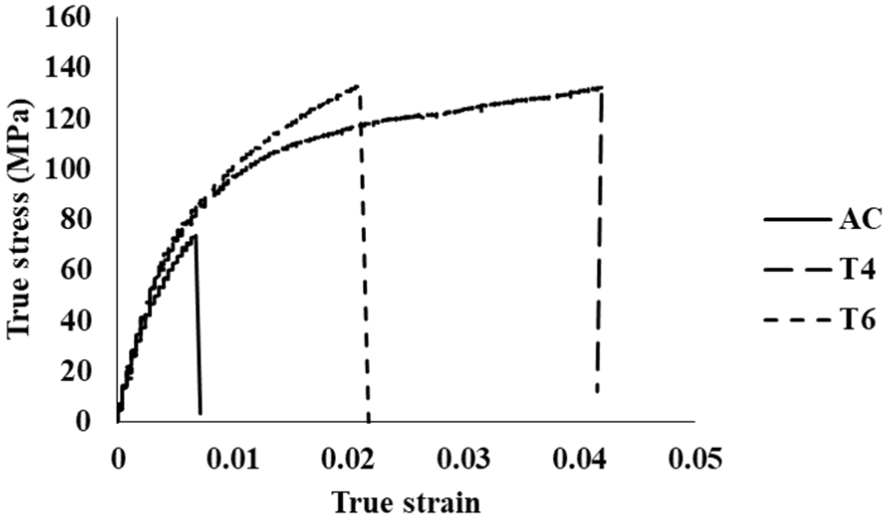

Fig. 4.5: True stress versus true strain curve of received material in as-cast, T4 and T6 conditions.

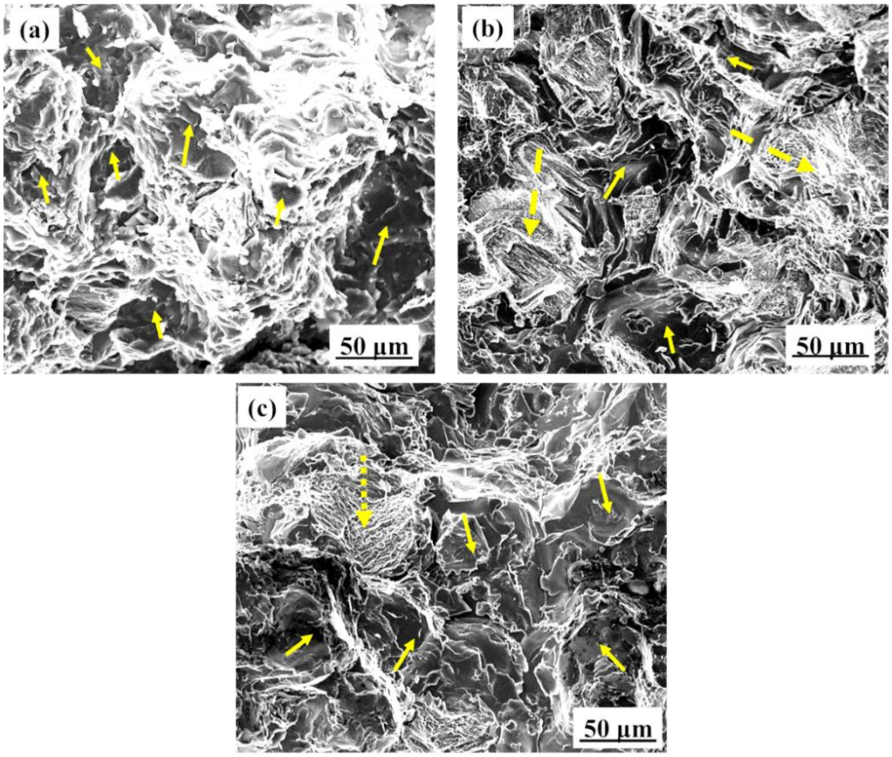

Fig. 4.6: Fractograph of tensile tested specimen with cleavage facets indicated by solid arrows in (a) as-cast, (b) quasi cleavage by long-dashed arrows in T4 condition (c) river patterns by short-dashed arrow inT6 condition.

The fractograph of T6 sample in Fig. 4.6(c) contain prominent facet morphology and river patterns. This is probably due to the re-precipitation of β particles along the boundaries and also inside the matrix as visible in the microstructures in Fig. 4.4(c). Zindal et al [221] observed the presence of precipitates in the grains and along the grain boundaries after aging in Mg-8Al-0.5 Zn alloy. In another work by the same author in same material, presence of both intergranular and transgranular fracture was observed when the alloy was aged at lower temperatures (≤200°C) [222]. Hence, it is clear that the solution treated samples have good combination of strength and ductility due to solid solution strengthening and because of the dissolution of β-phase and accompanied reduction in fraction of brittle interdendrites respectively.

4.1.3 Fracture toughness

The SENB specimen presented in Fig.3.3 was subjected to J-integral test after fatigue pre-cracking. J-integral represents the method to calculate amount of energy or work required to create a unit fracture area. It can also be viewed as a stress intensity factor [223].

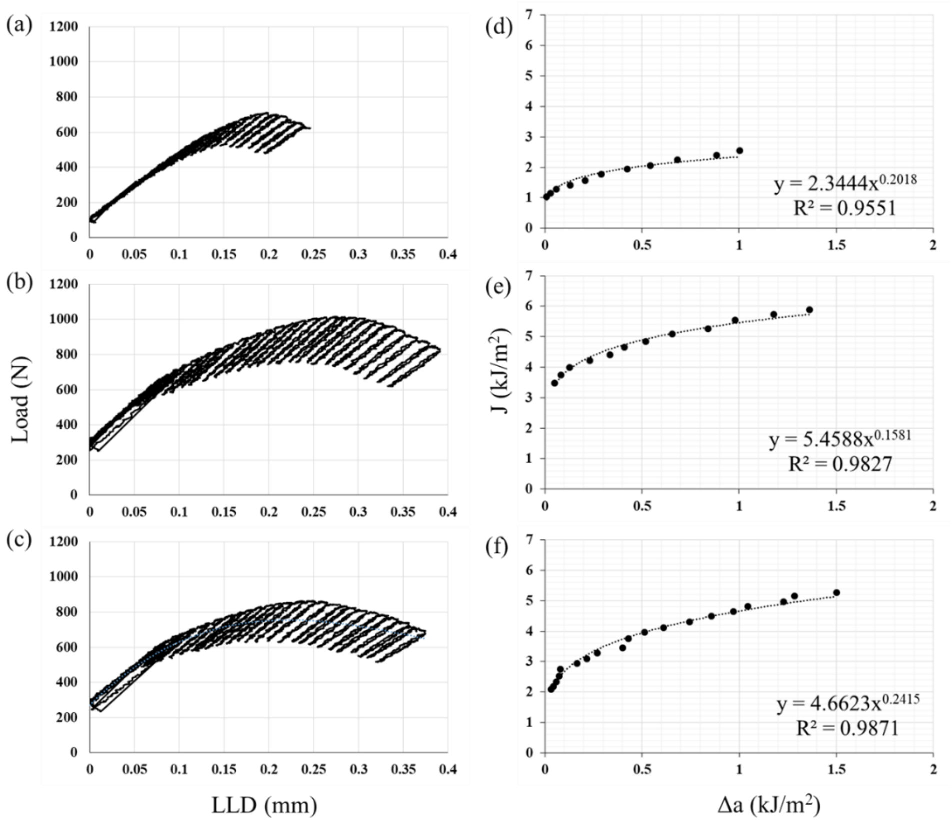

Fig. 4.7: Load vs. LLD curve of (a) as-cast, (b) T4 & (c) T6 and J vs. Δa curve of (d) as-cast, (e) T4 & (f) T6 sample.

The critical fracture energy J_{1C} defines the point at which instability or large-scale plastic yielding occurs during crack propagation under mode one loading. In order to maintain the path independency of J-integral calculation, proportional loading (loading and unloading) were maintained as shown in a load versus load line displacement (LLD) plot in Fig. 4.7. The maximum load attained by as-cast material was 720 N and LLD of 0.25 mm (Fig. 4.7(a)). The T4 sample attained maximum load 1000 N and a LLD of 0.39 mm (Fig. 4.7(b)), while the T6 specimen attained 810 N and 0.37 mm (Fig. 4.7(c). The LLD was measured using crack opening displacement (COD) gauge.

J-integral (kJ/m^2) value was calculated at every load and corresponding crack growth (Δa) was measured to construct J vs Δa curve. The crack measurement was performed by using compliance technique. The test data were qualified according to ASTM E1820 standard [224] and by fitting the data to power law of the form in Eq. 4.1.

$$J = C_1 \left(\frac{\Delta a}{k}\right)^{C_2} \qquad 4.1$$

where C_1 and C_2 are constants and k=1 mm. The correlation coefficient of the least square fit should be greater than 0.96 and the power coefficient C_2 shall be lower than 1. The J_{1C} value of as-cast (Fig. 4.7(d)), T4 condition (Fig. 4.7(e)) and T6 conditions (Fig. 4.7(f)) were 1.7 kJ/m^2, 4.2 kJ/m^2 and 3.1 kJ/m^2 respectively as measured from the intersection point of the power law curve with 0.2 mm offset line. Thus, the material in solution treated condition had shown higher J_{1C} value among all the three conditions tested.

Similar to tensile properties, the T4 samples showed good crack resistance behavior. The strain distribution ahead of the crack tip was analyzed using extended finite element method (XFEM). A four node quadrilateral elements are used to mesh the domain in which 6500 nodes are generated. The applied boundary conditions are same as the experimental work. The lower edges of specimen are constrained in all direction. The tensile properties of Mg alloys and some of the data points of LLD vs load are taken as input for the simulation. The simulated results are showed in the Fig. 4.8. The distribution of strain is similar in all the cases but the maximum strain at the crack-tip was lowest (1.6%) in as-cast condition (Fig. 4.8(a)) and highest (2.18 %) in T4 condition (Fig. 4.8(b)). The T6 condition achieved a maximum strain of 2.12 % at the crack as observed from Fig. 4.8(c). The simulated maximum strain values of AC and T6 at the crack tip are approximately equal to the fracture strain during the uniaxial tensile test. (Fig. 4.5). The simulated maximum strain at the crack tip of T4 alloy is lesser than the fracture strain during uniaxial tensile test but almost same as that of T6 condition. It is because the continuum approach of finite element analysis failed to predict the microstructural features like crack bridging and quasi-static cleavage phenomenon. Hence it is clear that the dissolution of β-phase after solution treatment increases the materials strength, elongation and fracture toughness of the material but the improvements are not significant when compared to Al alloys and steels in high performance structural applications.

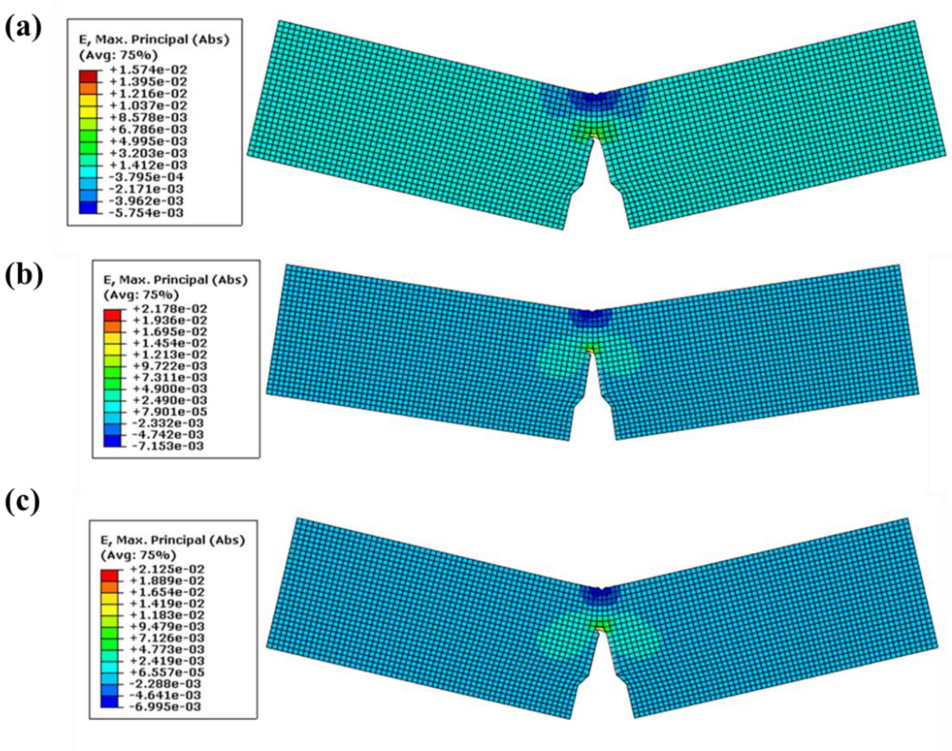

Fig. 4.8: Finite element analysis of strain distribution at the crack tip of (a) as-cast (b) T4 and (c) T6, SENB samples.

4.2 Discussion

The as-received AZ91 Mg alloy was tested for tensile and fracture toughness properties in its as-cast, T4 and T6 conditions. The as-cast microstructure have coarse α-Mg and brittle β phase. The β particles got partially dissolute after solution treatment (T4) and further precipitates on aging at 167^{o}C (T6). The effect of as-cast microstructure, solutionizing and aging on the tensile properties and fracture toughness were quite clear from the obtained results. However, it is interesting to study the toughening mechanism that the crack tip undergoes as the material condition changes from as-cast to T4 and then T6 conditions. During, fatigue crack growth, Nicoletto et al. [225] observed crack bridging in AZ91 Mg alloy. Ritchie [226] explained crack bridging is one of the extrinsic toughening mechanism during fatigue crack growth propagation in ductile and brittle solids.

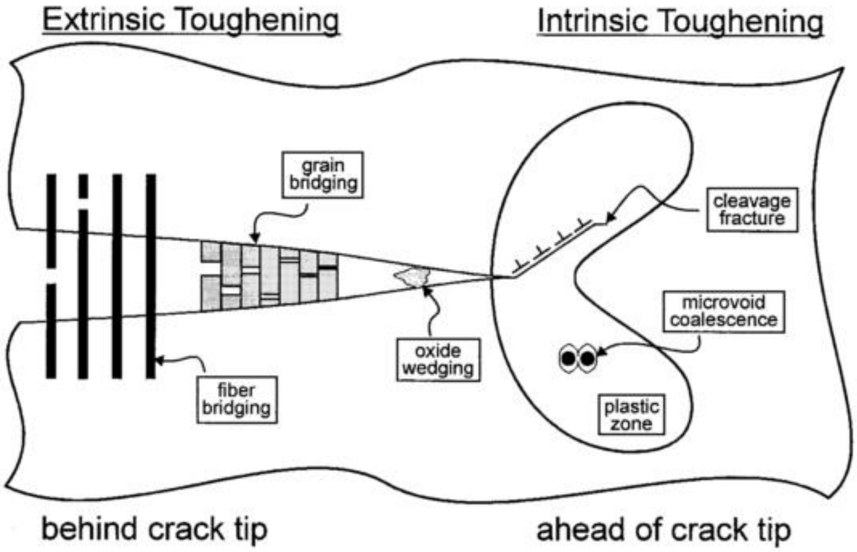

Fig. 4.9: Schematic illustration of extrinsic and intrinsic damage/toughening mechanism [227].

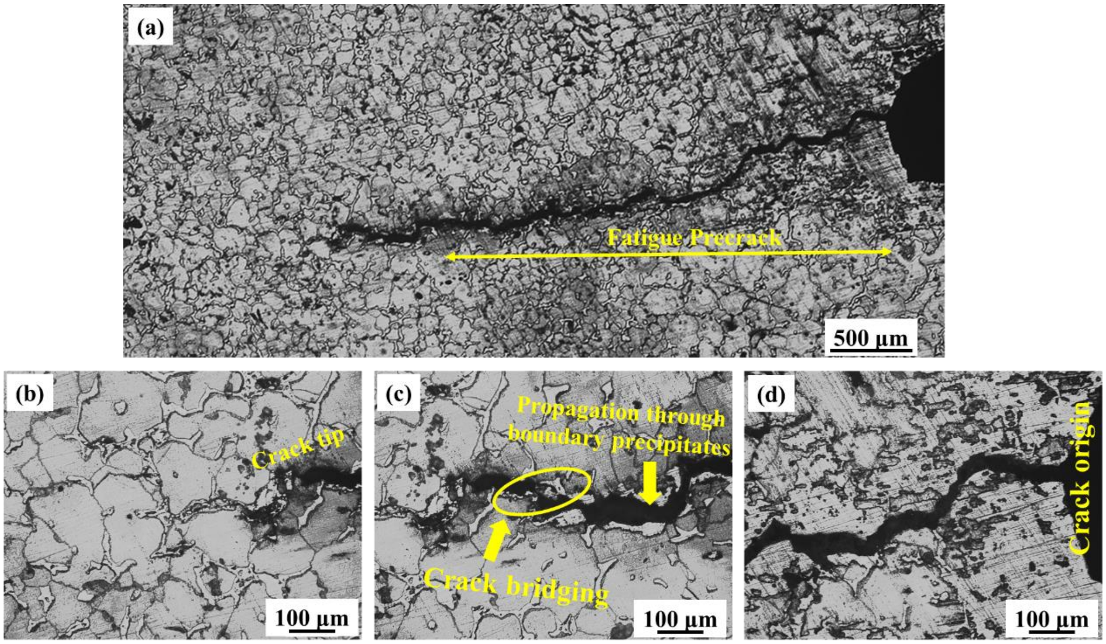

Fig. 4.10: T4 condition; (a) Crack path after J-integral test, (b) crack-tip, (c) fatigue pre-crack propagation through brittle dendrites and crack bridging by precipitates and (d) crack origin.

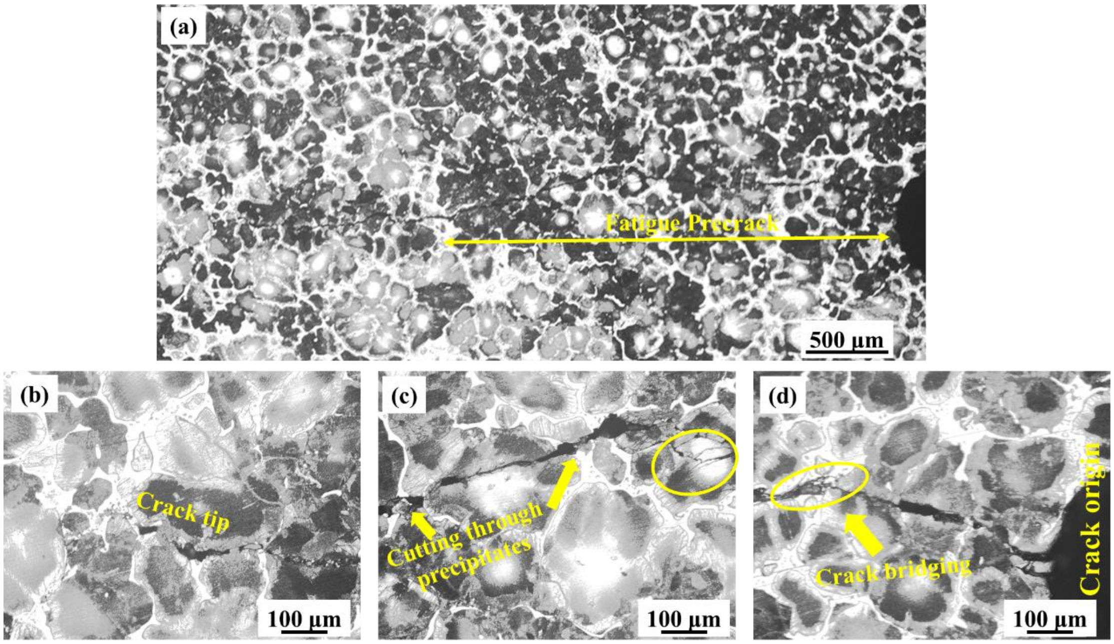

Fig. 4.11: T6 condition; (a) Crack path after J-integral test, (b) crack-tip, (c) fatigue pre-crack propagation cutting the brittle dendrites and crack bridging by precipitates and (d) crack origin.

Crack growth ahead of the crack tip is supported by intrinsic microstructural damage mechanisms, and impeded by extrinsic mechanisms acting primarily behind the crack tip which resists the effect of far-field driving forces on the crack tip. Intrinsic damage mechanisms in metallic materials are due to formation of microcrack, voids, dislocation pile-ups and interface decohesion in front of the rack-tip. On the other hand, extrinsic mechanisms are take place at the crack wake or behind the crack tip. The crack surfaces form inelastic zones while contacting with inclusions or second phase particles via sliding, bridging, wedging or by their combinations. The schematic of intrinsic and extrinsic mechanisms are shown in the Fig. 4.9.

In this work also, indication of crack bridging was observed along the crack surfaces behind crack-tip however, intrinsic damage mechanism in front of the crack tip dominate the fracture behavior. The crack tip along with fatigue pre-crack of T4 and T6 condition are shown in the Fig. 4.10(a) and Fig, 4.11(a) respectively. Regener and Dietze [228] observed that the fracture was due to the failure of interface between α-matrix and β-particles and the cleavage of β particles which are all intrinsic damage mechanisms. In Fig. 4.10 (b), the crack tip is observed to follow a tortuous crack path of the boundary precipitates which leads to intergranular crack growth whereas in T6 condition the crack growth was transgranular (Fig. 4.11(b)) while both the crack shows indication of crack bridging in fatigue pre-crack regime. Even the cracks are observed to originate from the α/β interface (Fig. 4.10(c) and (Fig. 4.11(c)). Hence, the extrinsic toughening mechanism seems common in all conditions but it is the intrinsic damage mechanism at the crack front which controls the fracture resistance mechanism in AZ91 Mg alloy. As segregation of α/β interface is quiet easier in as-cast condition when compared to T4 and T6 conditions, the fracture toughness was low in as-cast alloy.

4.3 Conclusions

The mechanical behavior of received AZ91 Mg alloy in as-cast, T4 and T6 conditions were studied by uniaxial tensile test and mode 1 fracture toughness test. The following conclusions were obtained

- The microstructure of as-cast material have brittle β phase , which got dissolute in α-Mg after T4 solution treatment and re precipitates during aging (T6).
- The alloy under solution treated condition (T4) exhibited better tensile strength and fracture toughness due to the dissolution of brittle β particles when compared to the as-cast material.
- Extrinsic toughening mechanism, crack bridging, was observed at the crack wake but it is the intrinsic damage mechanism, i.e., segregation of α/β interface at the crack tip, which defines the crack resistance behavior.

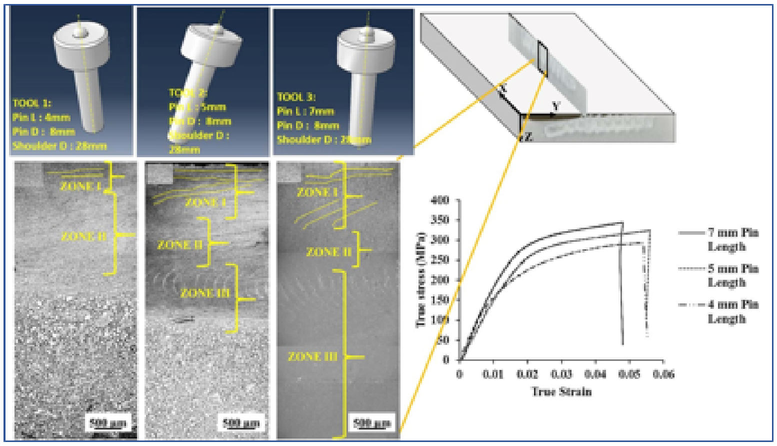

CHAPTER 5

EFFECT OF TOOL PIN LENGTH ON FSPED MICROSTRUCTURE

OVERVIEW

As subsequent chapters of the thesis are based on layered microstructure (microstructure variation through the thickness) created by tools with different pin length, it is important to analyze effect of the tool pin length on microstructure and mechanical properties.

CHAPTER 5

EFFECT OF TOOL PIN LENGTH ON FSPED MICROSTRUCTURE

Multipass FSP was performed using tools with different pin lengths. Its effect on microstructure and mechanical properties are presented in this chapter. Three tools with pin lengths of 4 mm (PL_4), 5 mm (PL_5) and 7 mm (PL_7) were used to process the AZ91 Mg plate, while other dimensions of the tool remained same. The microstructure exhibited inhomogeneity, inherent to the process, however its effect on mechanical properties and texture were found to be inconsequential. Further, the microstructural changes, namely, grain size, second phase particles distribution, texture and grain boundary misorientation distribution after FSP are presented in this Chapter.

5.1. Results

5.1.1 Material flow under the tool

The cast AZ91 Mg plates, 10 mm thick and 110 mm long, were subjected to multipass FSP with 50 % overlap along the retreating side using three different tools. The schematic of the macrostructural patterns on the transverse direction and along the process direction after FSP shown in the Fig. 5.1.

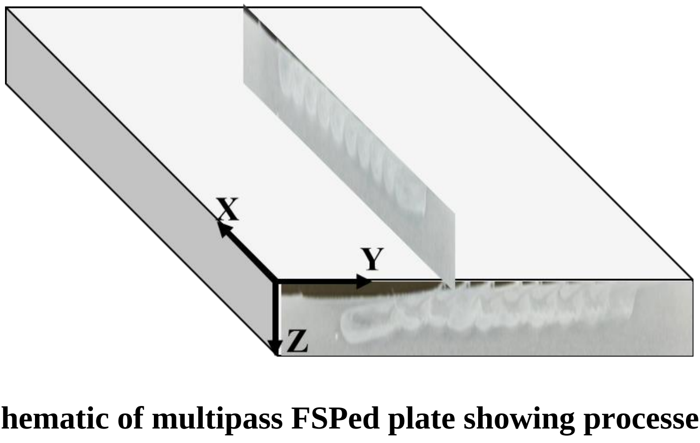

Fig. 5.1: Schematic of multipass FSPed plate showing processed region along the transverse direction (Y-direction) and along the process direction (X-direction).

The difference in the macrostructural features obtained using the tools PL_4, PL_5 and PL_7 are discussed with reference to the microstructures obtained from XZ plane.

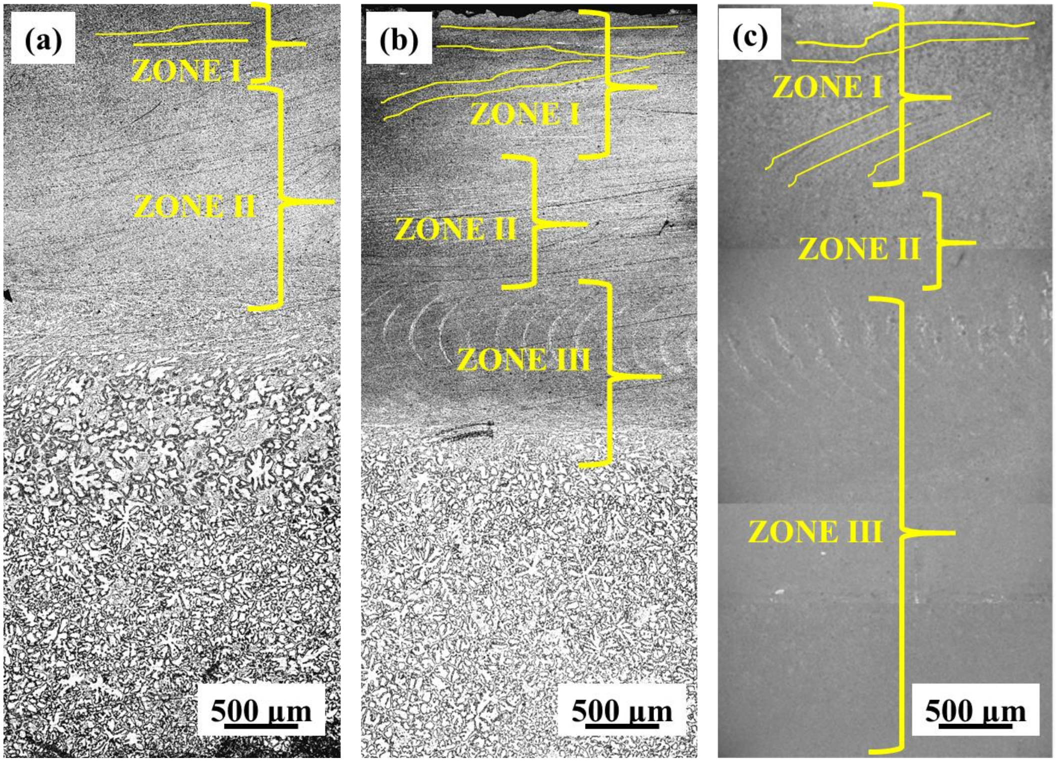

Fig. 5.2: Stitched optical images showing inhomogeneity in the microstructure in XZ plane of FSPed region processed by using; (a) PL_4, (b) PL_5 and (c) PL_7.

The stitched optical microstructures of FSPed plates in XZ plane processed by all the three tools are shown in the Fig. 5.2. The length of the processed region tally with the pin length used however, processed region can be divided in different zones on the basis of flow patterns observed in the macrostructure after FSP. Based on macrostructural features obtained after processing by PL_4 (Fig. 5.2(a)), the processed region can be divided in to two zones, namely, ZONE I and ZONE II. On the other hand, processed region after FSP by PL_5 (Fig. 5.2(b)) and PL_7 (Fig.5.2(c)) was divided into three zones i.e. ZONE I, ZONE II and ZONE III. In ZONE I the flow lines are almost parallel to the surface. It appears that macrostructure of ZONE1 was primarily affected by the rotating shoulder. In ZONE II material flow is expected to be vigorous [229] due to combined effect of pin and shoulder which resulted in fine microstructure without any macro features. The downward flow from the shoulder was closely balanced by the upward flow in this region. In ZONE III the material flow was affected only by the pin and, since temperature is expected to be lower away from the shoulder [230], the macrograph contain semicircular ring patterns in this region.

5.1.2 Microstructure

The microstructures before and after FSP were compared in Fig. 5.3. As-cast microstructure, shown in Fig. 5.3(a), contain dendrites of 100 μm average size and interdendrites with average thickness of 20 μm. The secondary electron image of as-cast microstructure is shown as insert in Fig. 5.3(a). EDS analysis presented in Table 5.1 in conjunction with Fig. 5.3(a) brings out that dendrites (A) had elemental composition of 5.1 wt.% Al whereas, interdendrites (B) had 34.4 wt. % Al and 2.4 wt. % Zn. This confirms that α – Mg matrix is deficient in Al and, interdendrites consist of β precipitates ($Mg_{17}Al_{12}$).

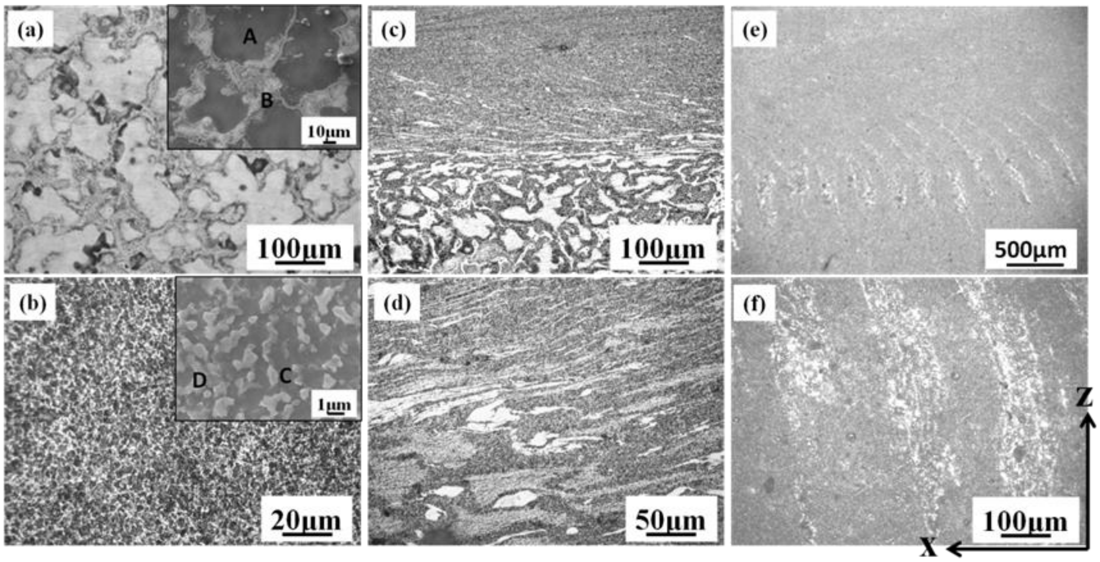

Fig. 5.3: Four distinct microstructure regions observed from macrostructures along the transverse plane a) as cast microstructure, b) FSPed fine grained microstructure; c) microstructure of transition region; d) transition region in higher magnification; e) inhomogeneous microstructured region and f) magnified microstructural inhomogeneities.

FSPed region with fine grain microstructure and broken, homogeneously distributed precipitates are seen in Fig. 5.3(b). In the inset of Fig. 5.3(b), the SEM image of the FSPed region exhibit two features (C and D) which were identified as matrix and precipitates. The matrix (C) contain 10.28 wt.% Al whereas precipitate (D) contain 22.59 wt. % Al. It is clear that partial precipitate dissolution occurred during FSP. The transition region in Fig. 5.3(c) and its magnified image in Fig. 5.3(d) exhibit elongated grains. Fig. 5.3(e) and its magnified image in Fig. 5.3(f) exhibit non-uniformity in grain size in the form of periodic ring patterns which was observed after FSP using longer pin length. It is clear that FSP has resulted in breaking of dendritic structure accompanied by refinement and uniform distribution of precipitates accompanied by partial precipitate dissolution. The XRD pattern in Fig.5.4 supports EDS data, ensuring the existence of α-Mg and β-$Mg_{17}Al_{12}$ phases in both as-cast and FSPed AZ91 samples. Intensity attenuation and disappearance of certain diffraction peaks of β-phase confirms dissolution of β - phase and enrichment of magnesium matrix after FSP.

Table 5.1: Elemental distribution obtained using EDS, at different regions marked in Fig. 5.3.

Region	Mg		Al		Zn	
	Wt. %	**at. %**	**Wt. %**	**at. %**	**Wt. %**	**at. %**
A	94.8	95.3	5.1	4.6	-	-
B	63.1	66.4	34.4	32.6	2.4	0.9
C	89.7	90.6	10.2	9.3	-	-
D	77.5	79.2	22.5	20.7	-	-

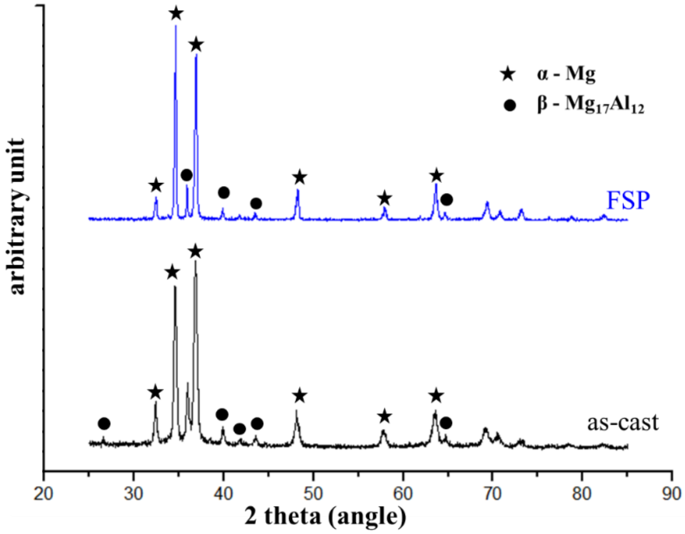

Fig. 5.4: Phase identification in as-cast and FSPed material by XRD peaks. Disappearance of certain peaks indiciate dissolution of second phase in to the matrix.

5.1.3 Microtexture

The grain structure after FSP was not apparent in optical and secondary electron images but it is quite clear in the inverse pole figure (IPF) map (Fig. 5.5(a)) acquired from EBSD scan. In order to obtain a statistically valid EBSD data, a large area scan was performed to find average grain size, texture and misorientation distribution. The IPF map shown in the Fig. 5.5(a) was obtained from the XZ plane but the textures were rotated towards normal direction (Z-direction) so that it can be compared with the macrotextures and textures obtained after deformation (presented in Chapter 7 of the thesis). The average grain size is 0.8 µm and the grains are having predominantly basal orientation. The (0001) and $(10\bar{1}0)$ pole figures are shown in Fig. 5.5(b). The basal plane normal is tilted towards process direction in the normal plane. Similar basal texture alignment in the process direction was observed in AZ31 [231] and AZ91 magnesium alloys [174]. Besides basal texture the microstructure contain 20% of misorientation angle around 30° as shown in the Fig. 5.5(c) which is in agreement with the work by Feng and Ma [232] on as-cast AZ80 Mg alloy after FSP. The higher fraction of 30° misorientation between grains with basal orientation is due to higher geometrical probability in hexad symmetry for this misorientation [233].

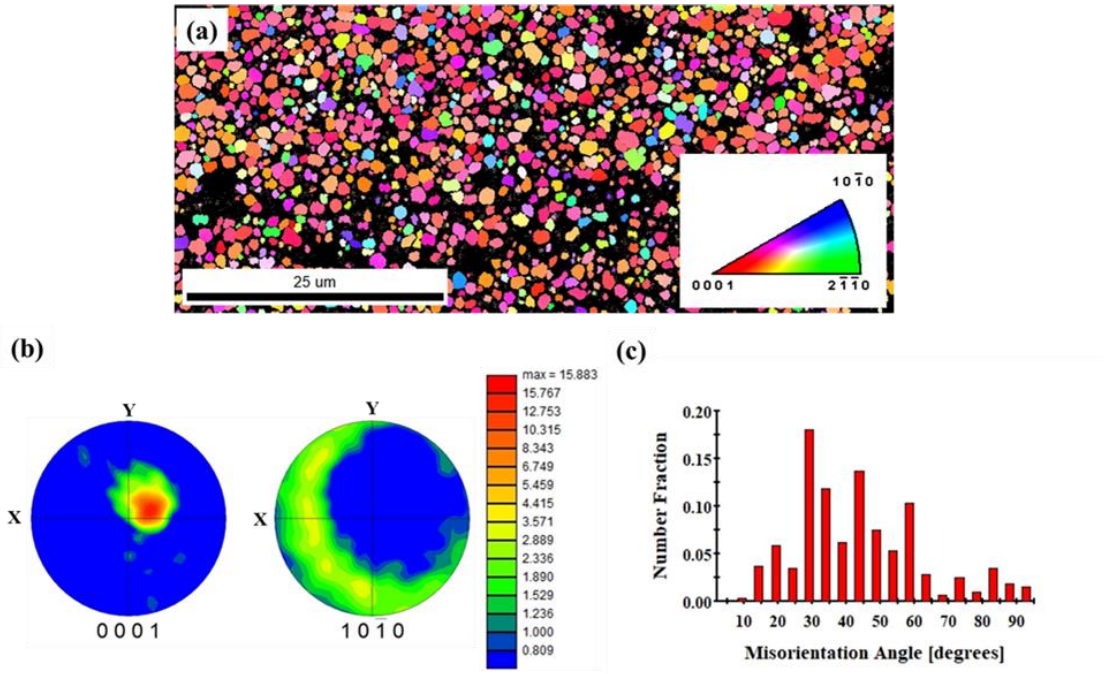

Fig.5.5: EBSD analysis of FSPed region of sample processed by tool3; (a) Inverse pole figure map, (b) (0001) and $(10\bar{1}0)$ pole figures and (c) grain boundary misorientation distribution.

5.1.4 Phase distribution

The macrostructures provided obvious differences in the structure after FSP using three tools with different pin lengths. To understand the processed microstructures further, SEM images of FSPed regions obtained after processing by the three tools are shown in the Fig. 5.6. The microstructures exhibit similar distribution of phases in all the three samples, i.e., samples processed by PL_4 (Fig. 5.6(a)), PL_5 (Fig. 5.6(b)) and PL_7 (Fig. 5.6(c)). There was no significant deviation in the elemental distribution between phases after FSP by the three tools. Approximately, the elemental distribution in α-phase (Mg~90 wt. % and Al~10 wt. %) and in β-phase (Mg~80 %, Al~20 %) are quite similar in all the cases.

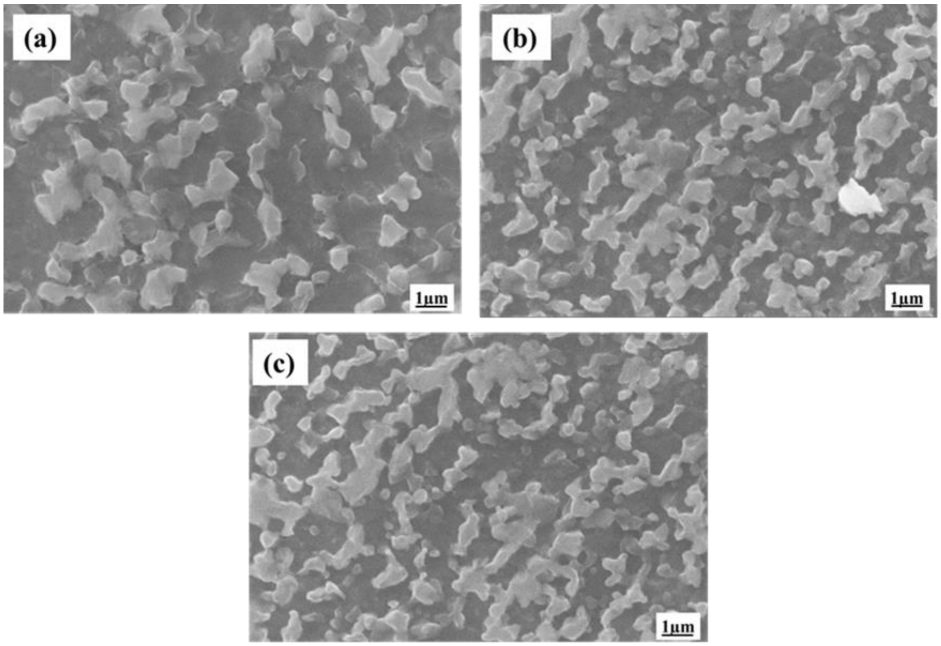

Fig. 5.6*:* SEM image of the samples FSPed by the tools; (a) PL_4, (b) PL_5 and (c) PL_7.

In order to understand the change in nature of precipitates formed after FSP using different pin lengths, phase analysis by XRD was carried out and presented in Fig. 5.7. The α-peaks and β-peaks are at same position in all the samples FSPed by using the three tools PL_4, PL_5 and PL_7, indicates the similarity in the phases obtained.

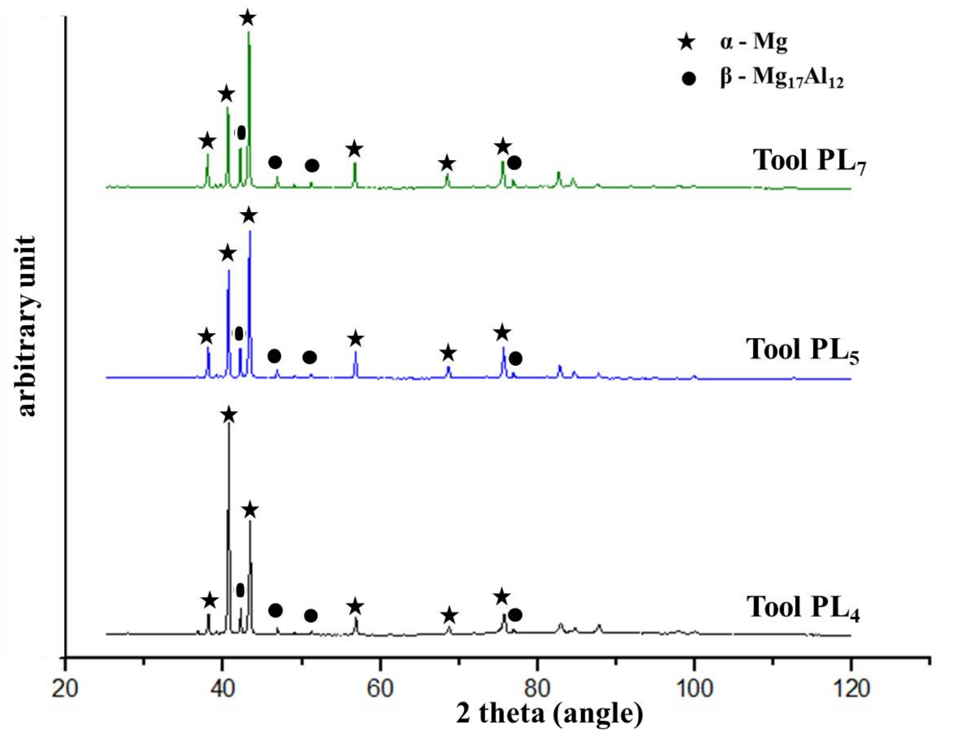

Fig. 5.7: Phase analysis by XRD peaks obtained in FSPed regions of samples processed by the tools PL_4, PL_5 and PL_7.

5.1.5 Tensile properties

Apart from microstructure it is necessary to study influence of tool pin length, which is a main process variable in this work, on the mechanical properties. The tensile test results are shown in Fig. 5.8. Tensile strength and elongation of material processed by tool PL_4 is 290 MPa and 5.4 % respectively. In the material processed by tool PL_5, the tensile strength increased to 320 MPa whereas the elongation remains approximately same at 5.5 %. Further, the strength increased to 340 MPa in the material processed by tool PL_7 but the elongation reduced to 5 %. Although, strength found to increase with increase in thickness of the FSPed material, the variation is only 15% for increase in thickness by 100%. The ductility in all the cases was approximately 5 %. Hence, it is clear that properties of fine grained material are more or less same irrespective of pin length used to get grain refinement.

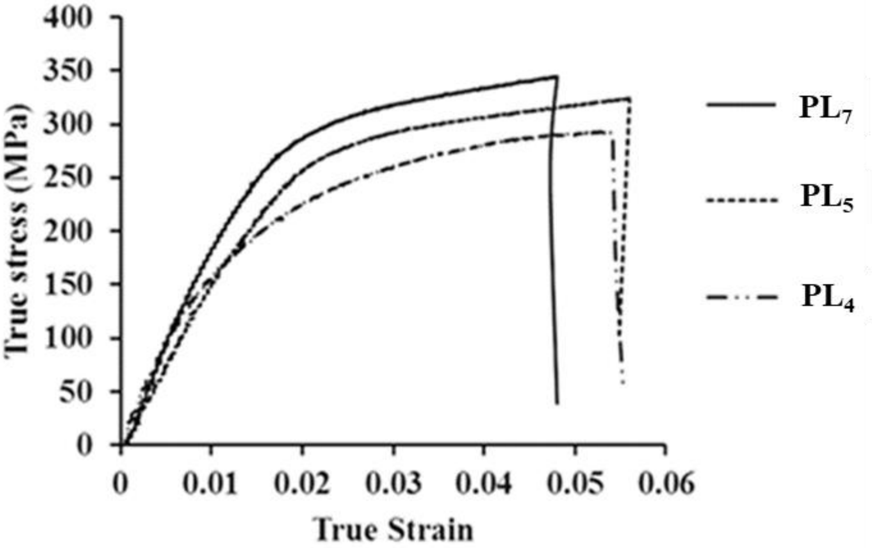

Fig. 5.8: True stress vs. True strain curve of FSPed region samples obtained from tools with different pin lengths.

Previous studies on FSP of Al alloys also did not show any significant deviation in the mechanical properties due to the microstructural variation that exist after FSP in thickness direction as well as in the multipass direction i.e. between two passes [234–237].

5.2 Discussion

5.2.1 Semi-circular ring patterns

Semicircular ring patterns observed in the Fig. 5.2(b) & (c) have equal spacing between two successive rings. The spacing between two successive rings was found to be approximately 200 μm. Interestingly the distance between two rings was approximately equal to the pitch (traverse speed/rotational speed=208 μm) of the FSP process. It is also worth noting that the tool pin length was more than 5mm in case of PL_5 and PL_7 whereas, in tool PL_4 it was less than 5 mm. Hence, the FSPed region obtained by PL_4 has effect of only shoulder and the combined effect shoulder and pin but it doesn't contains the region due to the effect of only pin. In tool2 and tool3 the circular ring patterns observed were due to the effect of only pin. Moreover, Swaminathan et al. [238] studied peak temperature during FSP of NiAl bronze alloy and reported that temperature at depths below 4mm from the shoulder will be 50–100 °C lower than that at the surface. Therefore, it appears that the non-uniform microstructure is due to improper mixing of the material during FSP well below the shoulder. Ma et al. [151] observed similar β-phase particles rich bands during FSP of cast AZ91 and AZ80 magnesium alloys which was attributed to the lower strain rate/strain and temperature conditions which in turn depends on tool rotational and traverse speeds.

5.2.2 FSPed microstructure

The multipass FSPed AZ91 alloy is characterized by very fine matrix grains (~0.8 μm) and β-particles distributed uniformly in the microstructure with some non-uniformity in the microstructure. In the location where uniform microstructure was observed, the eutectic β-$Mg_{17}Al_{12}$ network in the as-cast AZ91 alloy disappeared after multipass FSP due to mechanical shearing and dissolution by frictional heat. Based on the Mg–Al phase diagram and the differential scanning calorimetry (DSC) analysis by Feng and Ma [152], the heating temperature of 437°C causes the dissolution of the eutectic β-$Mg_{17}Al_{12}$ phase into the magnesium matrix in AZ91 alloy. The EDS analysis indicated that FSPed region had 10.28 wt. % Al, i.e. approximately equal to the aluminum concentration in AZ91alloy. This value is much higher than that (5.16 wt. % Al) in the as cast alloy, indicating significant dissolution of the eutectic β-$Mg_{17}Al_{12}$ phase into magnesium matrix during FSP. Celotto and Bastow [30] had reported that the maximum solid solubility of aluminum in magnesium was as high as 12.9 wt. % at the eutectic temperature and about 1.5 wt. % at room temperature. It implies that matrix grains of FSPed AZ91 alloy were in supersaturated solid solution condition. The XRD pattern in Fig. 5.4 supports EDS data, ensuring the existence of α-Mg and β-$Mg_{17}Al_{12}$ phases in both as-cast and FSPed AZ91 samples. Intensity attenuation and disappearance of certain diffraction peaks of β-phase confirms dissolution of β-phase and enrichment of magnesium matrix after FSP. Hence, it is clear that FSP has resulted in breaking of dendritic microstructure accompanied by refinement and uniform distribution of alloying elements.

5.2.3 Deformation mechanism and texture

EBSD analysis of multipass FSPed sample was carried out to understand the nature of deformation mechanism that cause the resultant microstructure and texture produced after friction stir processing. The EBSD map was obtained from plane perpendicular to transverse direction (XZ plane) of the material processed by tool PL_5. Fig. 5.9(a) shows grain size map. It shows that grain size varies from less than 1 μm to 5 μm with most of the grains showing lower than 1 μm size. Fig. 5.9(b) shows grain orientation spread (GOS) map. GOS value indicates amount of substructure in the microstructure. High GOS value represents sub-grains and high dislocation density. On the other hand GOS < 1 indicates recrystallized grains. The fine grain size together with GOS value lesser than one indicates occurrence of dynamic recrystallization during the process. Thus, dynamic recrystallization (DRX) was the deformation mechanism that generated fine grained microstructure during FSP.

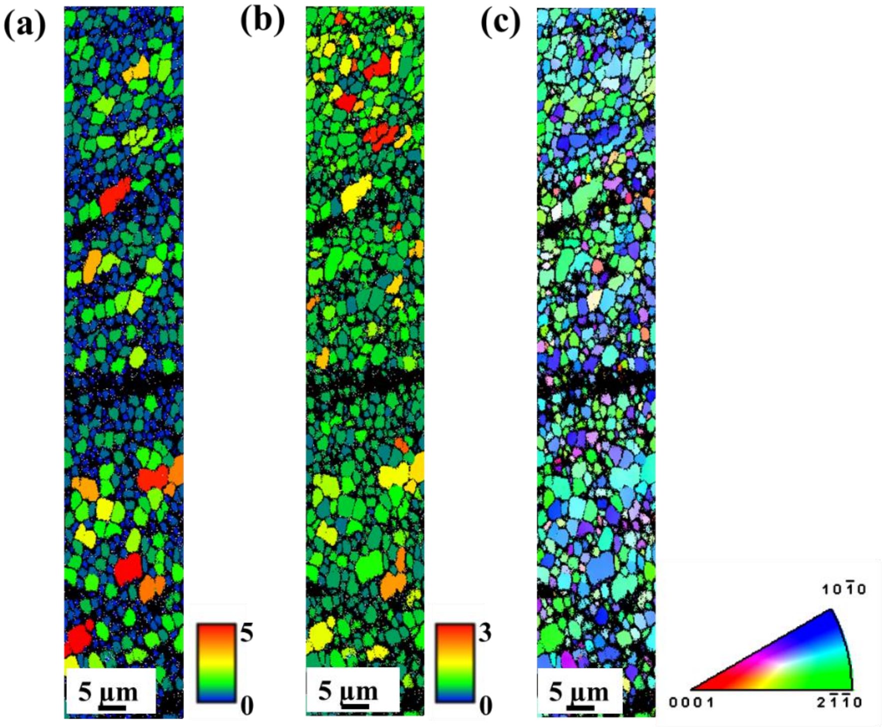

Fig. 5.9: (a) Grain size map, (b) GOS map, (c) IPF map obtained at processed region from transverse plane sample processed by PL$_5$.

The IPF map in Fig. 5.9(c) depicts non-basal slip in the transverse plane (XZ plane) which implies the normal plane contain basal texture which is ensured by the dominant basal poles in Fig. 5.7(c). The critical resolved shear stress (CRSS) for non-basal slip systems is predicted to be approximately 5 times higher than basal slip systems [239]. Therefore, in process direction basal slip dominates the deformation, whereas in the transverse direction, non-basal slip dominates the deformation. Jain et al. [173] in their work reported yield anisotropy with better mechanical properties in transverse direction when compared to process direction in FSPed AZ91 alloy due to such strong basal texture in process direction. Hence, in further part of the work, all the mechanical tests were carried out in the process direction as a safe design criterion.

5.3. Conclusions

To generate layered microstructure (subsequent chapters) in AZ91 Mg alloy, it was necessary to use tools with different pin lengths. Hence, the effect of tool pin length on the FSPed microstructure and its influence on mechanical properties were analyzed and following conclusions were obtained,

- An apparent difference and necessary condition of change in depth of the processed region was achieved.
- Semi-circular ring patterns was observed in the tools with pin length 5 mm (PL_5) and 7 mm (PL_7) due to only pin effect which was nullified in the FSPed region obtained using the tool with pin length 4 mm (PL_4).
- Though there were differences in the macrostructure of the processed regions using three tools, the difference in microstructural aspects, i.e., phase distribution, microstructure, microtexture and its influence on mechanical properties are inconsequential.
- The microstructure of the processed region contained grains with average size of 0.8 μm and predominant basal texture slightly tilted towards process direction in the normal plane (XY plane).

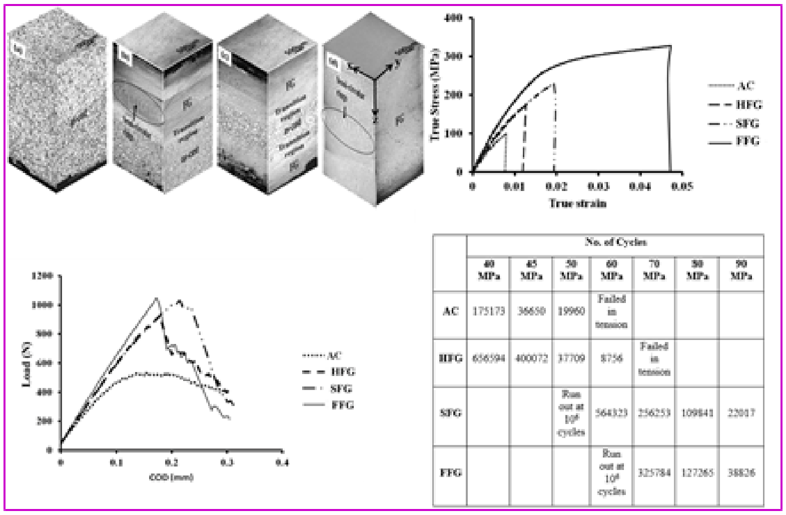

	No. of Cycles						
	40 MPa	45 MPa	50 MPa	60 MPa	70 MPa	80 MPa	90 MPa
AC	175173	36650	19960	Failed in tension			
HFG	656594	400072	37709	8756	Failed in tension		
SFG			Run out at 10^6 cycles	564323	256253	109841	22017
FFG				Run out at 10^6 cycles	325784	127265	38826

CHAPTER 6

LAYERED MICROSTRUCTURE AND ROOM TEMPERATURE PROPERTIES

OVERVIEW

The layered microstructures, containing mixture of as-cast microstructure and fine grained microstructure through the thickness, were generated by multipass FSP. The effect of this layered microstructure on the room temperature mechanical properties; tensile, fracture and fatigue, were studied.

CHAPTER 6

LAYERED MICROSTRUCTURE AND ROOM TEMPERATURE PROPERTIES

After studying the effect of tool pin length on the microstructure and mechanical properties of multipass friction stir processed AZ91 Mg alloy, layered microstructures were generated. The microstructure consists of layer of processed (fine grained) and unprocessed (as-cast) region. Three such layered microstructure were generated, first being half thickness processed and remaining half of the thickness is unprocessed (HFG), second one was processed one third from both the surfaces and the middle one third is unprocessed (SFG) and the final one consists of full thickness processed region (FFG). The room temperature mechanical behavior of these layered microstructured materials were studied by testing them under uniaxial tensile loading, monotonic loading in presence of a notch and cyclic loading.

6.1. Results

6.1.1 Microstructure

Macrostructure of all the four configurations i.e. AC, HFG, SFG and FFG are shown in a three dimensional montage in Fig.6.1. The AC material shows homogeneous, coarse grained, as cast microstructure throughout the thickness, as shown in Fig. 6.1(a). Material processed to half the thickness (HFG) contain 3 mm as-cast, coarse grained microstructure from one surface and 3 mm FSPed microstructure from the other surface, as shown in Fig. 6.1(b). Material processed from both the surfaces (SFG) as shown in Fig. 6.1(c) contain 2 mm of processed microstructure from both the surfaces and the middle 2 mm has as-cast, coarse grained microstructure. Fig. 6.1(d) shows full thickness processed material (FFG) having processed microstructure throughout the 6 mm thickness. Macrostructures in Fig. 6.1(b) and Fig. 6.1(d) exhibit non-uniform microstructure having semi-circular rings. This particular feature is visible for the processing conditions in which tool with longer pin was used.

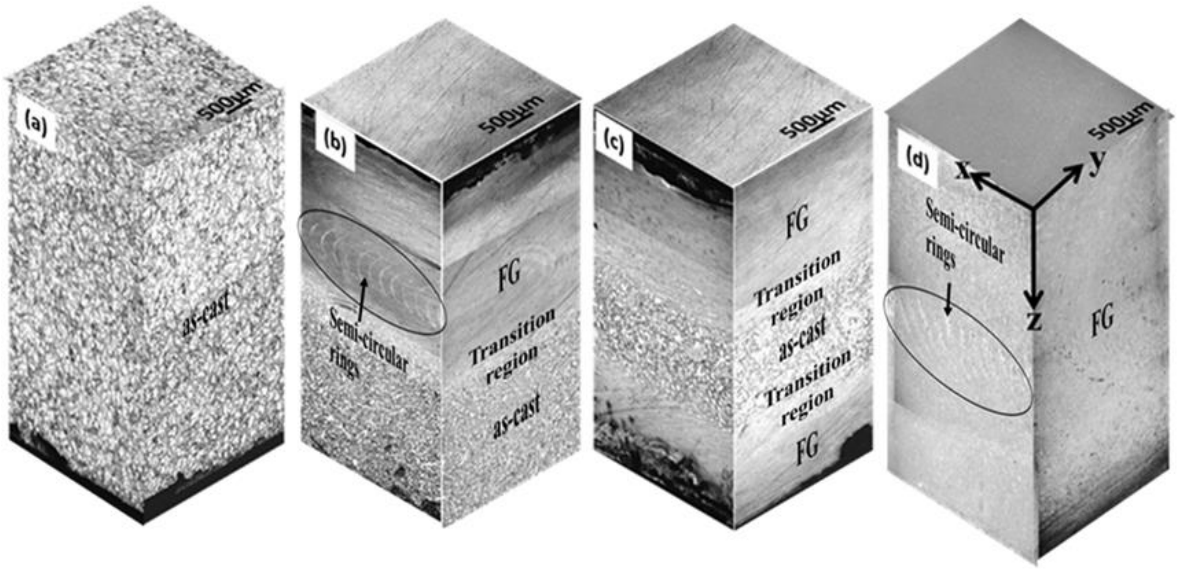

Fig. 6.1: Macrostructure of (a) AC, (b) HFG, (c) SFG and (d) FFG samples. As-cast microstructure regions, fine grained regions (FG), transition regions and semi-circular ring patterns are mentioned. Arrows x, y and z represent process direction, transverse direction and thickness direction respectively.

6.1.2. Tensile properties

The true stress versus true strain curves of specimens with different microstructural regions are presented in Fig. 6.2. The as-cast (AC) microstructure exhibited low strength and elongation whereas, FFG sample showed highest strength and elongation.

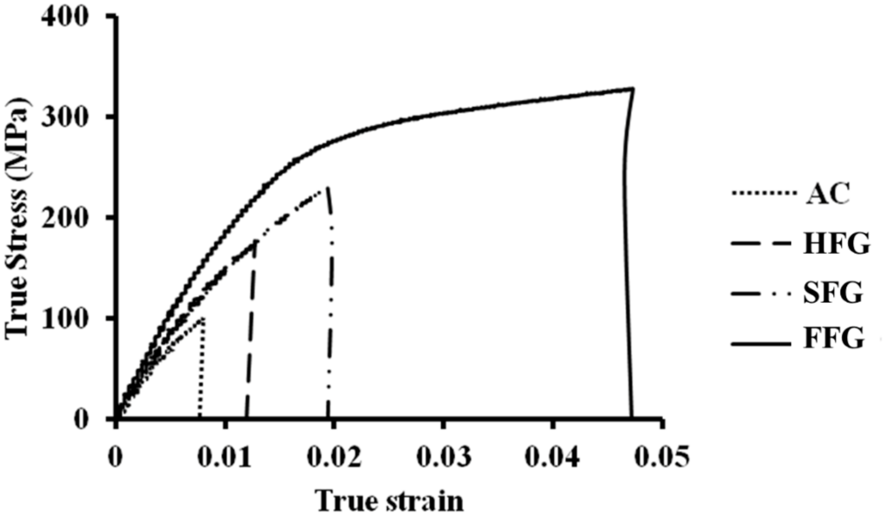

Fig. 6.2: True stress versus True strain curve of samples with different microstructural configurations.

On comparing FFG sample with AC, the yield strength (YS) increases from 92.MPa to 242.MPa, ultimate tensile strength (UTS) from 100 MPa to 328 MPa and ductility from 0.8 % to 4.7%. The YS, UTS and ductility of HFG were 158 MPa, 175 MPa and 1.3 % respectively. Although, surface modified microstructure (SFG) showed yield strength (203 MPa) and tensile strength (230 MPa) comparable to FFG, improvement in elongation was insignificant as work hardening region was observed only in the FFG specimen. The HFG and SFG were showing intermediate properties between AC and FFG samples. Gradual improvement in the yield and tensile strength was observed with the increase in the amount of the processed material, in the following order; AC, HFG, SFG and FFG.

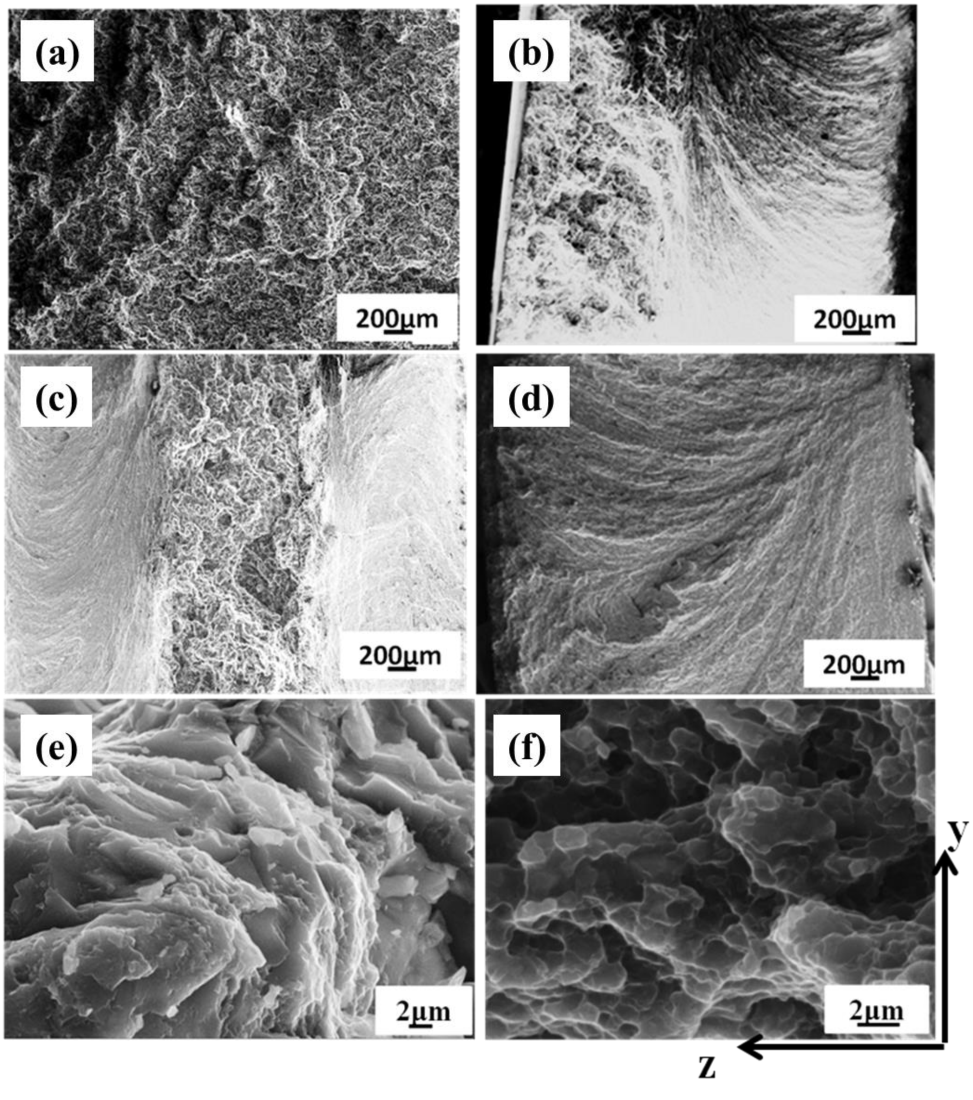

Fig. 6.3: Fractographs of uniaxial tensile tested samples with the fracture surfaces in process plane; (a) AC, (b) HFG, (c) SFG, (d) FFG (e) transcrystalline fracture in as cast region and (f) intergranular fracture in FSPed regions.

Fig. 6.3 shows the fractographs of tensile samples with fracture surfaces perpendicular to processing direction (and tensile direction). Typical features of transcrystalline, brittle, cleavage fracture were observed in the as-cast (AC) sample (Fig. 6.3(a)). The fracture surface in HFG sample exhibited two distinct regions in two halves as shown in the Fig. 6.3(b). One half was as-cast region characterized by cleavage surface and another half was processed region characterized by intergranular fracture. Fracture surface contain flow lines very similar to the one observed in the microstructure after FSP. Similarly SFG also had two distinct regions in three parts as shown in Fig. 6.3(c). Material up to 2 mm depth from the surface has intergranular fracture and the middle region it has characteristic transcrystalline cleavage fracture of cast structure. The FFG sample has intergranular fracture morphology as shown in the Fig. 6.3(d). Thus, the fractured surfaces clearly differentiate the processed and unprocessed region with intergranular fracture and transgranular fracture respectively. The magnified images of transgranular fracture and intergranular fracture were shown in the Fig. 6.3(e) and Fig. 6.3(f) respectively.

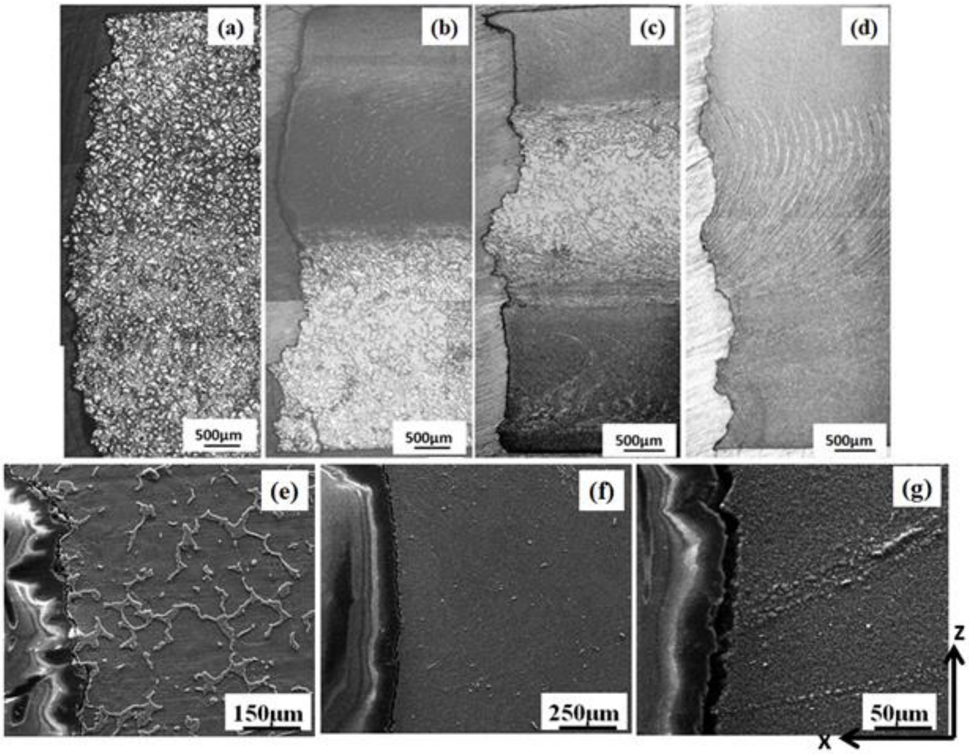

Fig. 6.4: Optical images of tensile sub-surfaces of (a) AC, (b) HFG, (c) SFG and (d) FFG along the transverse plane which is parallel to the loading axis and FE-SEM images of fracture profile of (e) as-cast region, (f) FSPed region without inhomogeneities and (g) FSPed region with inhomogeneities.

To bring out the effect of microstructural variation on fracture behavior, fracture profile in through thickness were obtained using optical microscopy, as shown in Fig. 6.4. The analysis was carried out to understand crack propagation path. AC sample in Fig. 6.4(a) shows zigzag fracture path whereas, the processed region of HFG in Fig. 6.4(b) and SFG in (Fig. 6.4(c)) has smooth and curved profile. Fig. 6.4(d) shows irregular fracture profile of FFG material. The zigzag fracture profile of AC material is due to crack propagated along interdendritic particle, as shown in scanning electron image in Fig. 6.4(e). The high magnification SEM image of HFG and SFG in Fig. 6.4(f) reveal that the smooth fracture profile was due to microstructural refinement. However, irregular fracture profile observed in FFG is due to non-uniform microstructure at semi-circular ring patterns as shown in Fig. 6.4(g).

6.1.3 Apparent notch fracture toughness

The apparent notch fracture toughness values (notch K_Q) of single edge notched bend (SENB) specimens, without pre crack, were also observed to follow a trend similar to the tensile test.

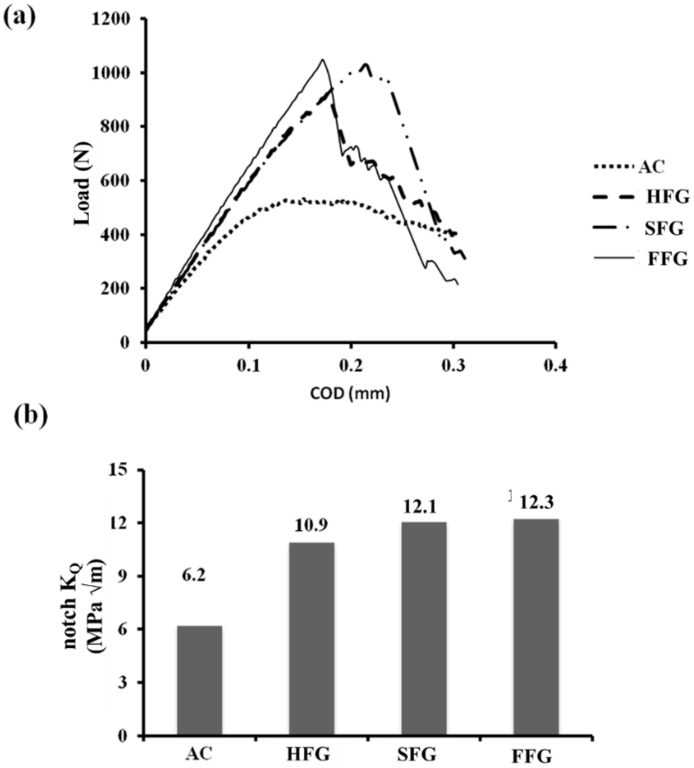

Fig.6.5: Notch fracture toughness test results of samples with different microstructural configurations (a) load vs. crack opening displacement (COD) curve and (b) comparison of apparent notch fracture toughness.

The plot of load against crack opening displacement (COD) is shown in Fig. 6.5(a). The AC sample did not show any sharp peak at maximum, whereas pop-in had occurred in the SFG sample. The HFG and FFG samples too exhibited sharp maximum load. Fig. 6.5(b) shows notch K_Q values of different samples which indicate improvement in fracture toughness from AC to FFG sample. The AC specimen showed lowest K_Q value of 6.2 MPa√m and FFG had highest K_Q value of 12.3 MPa√m with HFG and SFG showing K_Q values of 10.9 MPa√m and 12.1 MPa√m respectively. The values mentioned are apparent notch fracture toughness (K_Q). These values may not indicate the actual material property but are consistent enough to compare the fracture toughness with different processing conditions.

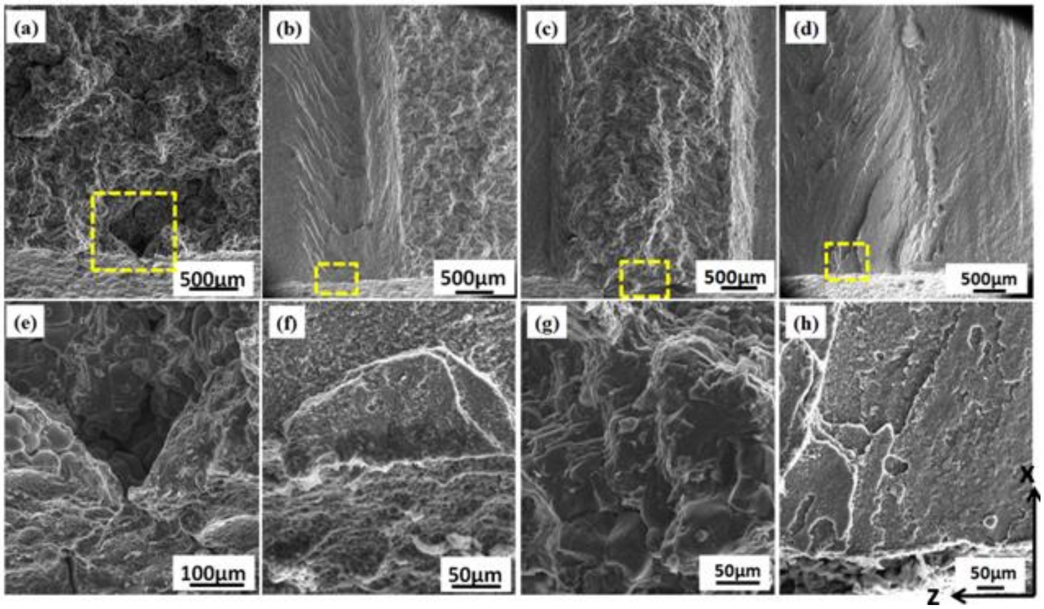

Fig. 6.6: Fractograph of SENB samples; (a) AC, (b) HFG, (c) SFG and (d) FFG with their crack origins marked inside the box and respective magnified images in (e)–(h).

The fractograph of fracture toughness tested samples are shown in Fig. 6.6. Similar to the fractograph of tensile samples, the fracture toughness samples too have clear distinction between processed and unprocessed regions. In as-cast (AC) sample there is a void formation at the center of the notch, marked as box in Fig. 6.6(a) which is identified as crack initiation site. Similarly in SFG sample, void formation was observed at the notch in as-cast region (Fig. 6.6(c)) though the void formation in SFG is not as prominent as in AC sample. Secondary cracks were observed on both processed and unprocessed region around the notch of HFG. The spot with secondary crack on processed region was considered as crack initiation site (Fig. 6.6(b)) as there is no indication of void formation in the as-cast region. The fractograph of FFG with the crack initiation site was shown in Fig. 6.6(d). The magnified images of crack initiation sites of AC, HFG, SFG and FFG are shown in Fig. 6.6(e)–(h) respectively.

6.1.4 Fatigue

To study the fatigue behavior of all four various microstructural compositions, high cycle fatigue experiments were performed at selected stress amplitudes based on the tensile strength of the specific microstructural composition instead of performing complete S-N curve. The UTS of as cast and HFG are 100 MPa and 175 MPa respectively. The stress amplitudes of 40 to 60 MPa were selected so that maximum load that can reach will be within the UTS. In similar manner stress amplitudes of 50 to 90 MPa were selected for both SFG and FFG materials. The results are shown in the Table 6.1. Fatigue life has been improved from as cast to FFG. However, very marginal improvement in the FFG material was observed in comparison to SFG samples at high stress amplitudes.

Table 6.1: Fatigue test results of samples with different microstructural composition showing No. of cycles to failure at different stress amplitudes.

	No. of Cycles to failure						
	40 MPa	**45 MPa**	**50 MPa**	**60 MPa**	**70 MPa**	**80 MPa**	**90 MPa**
AC	175173	36650	19960	Failed in tension			
HFG	656594	400072	37709	8756	Failed in tension		
SFG			Run out at 10^6 cycles	564323	256253	109841	22017
FFG				Run out at 10^6 cycles	325784	127265	38826

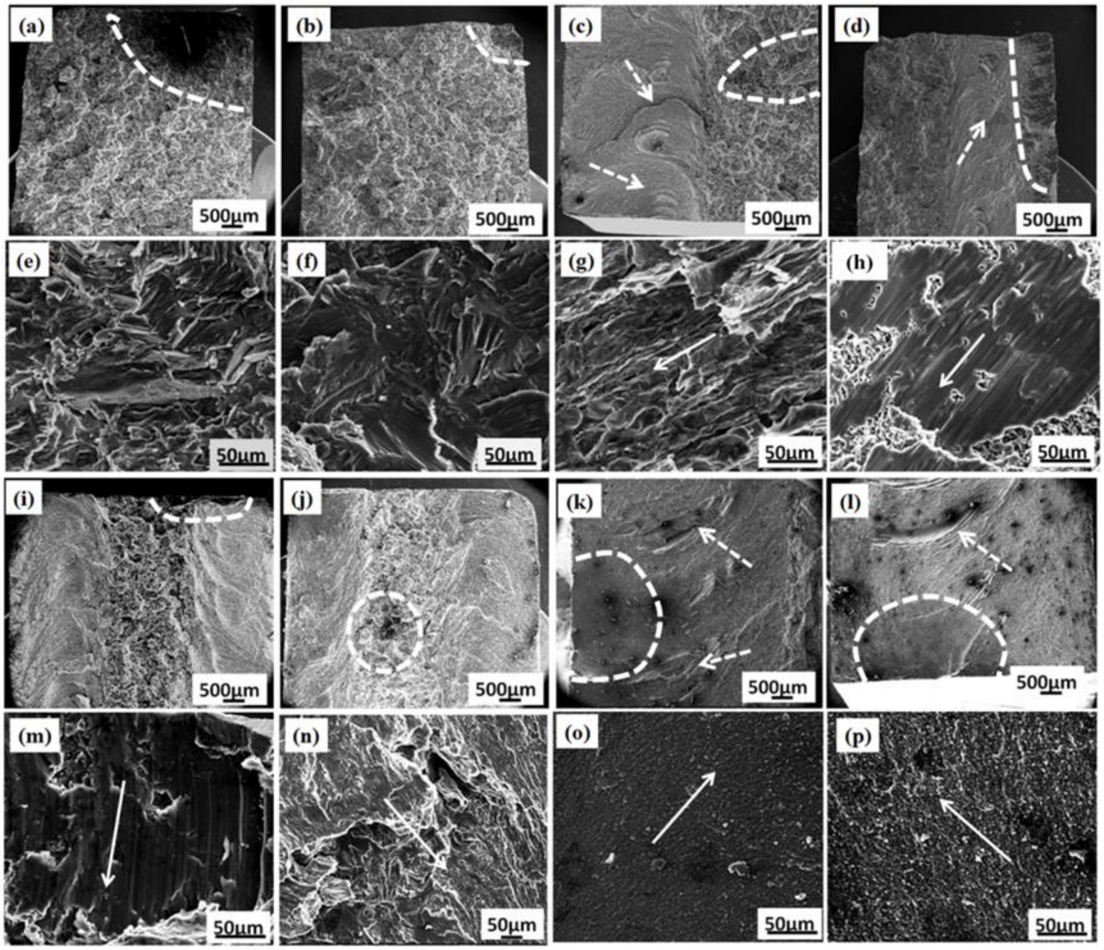

Fig. 6.7: Fractograph of fatigue tested samples at specific stress amplitudes (a) AC at 40 MPa, (b) AC at 45 MPa, (c) HFG at 40 MPa, and (d) HFG at 45 MPa with (e), (f), (g) and (h) are respective magnified fatigue crack growth regions marked in boxes, similarly (i) SFG at 70 MPA (j) SFG at 80 MPa, (k) FFG at 70 MPa and (l) FFG at 80 MPa while (m), (n), (o) and (p) are respective magnified fatigue growth regions. Dotted arrows indicate inhmogeneities and solid arrows indicate crack growth direction.

The fractograph of fatigue tested sample are shown in the Fig.6.7. The topology of fatigue crack sites was observed from the complete fractured surfaces. The as-cast, AC, samples has shown the stress concentrating corners as the fatigue crack initiation zone at both 40 MPa and 45 MPa stress amplitudes in Fig. 6.7(a) and Fig. 6.7(b)) respectively. In HFG the fatigue crack growth were observed on the as cast region at 40 MPa (Fig. 6.7(c)) and in processed region at 45 MPa (Fig. 6.7(d)). The magnified images of fatigue crack regions are presented exactly below the corresponding full thickness fractographs. In AC sample the fatigue crack growth regions have wider facets (Fig. 6.7(e) and Fig. 6.7(f)) when compared to the facet observed in as cast region of HFG at 40 MPa in Fig. 6.7(g). The fractograph of fatigue failures of SFG at stress amplitude 80 MPa and 90 MPa are shown in the Fig. 6.7(i) and Fig. 6.7(j) respectively and that of FFG are shown in Fig. 6.7(k) and Fig. 6.7(l) in the same manner. The corresponding magnified striated fatigue regions are presented exactly below the full thickness fractographs. Fig. 6.7(h) and Fig. 6.7(m) exemplify the fatigue growths in the fine grained region of HFG at stress amplitude 45 MPa and SFG at stress amplitude 80 MPa respectively. The facets in as cast region of SFG (Fig. 6.7(n)) tested at stress amplitude 90 MPa are smaller than that of HFG (Fig. 6.7(g)). The fatigued regions of FFG at stress amplitudes 80 MPa (Fig. 6.7(o)) and 90 MPa (Fig. 6.7(p)) are quite different from the other samples which are very fine. The directions of fatigue crack propagations are represented by solid arrow marks which are almost approximately 45 degrees to the loading axis and the broken arrow marks indicate the inhomogeneities.

6.2 Discussion

6.2.1 Rule of mixture

In the present work, different microstructural configuration and proportions namely, AC, HFG, SFG and FFG were tried to identify optimum condition for better mechanical properties. FFG with the yield and tensile strength of 242 MPa and 327 MPa respectively and with 2.1% elongation had shown superior tensile properties. Improvement of 162% in yield strength and 226% in tensile strength was observed over as cast material. On the other hand, HFG and SFG had shown 71% and 120% improvement in yield strength and, 74% and 129% improvement in tensile strength, respectively. The results represent that the tensile properties of HFG and SFG were in between the AC and FFG samples. Hence, we can say that the properties were only dependent on proportion of processed microstructure and not on the microstructural configuration. Therefore, the rule of mixture can be applied to predict properties, as shown in Fig. 6.8. In general, any property following rule of mixture should fall between lower bound and upper bound values whose expressions for ultimate tensile strength (UTS) is given in the following equation.

$$\left(\frac{f}{\sigma_{UTS,f}} + \frac{1-f}{\sigma_{UTS,m}}\right)^{-1} \leq \sigma_{UTS,c} \leq \left(f\sigma_{UTS,f} + (1-f)\sigma_{UTS,m}\right) \quad 6.1$$

In the above equation f is the fraction of processed region. $\sigma_{UTS,f}$, $\sigma_{UTS,m}$ and $\sigma_{UTS,c}$ are the UTS of fully processed microstructure, as-cast microstructure and composite microstructure respectively. Yield strength (YS) of composite microstructures were also calculated in similar fashion by using YS of as cast and processed microstructure in place of corresponding UTS values. However, there is a deviation in yield strength from rule of mixture at SFG, as its value was more than the upper bound, as shown in Fig. 6.8(a). Unlike yield strength the tensile strengths of AC (0% fine grained region), HFG (50% fine grained region), SFG (67% fine grained region) and FFG (100% fine grained region) in Fig. 6.8(b) are well within the bounds. The deviation from rule of mixture in yield strength can be attributed to ambiguity in measurement by using 0.2 % strain offset. On the other hand, maximum load at failure can be found without any ambiguity, hence tensile strength is found to follow rule of mixture within the bounds.

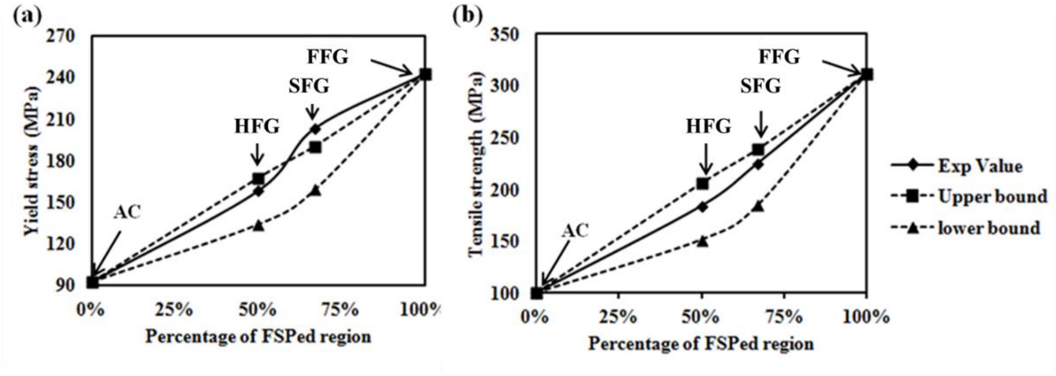

Fig. 6.8: Comparison of experimental result with the rule of mixture for (a) yield strength and (b) tensile strength. At 0%, 50%, 67% and 100% of FSPed region are indicated as AC, HFG, SFG and FFG samples respectively.

6.2.2 Strengthening mechanisms

The grain size contribution to the yield strength is evaluated using the familiar Hall–Petch relation (Eq. 2.1). The constant k depends on the type of material, microstructure and process. For the cast AZ91 alloy, σ_0 and k were taken as 11 MPa and 370 MPa $\sqrt{\mu m}$ respectively [85] and for fully FSPed AZ91 alloy, these values were 10 MPa and 160 MPa $\sqrt{\mu m}$ respectively [129]. The equation estimates that increase in strength due to grain size effect from 48 MPa in as-cast condition to 190 MPa after FSP.

The solid solution strengthening contribution was evaluated using the Eq. 2.2, where the atomic fraction of solute (Al), X is 4.7 % and 9.4 % before and after processing respectively and, $C = 197$ (MPa $X^{-2/3}$). Due to processing, the strengthening contribution from solid solution improved from 26 MPa to 43 MPa. Both grain size and solid solution strengthening made sure that processed region possess superior tensile properties when compared to the as-cast region. Hence in accordance with rule of mixture the strength of the material increases with increasing proportion of processed fine grain microstructure.

6.2.3 Fracture morphology and elongation

Like yield strength and tensile strength, elongation was also maximum for FFG. The percentage elongation of as-cast microstructure was 0.8 % whereas it was 4.7 % for FFG. The HFG and SFG had shown elongation of 1.2 % and 2.0 % respectively. From the stress-strain curve in Fig. 6.2 it can be observed that except FFG all other conditions did not show uniform plastic deformation. Stress-strain curve of FFG however showed considerable uniform plastic deformation but without significant strain hardening. Afrin et al [240,241] also observed strain hardening after FSW in AZ31 magnesium alloy. Fig. 6.6 clearly shows that crack initiated either in as-cast microstructure (AC, SFG) or in non-uniform microstructure which contain bands of processed and as-cast microstructures (HFG, FFG). Comparison of Figs. 6.3 and 6.4 on the other hand brings out the crack propagation path. In as-cast microstructure, crack path is through precipitate/matrix interface which accounts for the transgranular fracture surface. In processed material, the crack propagation is through grain boundary precipitate/matrix interface and grain boundaries, which gave it typical intergranular fracture surface. One of the method to improve ductility of any material is through strain hardening. In as-cast material, ductility was poor due to solute segregation in the interdendritic region. These regions were brittle in nature and acted as preferential sites for crack nucleation and propagation through interconnected network of interdendritic region (see Fig. 5.3(a) in Chapter 5). Since crack nucleation and propagation occurred at an early stage of deformation, the as-cast material did not get an opportunity for strain hardening. On the other hand, in the processed material the solute content was redistributed and interdendritic region was broken and uniformly distributed (see Fig. 5.3(b) in Chapter 5). Since the β phase was not continuous, grains underwent deformation before separation at the α/β interface. Both these microstructural changes allow material to exhibit significant strain hardening. It is evident in the stress-strain curves of the as-cast and processed materials. The fracture morphology also shows significant difference between the two materials. The as-cast material exhibited transgranular morphology wherein failure is primarily through cleavage of the β phase. The processed material on the other hand exhibited intergranular morphology.

6.2.4 Fracture toughness behavior

The values of the apparent notch fracture toughness of as-cast, HFG, SFG and FFG materials are 6.2 MPa√m, 10.9 MPa√m, 12.1 MPa√m and 12.3 MPa√m respectively. It follows the same trend as tensile strength that AC possess lowest notch K_Q value and FFG possess highest, whereas HFG and SFG have notch K_Q values between that of AC and FFG materials. Thus, the fracture toughness of the material was enhanced completely at full thickness grain refinement. The fracture toughness of the material depends on tensile properties which in turn depend on the grain size, according to Hall-Petch effect [242,243] . The effect of solid solution on Mg-Zn binary alloy were studied by Somekawa et al., [244] and reported that fracture toughness increases with the increase in solute concentration. Precipitate shape effect on the fracture toughness of ZK60 alloy was studied by Somekawa et al., [245] and they reported that the change in shape of precipitates from rod to spherical increases the fracture toughness of that alloy. In the present work also, after FSP, there is significant grain refinement from 100 μm to 2 μm and solute concentration increases from 5.1 wt% Al to 10.2 wt% Al. The uniform distribution of broken secondary phase particles as shown in Fig. 3(b) is responsible for enhancement in fracture toughness of the material.

Load vs. COD plot of as-cast material in Fig. 6.5(a), showed gradual drop in load after reaching its maximum. This behavior coupled with void formation and cleavage fracture observed in the fractograph (Fig. 6.6(a)) is the characteristics fracture behavior of AC material. Sharp peak load was attained in HFG and FFG with crack initiation observed at the bands of inhomogeneous microstructure as apparent from the fractograph in Fig. 6.6(b) and Fig. 6.6(d) respectively. SFG had a pop-in phenomenon observed from Fig. 6.5(a). Crack initiation in as-cast microstructure region of SFG can be observed from its fractograph (Fig. 6.6(c)). It was reported by Willoughby [246] that pop-in could occur in a heterogeneous material such as a weldment due to cleavage crack initiation in brittle region which could be arrested by the tougher matrix. In SFG, cleavage initiated from as-cast, brittle, microstructure region was arrested by tougher FSPed region, albeit not enough to increase its toughness further as the maximum load after pop-in was lower than the initial peak load. Thus any small amount of cast microstructure in FSPed region is detrimental in enhancing the tensile properties as well as crack resistance behavior.

6.3 Conclusions

The layered microstructure with variation in grain size through the thickness was processed using multipass friction stir processing and its effect on room temperature mechanical behavior were studied. The important conclusions are:

- Fully refined microstructure (FFG) exhibits superior tensile, fatigue and fracture behavior in comparison to as cast, half and surface modified fine grained materials.
- The strength of HFG and SFG, which contain different proportions of fine grain size microstructure was observed to follow the rule of mixture.
- Grain refinement with dissolved and broken up precipitates were primary reasons for improvement in tensile and fracture characteristics of multipass FSPed AZ91 alloy and any proportion of as-cast microstructure is detrimental to mechanical properties.

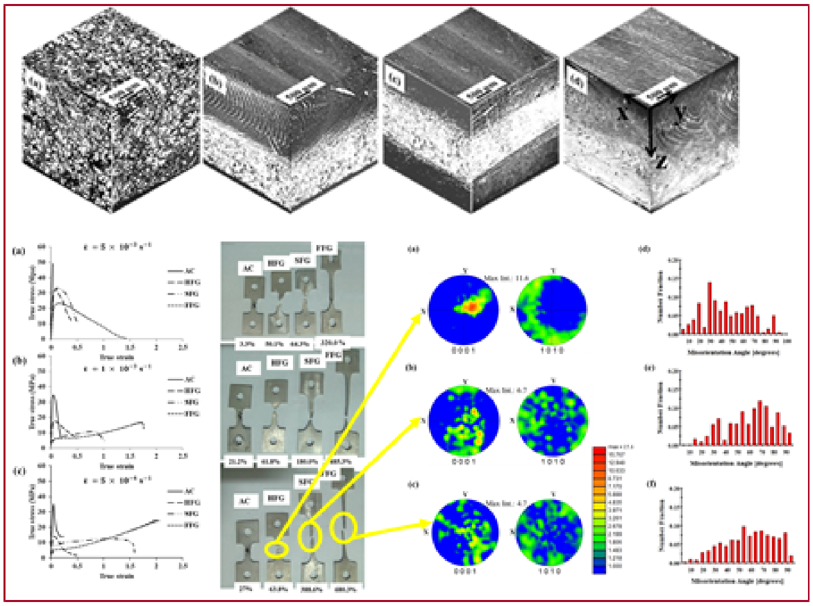

CHAPTER 7

LAYERED MICROSTRUCTURE AND SUPERPLASTICITY

OVERVIEW

The effect of layered microstructure on the superplasticity was studied by testing the tensile samples at high temperature and at three different temperatures. Texture studies before and after deformation were carried out to understand the deformation mechanism that aids the superplasticity.

CHAPTER 7

LAYERED MICROSTRUCTURE AND SUPERPLASTICITY

The effect of layered microstructures (FFG, HFG and SFG) on the superplastic deformation is studied in this chapter. High temperature tensile tests were carried out at 350°C using three different initial strain rates i.e. $5 \times 10^{-3}\ s^{-1}$, $1 \times 10^{-3}\ s^{-1}$ and $5 \times 10^{-4}\ s^{-1}$. The FFG material showed superplasticity at all strain rates and highest ductility of 680% was achieved at the strain rate of $5 \times 10^{-4}\ s^{-1}$. The AC and HFG material displayed very low elongation while SFG material exhibited superplasticity of 388 %. The superplastic behavior in SFG was due to increase in the fraction of fine grained microstructure and modification of as-cast microstructure on both the surfaces. Microstructure and texture studies revealed that grain boundary sliding accommodated by grain boundary migration and grain rotation was responsible for superplasticity in FSPed region.

7.1 Results

7.1.1 Microstructure post friction stir processing

The three dimensional (3D) macrostructural montage of AC material and materials processed with different FSP tools are shown in the Fig. 7.1. Multiple optical images were taken from orthogonal surfaces and stitched together to obtain the 3D montage.

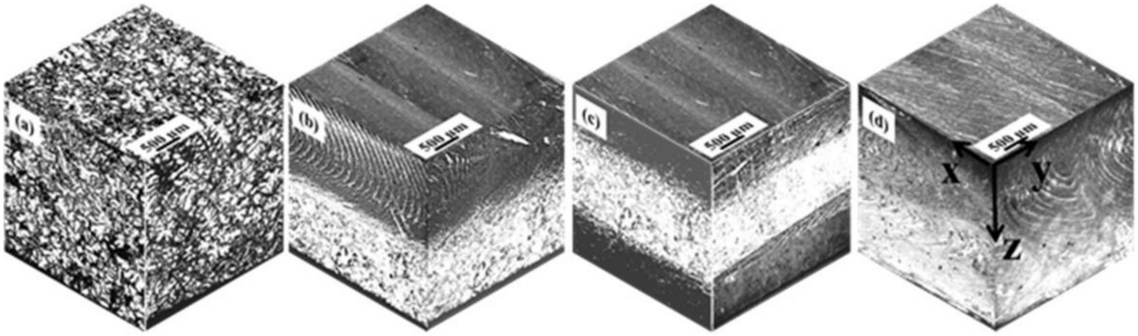

Fig. 7.1: Macrostructure of samples; a) AC, b) HFG, c) SFG and d) FFG. The process direction, transverse direction and thickness direction are represented by arrows X, Y and Z respectively.

Fig. 7.1(a) shows typical as-cast microstructure, consist of dendrites and interdendrites. The HFG material has two layers as shown in Fig. 7.1(b), one half of the thickness is FSPed region and remaining 1.5 mm of the 3 mm thick material is unprocessed region. It has semi-circular ring patterns in the XZ plane in the FSPed region. The SFG material has three layers as shown in Fig 7.1(c), the top and bottom 1 mm of the material are FSPed region and the middle 1 mm is unprocessed region. Fig. 7.1(d) exhibits fully FSPed region throughout the 3 mm thickness of the plate. It too has semi-circular ring pattern in the XY plane and onion rings in the YZ plane. The reason for microstructure obtained after multipass FSP using similar processing parameters were discussed briefly in Chapter 5.

7.1.2 Superplastic deformation

The tensile tests were carried out at 350 ºC with tensile axis parallel to the process direction. The flow curves and corresponding deformed samples obtained after the test at 350ºC and three different strain rates of 5×10^{-3} s^{-1}, 1×10^{-3} s^{-1} and 5×10^{-4} s^{-1} are shown in the Fig. 7.2(a), Fig. 7.2(b) and Fig. 7.2(c) respectively. As-cast material exhibited no superplasticity but its ductility increased from approximately 3 % at 5×10^{-3} s^{-1} to 27 % at 5×10^{-4} s^{-1}. The HFG material also showed elongation in the range of 50 % to 64 %. The flow behavior of SFG material at the strain rate of 5×10^{-3} s^{-1} is similar to that of HFG material which can be observed from the Fig. 7.2(a). However, it exhibited 180 % elongation at 1×10^{-3} s^{-1} strain rate and nearly 390 % elongation at 5×10^{-4} s^{-1}. On the contrary, FFG material exhibited superplasticity at all strain rates with a noticeable difference in percentage elongation at different strain rates; 320 % at 5×10^{-3} s^{-1}, 485 % at 1×10^{-3} s^{-1} and 680 % at 5×10^{-4} s^{-1}. The FFG material showed flow softening at 5×10^{-3} s^{-1} whereas at 1×10^{-3} s^{-1} and 5×10^{-4} s^{-1} it showed strain hardening. During superplastic deformation, hardening can occur either due to dislocation activity or dynamic grain growth.

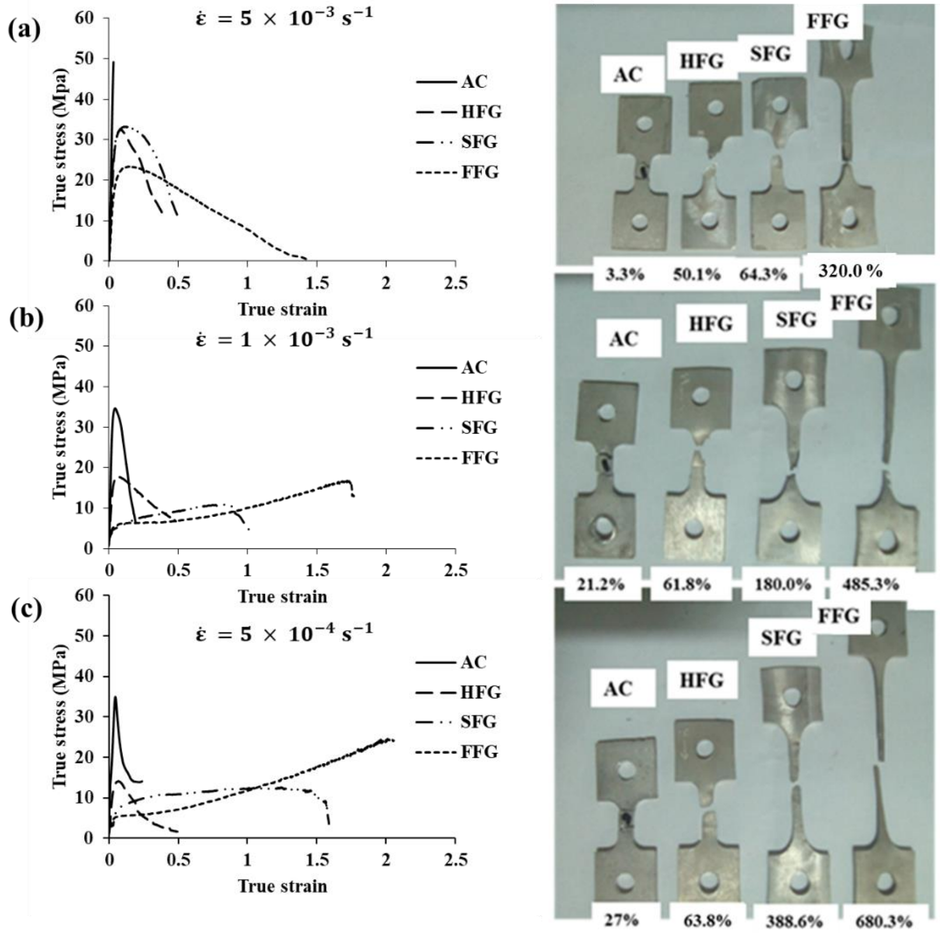

Fig.7.2: True stress versus true strain curves and corresponding deformed samples after deformation at 350ºC and at strain rates of a) 5 × 10^{-3} s^{-1}, b) 1 × 10^{-3} s^{-1} and c) 5 × 10^{-4} s^{-1}.

7.1.3 Strain rate sensitivity

The important parameter that defines superplasticity of a material is strain rate sensitivity (*m*). It measures the variation in flow stress as a function of strain rate. The strain rate sensitivity index (*m*) of the material was calculated employing the following equation (Eq. 7.1):

$$m = \frac{\partial ln\sigma}{\partial ln\dot{\varepsilon}} \qquad 7.1$$

In the equation σ is flow stress and $\dot{\varepsilon}$ is initial strain rate at which the test was carried out. The *m* values of all the four materials measured at peak load is given in the Table 7.1.

Table 7.1: Strain rate sensitivity measured at peak load

Material	‘m’ value at peak load
AC	0.16
HFG	0.36
SFG	0.60
FFG	0.54

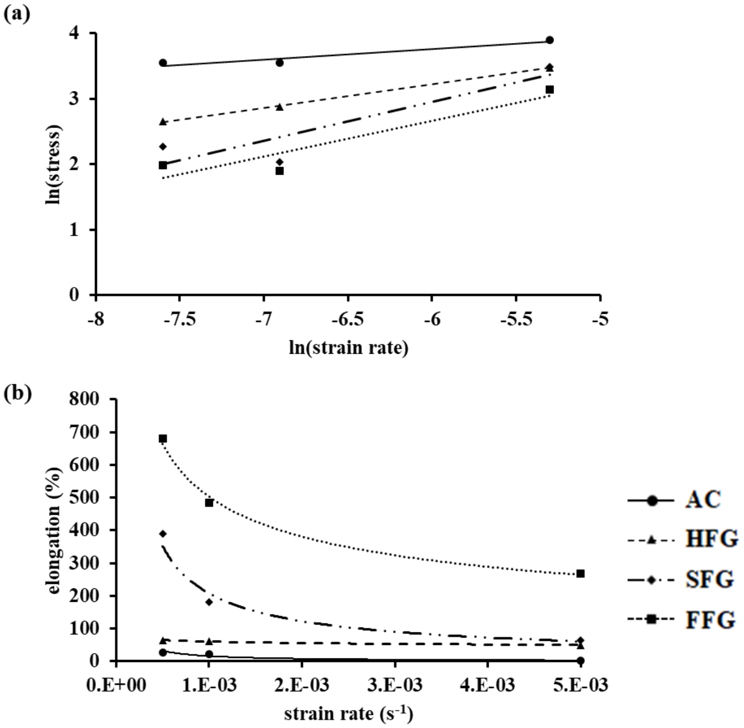

Fig. 7.3: (a) Flow stress vs. strain rate and (b) elongation vs. strain rate.

The strain rate sensitivity measured from slope of the linear fits in Fig. 7.3(a) was compared with their corresponding elongation versus strain rate in Fig.7.3(b). The elongation of AC and FFG materials was in accordance with their *m* values. However, elogation of layered microstructured materials, HFG and SFG was quite low in comparison to the *m* values (Fig. 7.3(b)). Cao et al. [247] also reported elongation of 55.6 % from their work on LAZ922 Mg alloy although *m* value exhibited by the maetrial was 0.64. It implies that the high *m* value is a necessary but not sufficient condition for a material to behave superplastically.

7.1.4 Fracture surfaces

Figure 7.4 shows fractographs of samples deformed at 350 ºC and at strain rate of 1 × 10^{-3} s^{-1}. Low magnification fractographs of AC (Fig. 7.4(a)), HFG (Fig. 7.4(b)), SFG (Fig. 7.4(c)), and FFG (Fig. 7.4(d)) are showing distinct features in processed region and unprocessed region. The AC material showed lower ductility and its fracture surface have both cleavage and dimples as shown in the Fig. 7.4(e) and Fig. 7.4(f) respectively.

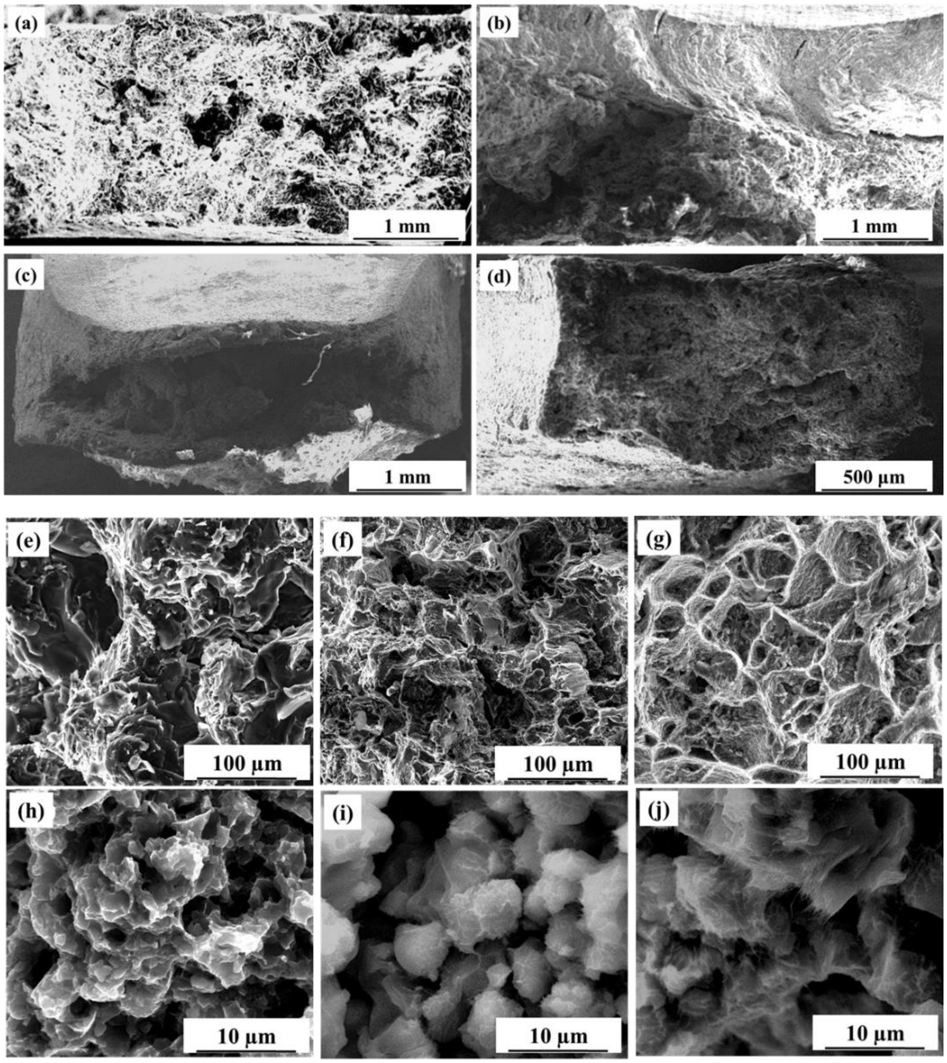

Fig. 7.4: Low magnification fractographs of tensile samples tested at 350ºC and at a strain rate of 1 × 10^{-3} s^{-1}; (a) AC, (b) HFG, (c) SFG and (d) FFG. Higher magnification fractographs reveal (e) brittle fracture region in AC material, (f) brittle and ductile mix mode fracture regions in AC material, (g) ductile fracture in as-cast region of HFG material, (h) intergranular fracture in FSPed region in HFG material, (i) intergranular fracture in FSPed region of SFG material and (j) fibres due to grain separation at high strain in FFG material.

As-cast region of HFG material showed (62 % elongation at 1 × 10^{-3} s^{-1}) dimples in their fracture morphology (Fig. 7.4(g)) whereas, FSPed region of HFG materials showed intergranular fracture surface in Fig. 7.4(h). Similar intergranular fracture can be observed in FSPed region of SFG and FFG materials in Fig. 7.4(i) and Fig. 7.4(j) respectively. On comparing the fracture surface of FSPed region in HFG with SFG, it appears that the size of the grains were larger in SFG material. Interestingly, SFG showed higher elongation than HFG material. Fracture surface of FFG material in Fig. 7.4(j) showed fibres in addition to intergranular fracture. Fibres were formed during grain separation at high strain values, in excess of 1.5 true strain.

7.1.5 Microstructure and texture after superplastic deformation

EBSD scans were used to analyse the microstructure after fracture. The scans were performed in FSPed region to understand the microstructural evolution during deformation and presented in Fig.7.5.

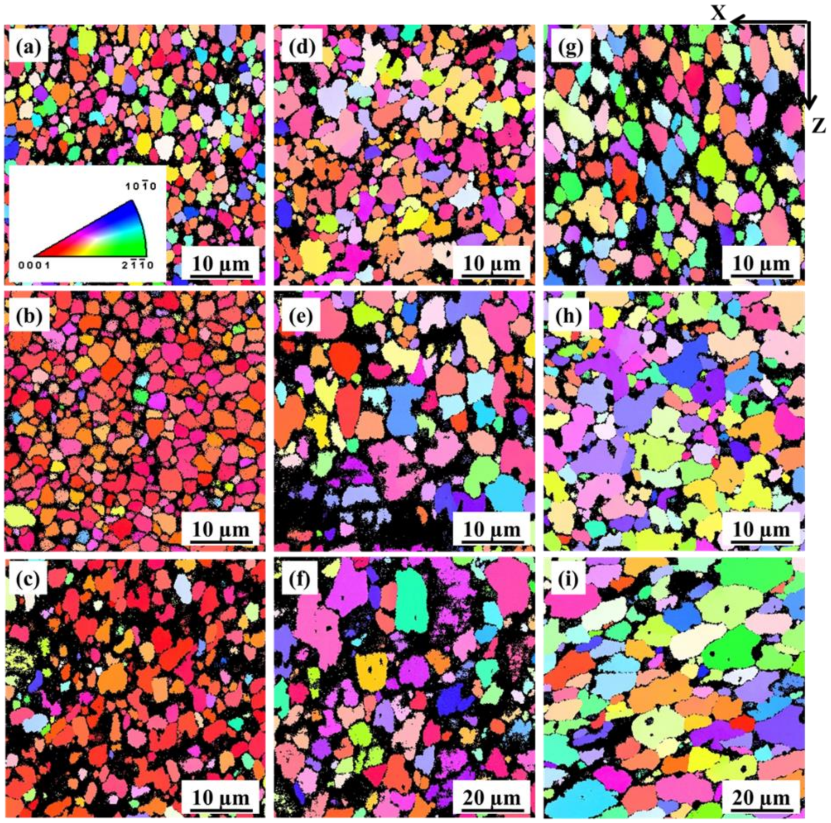

Fig. 7.5: IPF maps obtained from EBSD scans of FSPed region in x-z plane close to the fracture surface of tensile tested samples; (a), (b) and (c) are from HFG material, (d), (e) and (f) are from SFG material and (g), (h) and (i) are from FFG material. The ascending order of every material is corresponding to 5 × 10^{-3} s^{-1}, 1 × 10^{-3} s^{-1} and 5 × 10^{-4} s^{-1}.

The images were cropped for the sake of clarity while comparing the microstructure. On comparing the FSPed microstructure, for example in HFG materials, with decreasing strain rate in Fig. 7.5(a) to 7.5(c), the grain size increases from 1.6 to 2.0 µm. Similarly, in SFG (Fig. 7.5(d), (e) and (f)) and FFG (Fig. 7.5 (g), (h) and (i)) with decreasing strain rate the grain size increased after deformation. There is considerable difference in the final grain size after deformation in the FSPed region of HFG (2.0 µm), SFG (5.1 µm) and FFG (9.6 µm) at the lowest tested strain rate of 5×10^{-4} s^{-1}. This confirmed that dynamic grain growth occurred in FFG material as the grain size was higher for the material which experienced higher strain at lower strain rate.

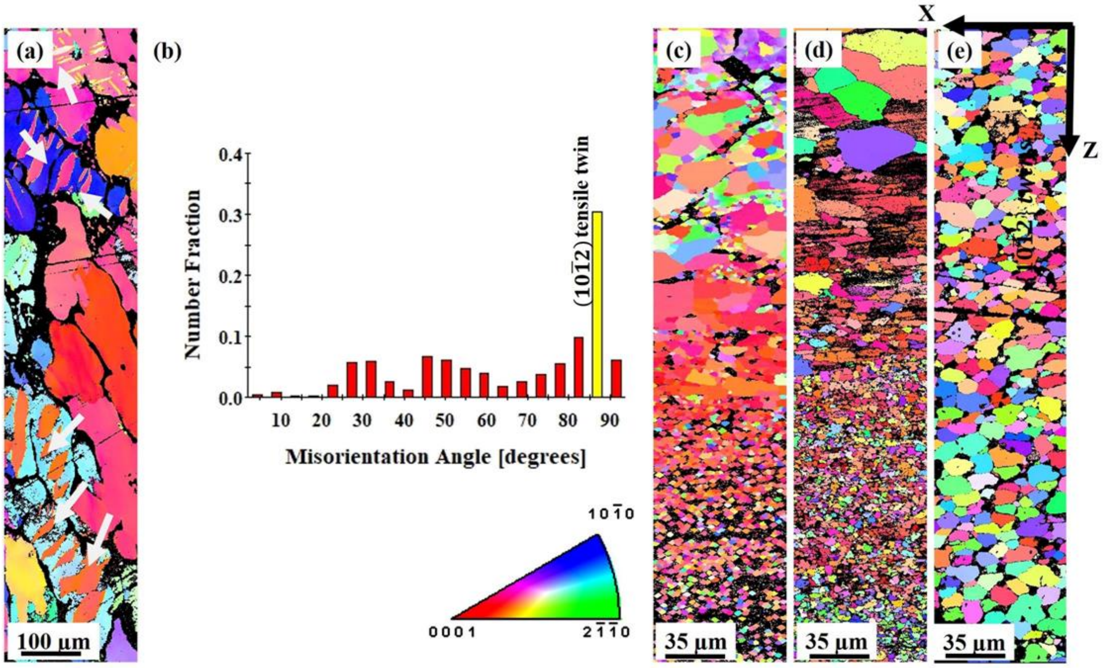

Fig.7.6: IPF maps of deformed samples with tensile axis parallel to process direction (parallel to X-axis shown above) at a strain rate of 5×10^{-4} s^{-1}; (a) AC material with highlighted (yellow) extension twins indicated by arrows in its IPF map and (b) grain boundary misorientation distribution of as-cast material showing predominant tensile twin population around 86.3^{0}, (c) HFG, (d) SFG and (e) FFG.

The EBSD map of materials tested at strain rate of 5×10^{-4} s^{-1} covering both the as-cast and FSPed microstructure in HFG and SFG materials and similar length scale maps from AC and FFG materials were collected and presented in Fig. 7.6. The tensile direction is horizontal in the plane of the paper. Considerable texture evolution accompanied by grain growth occurred during superplastic deformation in fine grained region. The IPF map of as-cast material showed twins in some grains probably due to unfavourable orientation of the grains for slip (Fig. 7.6(a)). The twins were identified as extension twins from the grain boundary misorientation distribution (Fig. 7.6(b)) in as-cast material, which have predominantly 86.3° misorientation angle. IPF map of deformed HFG material is shown in Fig. 7.6(c). The HFG microstructure consists of few recrystallized grains in as-cast region and finer grains with strong basal orientation in FSPed region. IPF map of SFG material in Fig. 7.6(d) showed texture randomization in the FSPed region, whereas, as-cast material did not show any microstructure evolution. However, in Fig. 7.6(e) the FFG material showed considerable grain growth having equi-axed grain morphology and random texture after the deformation.

7.2 Discussion

7.2.1 Superplastic behavior of inhomogeneous microstructure

This work was intended to study the effect of microstructural modification and introduction of inhomogeneous microstructure on superplasticity in Mg alloys. In general, inhomogeneity in initial material would lead to inhomogeneous deformation and strain localization which eventually lead to failure [248]. In classical superplastic literature, uniform fine grained microstructure was considered favourable for superplasticity. However in Al alloys, inhomogeneous microstructure has shown to exhibit higher ductility than homogeneous fine grain microstructure [207–209,234]. Pancholi et al. [249] demonstrated that at least 50% fine grain microstructure is required in the Al 5086 alloy for it to exhibit superior superplasticity when compared to the homogeneous fine grained material. It was argued that microstructural refinement in remaining 50% of coarse grain microstructure, which lead to fully homogenous microstructure in the material, was the reason for higher superplasticity [234,250]. However in the present work, layered microstructure material exhibited elongation lower than fully fine grained microstructure. Lack of superplasticity in HFG and SFG can be attributed to insignificant microstructural refinement in the coarse grain, as-cast microstructure during deformation, as shown in the Fig. 7.6(c) & the Fig. 7.6(d). It is well established that Al alloys exhibit continuous dynamic recrystallization (CDRX) [251,252]whereas, AZ91 Mg alloys exhibit discontinuous dynamic recrystallization [253]. It appears that CDRX of coarse grains in the layer microstructure of Al alloys was the primary reason for higher superplastic elongation in Al alloys which was not present in the AZ91 Mg alloy. However, elongation of more than 600 % and strain rate sensitivity of more than 0.5 in FFG material confirmed that friction stir processed AZ91 behave superplastically at a temperature of 350 °C and at strain rate of 5×10^{-4} s^{-1}.

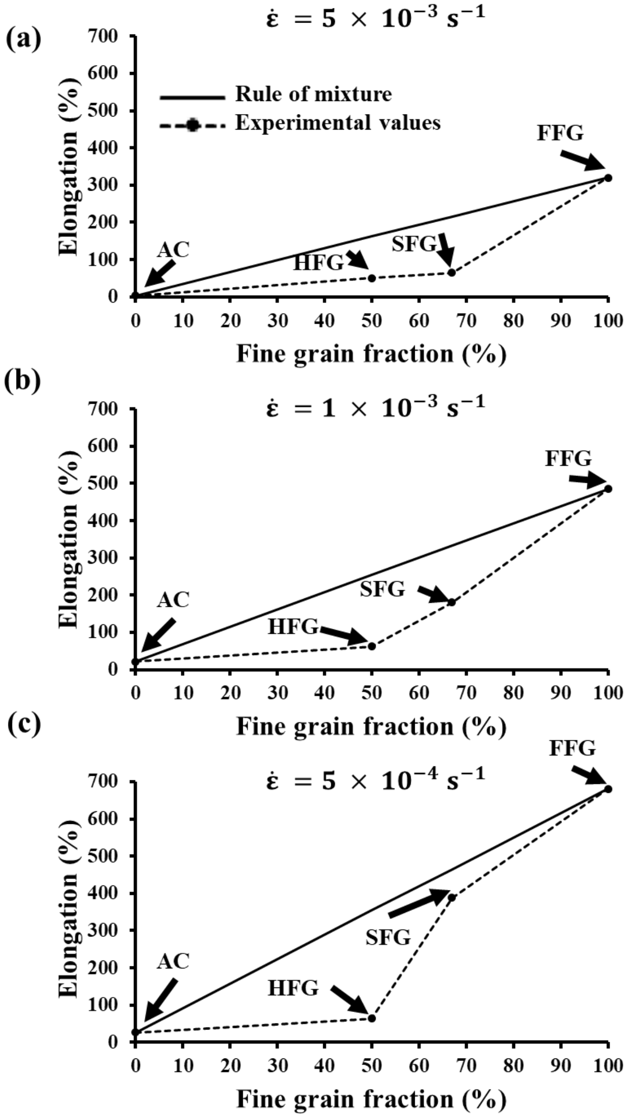

Fig. 7.7: Comparison of superplastic elongation in FSPed layered microstructure with the rule of mixture: a) 5×10^{-3} s^{-1}, b) 1×10^{-3} s^{-1} and c) 5×10^{-4} s^{-1}.

The superplastic elongation results of HFG and SFG were in between the AC and FFG samples. It appears that the properties were dependent on proportion of the processed microstructure. In order to understand behavior of HFG and SFG material as a composite of different microstructures, the superplastic elongations are compared with the rule of mixture given by Eq. 7.2 and shown in Fig. 7.7.

$$e_c = f \times e_f + (1 - f) \times e_m \qquad 7.2$$

where, f is the fraction of processed region and e_f, e_m and e_c are the elongation of fully processed microstructure, as-cast microstructure and composite microstructure, respectively. It is clear that elongation values are not exactly following the rule of mixture at the strain rates 5 × 10^{-3} s^{-1} (Fig. 7.7(a)) and 1 × 10^{-4} s^{-1} (Fig. 7.7(b)) but the value is approximately similar for SFG material deformed at 5 × 10^{-4} s^{-1} (Fig. 7.7(c)). The elongation values for different proportions of fine grain microstructure is significantly lower than the value predicted by the rule of mixture. Elongation of HFG materials was relatively close to AC materials at all strain rates. On the other hand, elongation of SFG increased with decrease in strain rate. It is clear that total elongation not only depends on proportion of fine grain microstructure but also on their distribution. In HFG material, fine grain microstructure was 50 % from one end and the other half contain as-cast microstructure whereas in SFG, both the surfaces contain fine grain microstructure with 67 % overall fraction of fine grain microstructure. Comparison of fractographs in Fig.7.4(b) and (c) indicate that in HFG material, fracture initiated in as-cast region and both the microstructural regions failed at the same time. On the other hand, in SFG the fine grained region showed considerable necking after failure of as-cast region. It is well known that surface irregularities are more critical than internal defects. One of the surface of HFG material consist of coarse dendrites and brittle interdendritic as-cast microstructure. Having brittle microstructure at the surface in case of HFG result in early onset of instability at final fracture.

7.2.2 Deformation mechanism

In AC material, slip as well as tensile twins contributed to the ductility it achieved at the strain rate of 5 × 10^{-4} s^{-1}, as observed from the IPF map in Fig. 7.6(a). In fine grained materials exhibiting superplasticity, GBS was reported as the primary deformation mechanism. Other than GBS, diffusion creep was found in Al alloys with high solute content [254,255]. In the present work, grain growth and equiaxed morphology was observed in FSPed region of all materials. In fact, grain growth was found to be proportional to the amount of deformation. Recently, Figueiredo et al. [65] reported similar grain growth during superplastic deformation of pure Mg at low temperatures. The grain growth was mostly static at low strain rate but strain enhanced dynamic grain growth might also contribute. Carpenter et al. [256] observed that without strain the rate of grain growth was lower than with strain at a constant temperature. Moreover, dynamic grain growth during superplastic deformation leads to strain hardening and prevents necking at low strain rate [257,258] which is evident from the flow curves and deformed samples presented in Fig.7.2. Moreover, in textured Mg alloys, interaction of slip systems gives rise to strain hardening [259]. Wilkinson and Caceres [258] studied the mechanism of dynamic grain growth during superplastic deformation. It was stated that strain localization at triple junction enhances normal grain growth and grains remain equi-axed due to GBS.

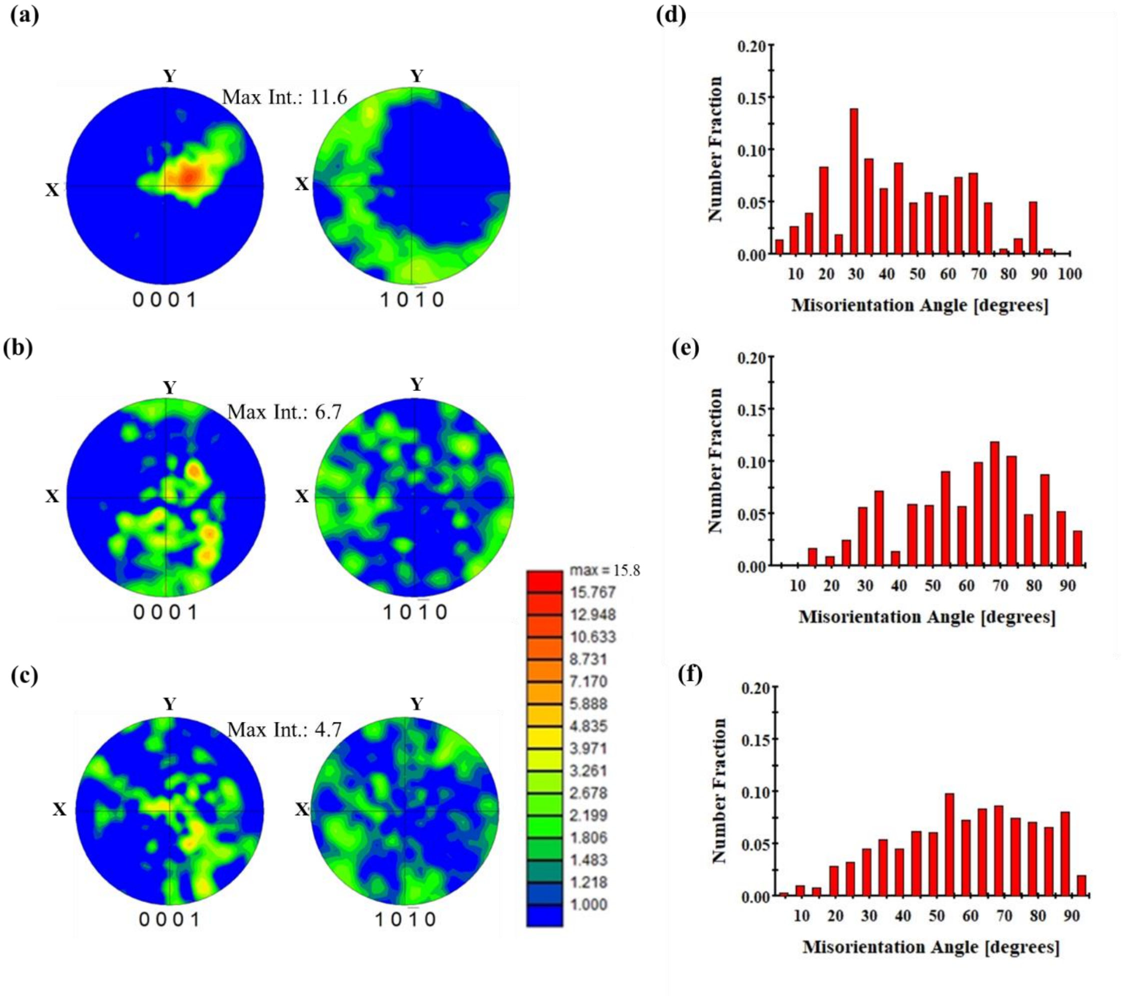

Fig. 7.8: Pole figures of FSPed region in deformed samples; (a) HFG, (b) SFG and (c) FFG at strain rate of 5×10^{-4} s^{-1} and their corresponding grain boundary misorientation distributions at (d), (e) & (f).

GBS requires an accommodation mechanism in order to avoid stress concentration due to impediments or in other words to make grain boundary mobile. The accommodation mechanism could be grain boundary migration, recrystallization, diffusion creep or dislocation slip. The pole figure in Fig. 7.8(a) showed basal texture in HFG material at the strain rate of 5×10^{-4} s^{-1}. The randomization of texture and reduced intensity in FSPed region with increasing ductility in SFG material is clear in Fig. 7.8(b). It becomes completely random in FFG material where it fails at a fairly large true strain of 2 (Fig. 7.8(c)). Moreover, the fraction of 30^o grain boundary misorientation in FSPed region before deformation (Fig. 5.7(c)) can be observed in HFG material (Fig. 7.8(d)) even after the deformation at the strain rate of 5×10^{-4} s^{-1}. Further, it becomes gradually distributed into higher misorientation angles with the increase in superplastic elongation in SFG (Fig. 7.8(e)) and in FFG (Fig. 7.8(f)) materials, which ensures grain rotation due to migration of grain boundaries. It further supports the argument of texture randomization during superplastic deformation. Similar change in texture from basal to random after superplastic deformation was observed in Mg alloys by Kandalam et al. [260] and Watanabe et al. [261]. Hence, GBS accommodated by grain boundary rotation and migration is the deformation mechanism responsible for superplasticity of FSPed AZ91 Mg alloy.

7.3 Conclusions

The layered microstructure with variation in grain size through the thickness of AZ91 Mg alloy was processed using multipass friction stir processing and tensile test was carried out at three different strain rates at 350 °C. The important conclusions of the work are:

- Fully refined microstructure (FFG) displayed superplasticity at all tested strain rates with a maximum elongation of 680 % at the strain rate of 5×10^{-4} s^{-1}.
- The AC and HFG material showed improvement in ductility but failed to show any superplasticity while SFG material exhibited superplasticity at 1×10^{-3} s^{-1} and 5×10^{-4} s^{-1}.
- As-cast microstructure is detrimental to superplasticity as it debonds easily at the interface of brittle interdendrites. FSPed region with the microstructure of fine grains and evenly distributed precipitates is favorable microstructure for superplastic elongation.
- Grain growth, change in texture from basal to random and decrease in the fraction of 30° grain boundary misorientation angle with deformation in the FSPed region indicates that GBS accommodated by grain rotation and grain boundary migration is the deformation mechanism responsible for superplasticity.

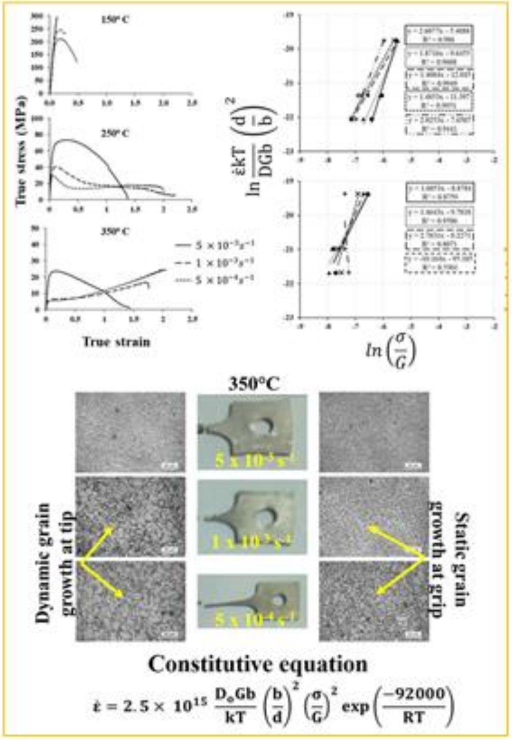

CHAPTER 8

CONSTITUTIVE EQUATION

OVERVIEW

Full thickness fine grained material was subjected to high temperature tensile test. A constitutive equation for the superplastic behavior of FSPed AZ91 Mg alloy was developed using the data obtained from the test results.

CHAPTER 8

CONSTITUTIVE EQUATION

In this chapter, a constitutive equation for the superplasticity of FSPed AZ91 Mg alloy was developed. The tensile samples were tested at 150 ºC, 250 ºC and 350 ºC and at three strain rates; 5 × 10^{-3} s^{-1}, 1 × 10^{-3} s^{-1} and 5 × 10^{-4} s^{-1} on each temperature. The results were used to evaluate the material parameters of constitutive equation. The calculated material parameters found to vary with the strain. The flow curves tested at 250 ºC and 350 ºC exhibited strain hardening behavior. Microstructures were obtained from the XZ plane at grip and at fractured-tip of the tested samples. Dynamic grain growth was evident from the observed microstructures. The reason for the variation of material parameters with strain was due to the strain hardening caused by dynamic grain growth. The reason for maximum superplastic elongation of 818 % exhibited at 250 ºC and at a strain rate of 1 × 10^{-3} s^{-1} was because of the more stable grain size at this test condition.

8.1 Results

8.1.1 Superplastic deformation

The flow curves of samples tensile tested at 150 ºC, 250 ºC and 350 ºC and at three different strain rates of 5 × 10^{-3} s^{-1}, 1 × 10^{-3} s^{-1} and 5 × 10^{-4} s^{-1} at each temperature are shown in the Fig.8.1. The Fig. 8.1(a), (b) & (c) shows the comparison of flow behavior with respect to temperature at strain rates 5 × 10^{-3} s^{-1}, 1 × 10^{-3} s^{-1} and 5 × 10^{-4} s^{-1} respectively . The Fig. 8.1(d), (e) & (f) shows the flow behavior with respect to strain rates at temperatures 150 ºC, 250 ºC and 350 ºC respectively. The material did not showed superplasticity at 150 °C. At 250 ºC and 350 ºC the material exhibited superplasticity at all strain rates. Strain hardening was observed in the flow curves of samples tested at 350 ºC and 250 ºC and at the strain rates 1 × 10^{-3} s^{-1} and 5 × 10^{-4} s^{-1}. However, it was more apparent in the flow curve obtained by testing at 350 ºC than at 250 ºC. This variation in flow behavior with strain can be understood on the basis of microstructural changes occurred concomitantly during superplastic deformation. Hence, it is necessary to evaluate the parameters of the constitutive Eq. 8.1 [262] with respect to strain.

$$\dot{\varepsilon} = \frac{AD_0Gb}{kT}\left(\frac{\mathbf{b}}{d}\right)^p \left(\frac{\sigma}{G}\right)^n \exp\left(\frac{-Q}{RT}\right) \qquad 8.1$$

In the above equation, $\dot{\varepsilon}$ is strain rate, σ is flow stress, A is a dimensionless constant, $D = D_0\exp\left(\frac{-Q}{RT}\right)$ is diffusion co-efficient, Q represents activation energy, $G = (1.92 \times 10^4 - (8.6T))$ denotes shear modulus, where T is temperature in Kelvin, **b** is Burger's vector, p is grain size exponent, n is stress exponent = 1/*m* (*m* is strain rate sensitivity), k is Boltzmann constant = 1.38×10^{-23} J/K and R is Gas constant = 8.314 J mol^{-1} K^{-1}.

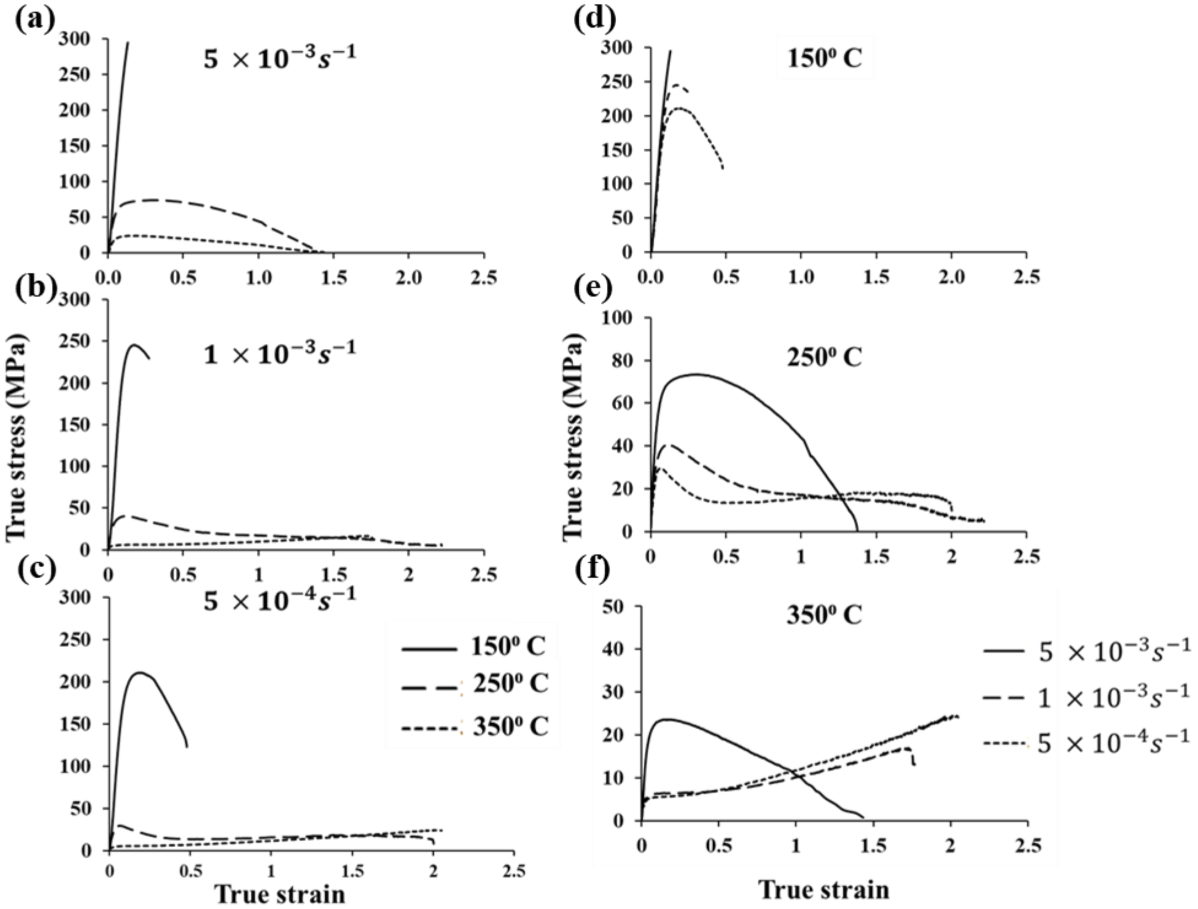

Fig. 8.1: True stress vs True strain curves of samples tensile tested at 150 °C, 250 °C and 350 °C and at three different strain rates of 5×10^{-3} s^{-1}, 1×10^{-3} s^{-1} and 5×10^{-4} s^{-1} at each temperature. Flow stress behavior with respect to temperature at strain rates; (a) 5×10^{-3} s^{-1}, (b) 1×10^{-3} s^{-1} and (c) 5×10^{-4} s^{-1}. Flow stress behavior with respect to strain rate at temperatures: (a) 150 °C, (b) 250 °C and (c) 350 °C.

The Fig. 8.2 shows percentage elongation at different strain rates with respect to temperature. At 150 ºC the flow curve at a strain rate of 5×10^{-4} s^{-1} exhibited considerable elongation of 62 % but no superplastic deformation. The total elongation to failure generally supposed to increase with increasing temperature and decreasing strain rate. At 350 °C, the material exhibited elongation of 320 %, 485 % and 680 % at the strain rates of 5×10^{-3} s^{-1}, 1×10^{-3} s^{-1} and 5×10^{-4} s^{-1} respectively. However, at 250 ºC and at a strain rate of 1×10^{-3} s^{-1} the material exhibited maximum elongation of 818 %.

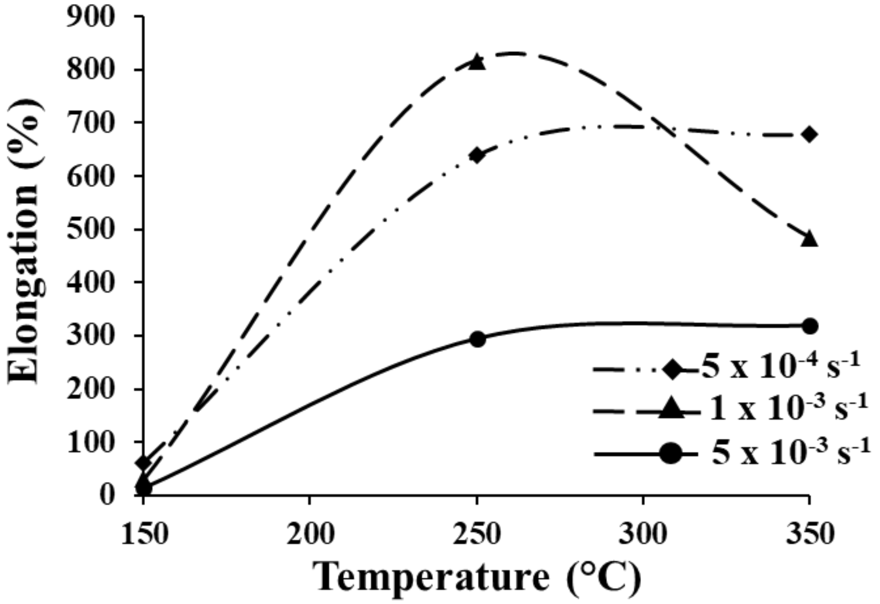

Fig. 8.2: Elongation versus Temperature at different strain rates.

8.1.2 Strain rate sensitivity (*m*)

The value of *m* determined from the plot of ln (σ) against ln ($\dot{\varepsilon}$) at a true strain of 0.2 is presented in Fig 8.3(a). The strain rate sensitivity (*m)* was measured using Eq. 7.1 at a true strain values of 0.1, 0.2, 0.5, 0.7 and 1.

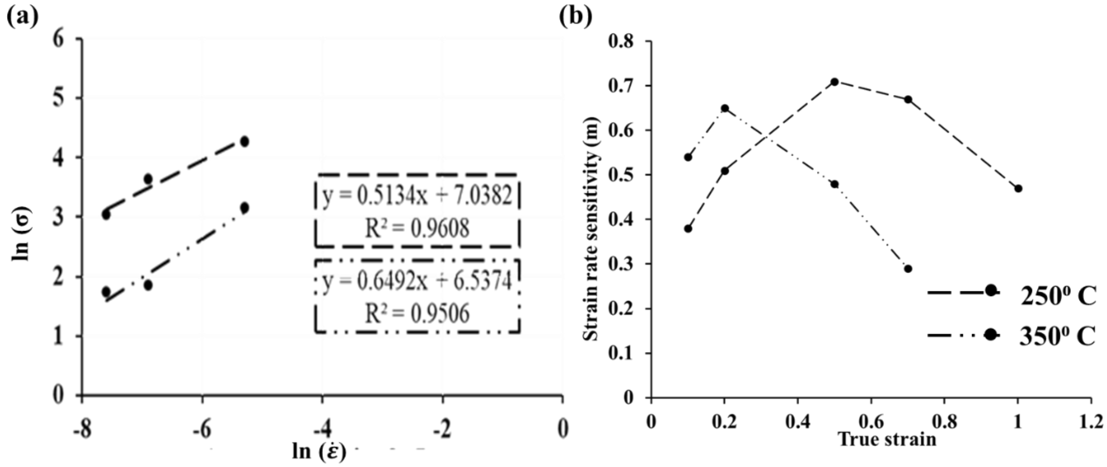

Fig. 8.3: (a) Plot of ln (σ) vs ln ($\dot{\varepsilon}$) to evaluate *m* value at a true strain of 0.2 and (b) Plot showing variation of *m* with strain

The variation of *m* value with strain is shown in the Fig. 8.3(b). The *m* value at 250 ⁰C found to increase from 0.38 at a true strain of 0.1 to 0.71 at a true strain of 0.5 and then decreases to 0.47 at a true strain of 1. At 350 ⁰C it increases from 0.54 at a true strain of 0.1 to 0.65 at a true strain of 0.2 and then decreases to 0.29 at a true strain of 0.7. The maximum value of *m* was 0.71 at 250 ⁰C and at a strain of 0.5. At 350 ⁰C the maximum *m* value was 0.65 at a strain of 0.2. Increasing "m" value implies that the microstructure evolution favours the superplastic deformation up to a true strain value where it reaches the maximum. On observing the corresponding flow curves in Fig. 8.1 at 250 ⁰C and 350 ⁰C, the strain hardening seems to initiate at these true strain values.

8.1.3 Stress exponent (n)

The stress exponent (n) at various strain values are evaluated by plotting all the data available from experiment at appropriate strain. The n value at 250 °C and 350 °C is the slope value on plotting the relation 8.2 as shown in the Fig. 8.4.

$$ln\frac{\dot{\varepsilon}\mathrm{kT}}{\mathrm{DGb}}\left(\frac{\mathrm{d}}{\mathrm{b}}\right)^{2}\text{against } ln\left(\frac{\sigma}{G}\right) \tag{8.2}$$

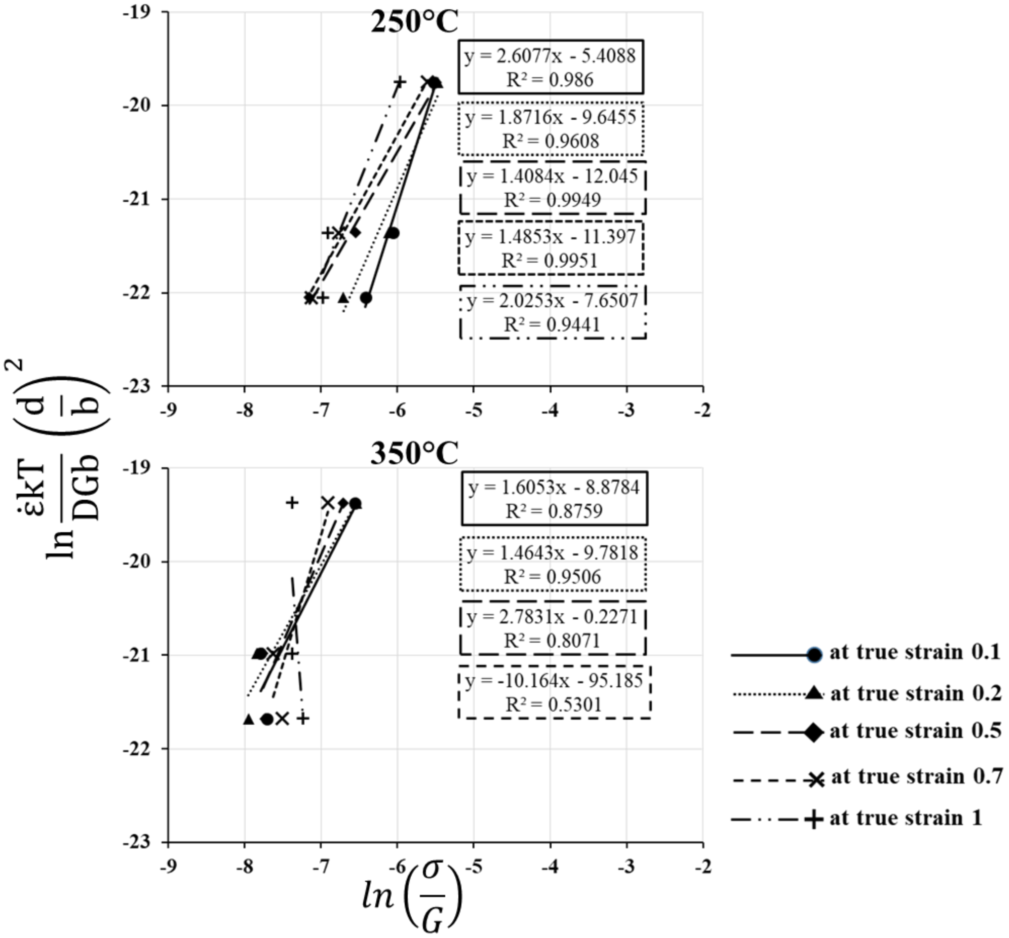

Fig. 8.4: Plots to evaluate stress exponent "n".

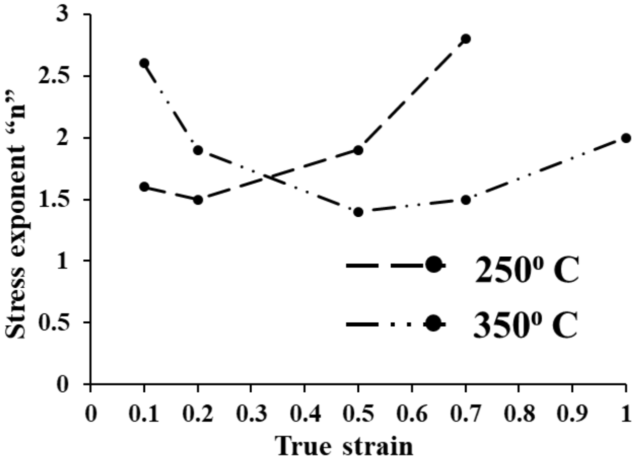

Fig. 8.5: Variation of stress exponent "n" with true strain.

For materials deforms by GBS, the grain size exponent (p) was considered as 2 [263]. The variation in "n" value with strain is shown in the Fig. 8.5. It was in the range of approximately 1.5 to 2.5. At 250 °C, the n value was 2.6 at a true strain of 0.1 and decreases up to 1.5 at a true strain of 0.7 and increases further to 2.0 at a true strain of 1. Similarly at 350 °C, the n value was 1.6 at a true strain of 0.1 decreases to 1.5 at a true strain of 0.2. On further increase in strain to 0.5 the n value increased to 2.7. The variation in n values with respect to strain are similar to the variation of *m* and Q, which can be correlated with the strain hardening behavior observed from the flow curves.

8.1.4 Activation energy

The activation energy (Q) were evaluated using the Eq. 8.3 [264]. The plot between ln (σ) versus 1/T as shown in the Fig. 8.6 gives the slope value, which has to be substituted in Eq. 8.3 to obtain the Q value.

$$Q = -nR\left(\frac{\partial \ln \sigma}{\partial \left(\frac{1000}{T}\right)}\right) \qquad 8.3$$

The variation of calculated activation energy with strain at 250 °C and 350 °C are presented in Fig 8.7(a) and Fig 8.7(b) respectively. The calculated activation energies shows variation with respect to strain as well as temperature. The Q value was found close to the grain boundary diffusion of Mg which is 92 kJ/mol whereas the Q value for lattice diffusion is 140 kJ/mol [202]. The values are considerably higher at 250 °C (Fig. 8.7(a)) compared to that at 350 °C (Fig. 8.7(b)). Mostly, the Q values found to decrease with strain except at the strain rate of 5×10^{-3} s^{-1}. It implies that as the deformation progress some factors influence the grain boundary diffusion process and reduces the required energy to activate grain boundary diffusion.

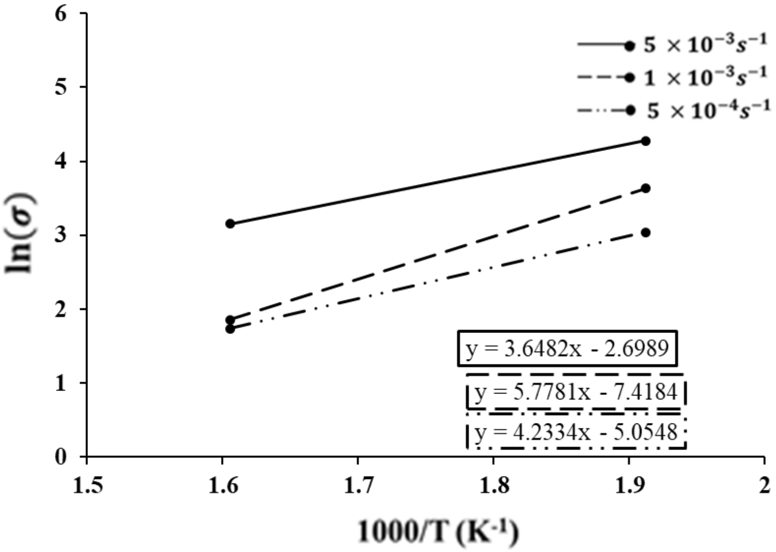

Fig. 8.6: Plot of ln (σ) vs 1000/T at a true strain of 0.2 to find the slope and calculate activation energy.

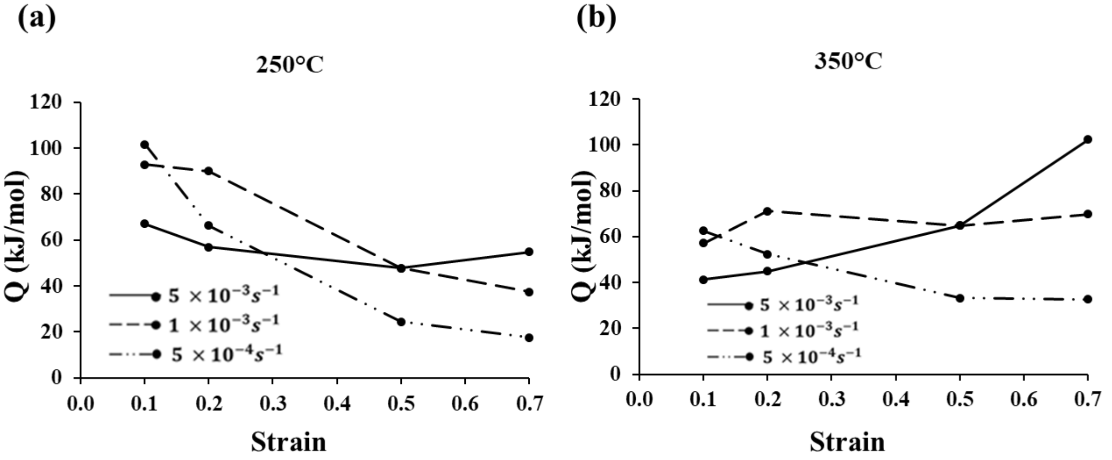

Fig. 8.7: Variation of activation energy with strain during the superplastic deformation at (a) 250 °C and (b) 350 °C.

8.1.5 Constitutive equation

As the material exhibited variation in flow behavior with increasing strain, the constitutive equation was developed based on the initial deformation condition at the true strain of 0.2. The grain size exponent (p) was considered as 2 due to GBS. As the stress exponent varies from 1.5 to 2.5, the average value of 2 was considered and the Q value calculated showed that it was corresponding to grain boundary diffusion (92 kJ/mol). The material constant, A, was calculated, using all the necessary data at the true strain 0.2 in the Eq.8.1. the A value turned out as 2.5 x 10^{15}. Hence the constitutive equation for superplasticity of friction stir processed AZ91 Mg alloy is given as Eq. 8.4.

$$\dot{\varepsilon} = 2.5 \times\ 10^{15}\ \frac{D_O G b}{kT}\ \left(\frac{b}{d}\right)^2 \left(\frac{\sigma}{G}\right)^2 exp\left(\frac{-92000}{RT}\right) \qquad 8.4$$

8.2 Discussion

Generally strain does not play any role in characterizing the flow behavior during high-temperature steady-state deformation. However, if there is any change in the microstructure that disrupts steady-state flow, then the strain would influence the flow behavior. If such changes are not considered while evaluating the materials parameters of the constitutive equation the steady-state equation will become misrepresentative. This aspect of change in flow behavior during superplastic deformation was reported in IN744 steel due to concurrent occurrence of strain hardening and strain softening by Kashyap and Mukerjee [265]. The microstructural evolutions such as, long and coarse grains become equi-axed, and grain growth were observed in the superplastic materials by Suery and Baudelet [266]. This denotes that there is an extensive microstructural evolution either in the grain size or in the defect structure during superplastic deformation. Moreover, the *m* values obtained from the constant stain-rate tests and change in strain-rate tests are often not in accord with each other [267]. Backofen et al [268] showed that a gradually falling in strain rate sensitivity could be explained by the gradual change in the microstructure during deformation. Hedworth and Stowell [269] mentioned that it is not possible to obtain true steady-state condition.

In this work, the flow curves at the temperature of 250 °C and 350 °C and at strain rates of 1 × 10^{-3} s^{-1} and at 5 × 10^{-4} s^{-1} exhibited strain hardening which can be observed in the Fig. 8.1. The strain hardening is severe in the case of materials tested at 350 °C. It denotes that the flow is not a steady-state deformation. Hence, the *m* value and the material parameters Q and n in the Eq. 8.1 are evaluated at different strain values. At 250 °C the *m* value reaches its maximum at a true strain of 0.7 and at 350°C it reaches its maximum at a true strain of 0.2. It has to be noted that at 250 ºC the *m* value close to 0.5 even at the true strain of 1 and at 350 ºC the *m* value reaches to 0.29 at a true strain of 0.7. It can be correlated with the strain hardening observed in the flow curves (Fig. 8.1). At 250 ºC, strain hardening was observed to begin after the true strain of 0.5 while at 350 ºC the strain hardening begins at the true strain of approximately 0.2. As the strain hardening progresses the *m* value observed to decrease with the strain.

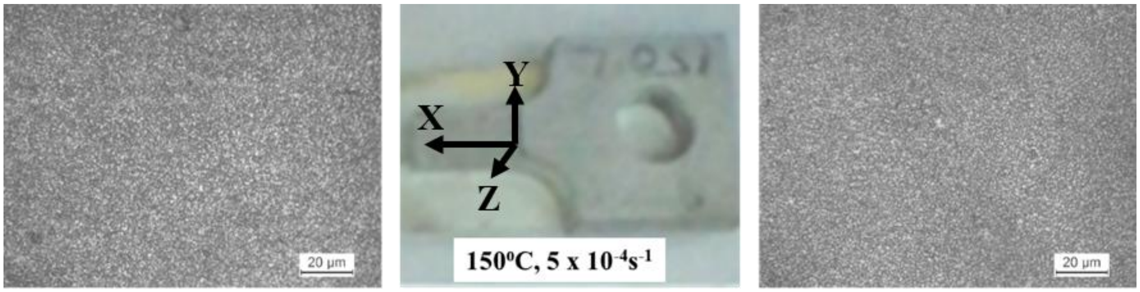

Fig. 8.8: Optical microstructure at the fractured tip and at grip of the sample tensile tested at 150 °C and at a strain rate of 5 × 10^{-4} s^{-1}.

In the previous chapter at discussion section 7.2.2, it was stated that GBS accommodated by grain rotation and grain boundary migration was the mechanism responsible for superplastic deformation in FSPed region. It contains argument of dynamic grain growth as the reason for strain hardening observed in the flow curve obtained at 350 °C. Hence, to confirm the occurrence of dynamic grain growth, the microstructure at the grip and fractured tip of the tensile tested sample were obtained. In the Fig.8.8, the optical microstructures, of the sample tensile tested at 150 °C ant at a strain rate of 5 × 10^{-4} s^{-1}, were obtained from the transvers section (XZ plane), at grip and at crack tip. The grains appeared like a clusters in both the microstructures due to very fine grain sizes of the order of 1 to 2 µm.

Similar microstructures were obtained from the samples tensile tested at 250°C (Fig. 8.9) and at 350 °C (Fig. 8.10). The microstructures at the grip section of the samples tested at 250 °C showed no difference in the microstructure which reveals no static grain growth at this temperature. However, at the strain rate of 1 × 10^{-3} s^{-1} and 5 × 10^{-4} s^{-1} the microstructure from tip region showed increase in average grain size to 4 µm which reveals the occurrence of dynamic grain growth. At 350 °C, increase in grain size to 2 µm and 4 µm was observed in the microstructures obtained at grip at the strain rate of 1 × 10^{-3} s^{-1} and 5 × 10^{-4} s^{-1} respectively. The corresponding grain sizes at the tip become 7 µm and 10 µm. It reveals that both static and dynamic grain growth had taken place at the samples tested at 350 °C.

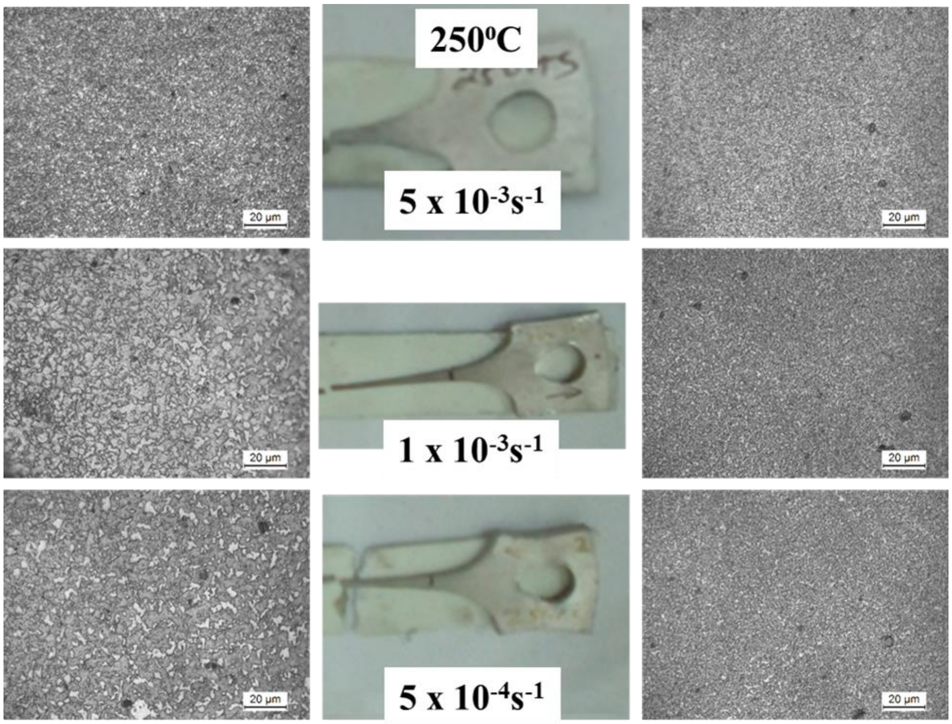

Fig. 8.9: Optical microstructures at the fractured tip and at grip of the samples tensile tested at 250 °C.

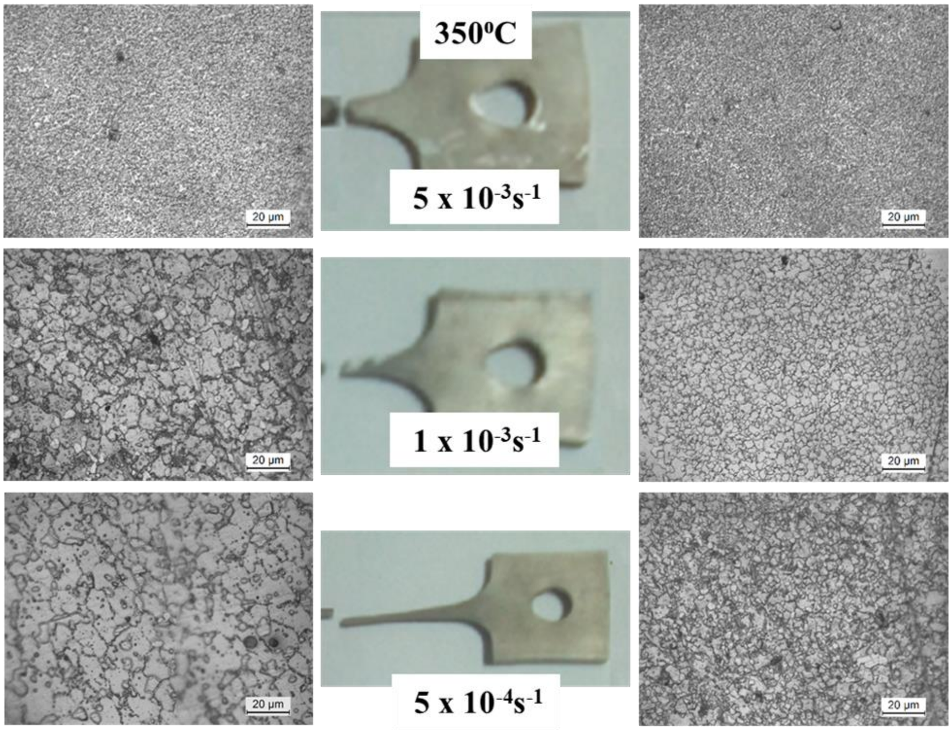

Fig. 8.10: Optical microstructures at the fractured tip and at grip of the samples tensile tested at 350 °C

The Q values also found to decrease with the increase in strain and n value followed similar variation as that of *m* value. At a strain rate of 5 x 10^{-3} s^{-1} the activation energy achieve a maximum at a true strain of 1 on both 250 ºC and 350 ºC. At the strain rate of 1 x 10^{-3} s^{-1} and 5 x 10^{-4} s^{-1} the activation energy almost decreases with strain, as seen in Table 8.1. There is no unique value of activation energy during the deformation. The reason could be due to several possibilities. One of the possibilities is the microstructural change in terms of dislocation activity, which influences the stress term in the numerator of eqn. 8.1 through a process of strain-hardening. These dislocations seem to be emanated from grain boundaries [270,271] because of large stress concentration developed due to grain-boundary sliding [272]. Small changes in the value of n as a function of strain also change the numerator of Eq. 8.1 significantly and can be correlated with the dislocation activity. The Q values at early stages of deformation are close to the activation energy of grain boundary diffusion in Mg alloys. Thus, GBS accommodated by slip activities were responsible for the dynamic grain growth and strain hardening behavior observed in the flow curves and causes the material parameters to vary with the strain. Further, static grain growth occurred at higher temperature (350 °C). Tripathi et al [273] observed bimodal grain sizes (elongated and equi-axed) after twin roll casting in AZ31 alloy. The microstructure remains stable up to an annealing temperature of 300 °C, however the grains become large and equi-axed at 500 °C. In this work also the microstructure was more stable during the deformation at 250 °C when compared to that at 350 °C which makes the material to exhibit maximum elongation of 818 % at 250 °C and at a strain rate of 1 x 10^{-3} s^{-1}.

8.3 Conclusions

The friction stir processed AZ91 Mg alloy was tensile tested at high temperatures in order to formulate a constitutive equation for superplastic deformation. The following conclusions were made,

- A constitutive equation for the superplasticity of FSPed AZ91 alloy was proposed.
- Maximum elongation of 818 % observed at 250 °C and at a strain rate of 1 x 10^{-3} s^{-1}.
- The material parameters were found to vary with the strain during superplastic deformation due to strain hardening at 250 °C and 350 °C.
- Grain boundary sliding accommodated by slip activities generated dynamic grain growth was the reason for strain hardening.

CHAPTER 9

CONCLUSIONS

AND

SUGGESTIONS FOR FUTURE WORK

CHAPTER 9

CONCLUSIONS & SUGGESTIONS FOR FUTURE WORK

This chapter details about the important findings made in the present research work and scope for future work.

Conclusions

In the present work, the hard to work as-cast AZ91 Mg alloy was chosen to search for improvement in its mechanical behavior by using friction stir processing method. Preliminary studies on the tensile and fracture toughness of the as-cast AZ91 Mg alloy was performed in as-cast, T4 and T6 conditions. The as-cast alloy was then multipass friction stir processed to modify its microstructure. The microstructural modifications were obtained by FSP using three tools, i.e., PL_4, PL_5 and PL_7 with different pin lengths 4 mm, 5mm and 7 mm respectively. The effect of these pin length on FSPed microstructures were studied. Three kinds of layered microstructure was developed through the thickness of the material, namely, i) FFG, ii) HFG and iii) SFG. The effect of these layered microstructures on the room temperature and high temperature mechanical behavior was studied. Finally, a constitutive equation was developed for the superplastic behavior of full thickness FSPed AZ91 Mg alloy.

The important conclusions from the work are as follows,

- Preliminary studies on the as-cast microstructure showed the microstructure of as-cast material contains 100 μm large, α-Mg matrix grains and network of brittle β phase. The β particles got dissolute in to α-Mg matrix after T4 solution treatment and re-precipitates during aging treatment after solutionizing (T6). The strength increased from 80 MPa in as-cast condition to 132 MPa in T4 and T6 conditions. Percentage elongation improved from 0.8% in as-cast to 4 % in T4 condition but further reduced to 2 % in T6 condition. The percentage elongation of the materials in as-cast, T4 and T6 conditions can be correlated with the cleavage facets, quasi-cleavage surfaces and river patterns from their respective fractographs. The fracture toughness of the material (J_{IC}) was also found to improve from 1.7 kJ/m^2 in as-cast condition to 4.2 kJ/m^2 in T6 condition. On further aging, J_{IC} value reduces to 3.1 kJ/m^2. The crack tip observed to followed intergranular crack path in T4 condition and transgranular in T6 condition. At the fatigue pre-crack region, crack bridging, an extrinsic toughening mechanism was observed due to the presence of precipitate particles but the intrinsic damage mechanism, i.e., segregation of α/β interface at crack tip determined the crack resistance behavior.

- The microstructure of the friction stir processed region contained grains with the average size of 0.8 μm and predominant basal texture slightly tilted towards process direction in the normal plane (XY plane). The effect of tool pin length (PL_4, PL_5 and PL_7) on the FSPed microstructure showed differences in the macrostructure of the processed regions but the difference in microstructural aspects, i.e., phase distribution, microstructure and its influence on mechanical properties were inconsequential. Semi-circular ring patterns was observed in the tools with pin length 5 mm (PL_5) and 7 mm (PL_7) due to the only pin effect, which was nullified in the FSPed region obtained using the tool with pin length 4 mm (PL_4) by the combined effect of both pin and shoulder of the tool.

- The effect of layered microstructures (FFG, HFG and SFG) on the room temperature mechanical properties showed that the FFG material exhibited superior tensile, fatigue and fracture behavior in comparison to AC, HFG and SFG materials. The strength of HFG and SFG materials, which contain different proportions of fine grain and as-cast microstructure, observed to follow the rule of mixture. Grain refinement with dissolved and broken up precipitates were primary reasons for improvement in tensile, fracture and fatigue characteristics of multipass FSPed AZ91 alloy and any proportion of as-cast microstructure is detrimental to room temperature mechanical properties.

- In the study of mechanical behavior of the layered microstructures at 350 °C also, FFG material displayed superplasticity at all tested strain rates with a maximum elongation of 680 % at the strain rate of 5×10^{-4} s^{-1}. The AC and HFG material showed improvement in ductility but failed to show any superplasticity while SFG material exhibited superplasticity at 1×10^{-3} s^{-1} and 5×10^{-4} s^{-1}. As-cast microstructure was detrimental, not only to room temperature properties but also to superplasticity, as it debonds easily at the interface of brittle interdendrites. FSPed region with the microstructure of fine grains and evenly distributed precipitates is favorable microstructure for superplastic elongation. Grain growth, change in texture from basal to random and decrease in the fraction of 30° grain boundary misorientation angle with the increasing deformation in FSPed region indicates that GBS accommodated by grain rotation and grain boundary migration is the deformation mechanism responsible for superplasticity.

- A constitutive equation for the superplasticity of FSPed AZ91 alloy was developed. The full thickness friction stir processed AZ91 Mg alloy was tensile tested at high temperatures (150 °C, 250 °C and 350 °C) and at three different strain rates (5×10^{-3} s^{-1}, 1×10^{-3} s^{-1} and 5×10^{-4} s^{-1}) at each temperature. The data obtained out of the test results were used to formulate a constitutive equation. The material parameters m, Q and n of the constitutive equation were found to vary with the strain during superplastic deformation. Grain boundary sliding accommodated by slip activities generated dynamic grain growth which causes strain hardening. The flow curves at 250 °C and at 350°C exhibited strain hardening behavior. This non steady-state behavior becomes reason for the variation of material parameters with the strain. The material showed maximum elongation of 818 % at 250 °C and at a strain rate of 1×10^{-3} s^{-1} due to grain stability at this test condition.

Suggestions for future work

The combination of different grain sized microstructure, either bimodal or layered microstructure, in Al alloys and few wrought Mg alloys was reported to exhibit superior mechanical properties when compared to the homogeneous fine grained microstructure. In this work also, the layered microstructure showed improvement in the mechanical properties but not superior to the fully fine grained microstructure. According to the results of this work, as-cast material in the layered microstructure was detrimental to the mechanical behavior of AZ91 Mg alloy at room temperature as well as at elevated temperature. Moreover, Mg is a low stacking fault energy material whereas Al alloys are comparatively high stacking fault energy materials. High stacking fault energy materials cross-slip easily and facilitate CDRX in case of Al alloys. For enhanced superplasticity in mixed grain size microstructure, the coarse grains in the microstructure should undergo microstructure evolution to become equiaxed, small grains through CDRX. It is not the case in present work, due to the presence of as-cast microstructure of AZ91 Mg alloy.

Therefore, the scope for the future works are as follows:

- Create layered microstructure in as-cast material using two or more sets of FSP parameters (rotation speed and traverse speed) will give different grain size regions. This will eliminate the detrimental as-cast microstructure from the layered microstructure. The effect of this layered microstructure without as-cast material can be studied.
- Comparative study can be performed on the deformation behavior of layered microstructure, generated by FSP in the materials, with high and low stacking fault energies (confirm the absence of as-cast region).
- Detailed deformation behavior in the layered microstructured material can be studied using Digital Image Correlation (DIC) maps and in-situ EBSD method.

References

[1] C. Berry, A Closer Look at Magnesium, 2015. http://www.zimtu.com/i/pdf/2015-07_ZR.pdf.

[2] Masaqui, Motor Vehicle Production 1950 to 2013, Wikimedia Commons. (2014). https://commons.wikimedia.org/wiki/File:Motor_Vehicle_Production_1950_2013.png (accessed October 12, 2017).

[3] Global Greenhouse Gas Emissions Data, United States Environ. Prot. Agency. (2016). https://www.epa.gov/ghgemissions/global-greenhouse-gas-emissions-data.

[4] Boeing, Current market outlook 2016-2035, (2016). http://www.boeing.com/resources/boeingdotcom/commercial/about-our-market/assets/downloads/cmo_print_2016_final.pdf

[5] M. Gupta, N. Gupta, Utilizing Magnesium based Materials to Reduce Green House Gas Emissions in Aerospace Sector, Aeron Aero Open Access. 1 (2017) 1–6. doi:10.15406/aaoaj.2017.01.00005.

[6] E.S.R.L. US Department of Commerce, NOAA, ESRL Global Monitoring Division - Global Greenhouse Gas Reference Network, (2017). https://www.esrl.noaa.gov/gmd/ccgg/trends/global.html (accessed October 16, 2017).

[7] A.A. Luo, Magnesium casting technology for structural applications, J. Magnes. Alloy. 1 (2013) 2–22. doi:10.1016/j.jma.2013.02.002.

[8] R. Brown, Future of Magnesium Developments in 21st Century, Mater. Sci. Technol. Conf. (2008).

[9] J.E. Hillis, The Effects of Heavy Metal Contamination on Magnesium Corrosion Performance, SAE Trans. 92 (1983) 553–559.

[10] Gupta M, Gupta N, The Promise of Magnesium Based Materials in Aerospace Sector History and Current Trends of Magnesium in Aerospace Sector, Int J Aeronaut. Aerosp. Res. Int. J. Aeronaut. Sci. Aerosp. Res. 4 (2017) 141–149.

[11] G.I. Taylor, Plastic strain in metals, Twenty-Eighth May Lect. to Inst. Met. (1938) 307–325.

[12] U.F. Kocks, Independent slip systems in crystals, Philos. Mag. 10 (1964) 187–193.

[13] R.E. von Mises, Mechanics of Plastic Shape Change of Crystals, J. Appl. Math. Mech. 8 (1928) 161-185.

[14] C.J. Bettles, M.A. Gibson, Current Wrought Magnesium Alloys: Strengths and Weaknesses, JOM. 57 (2005) 46–49.

[15] A. Dziubińska, A. Gontarz, M. Dziubiński, M. Barszcz, The Forming of Magnesium Alloy Forgings for Aircraft and Automotive Applications, Adv. Sci. Technol. Res. J. 10 (2016) 158–168.

[16] X. Zhang, Y. Chen, J. Hu, Recent advances in the development of aerospace materials, Prog. Aerosp. Sci. 97 (2018) 22–34.

[17] M. Madaj, M. Greger, V. Karas, Magnesium-alloy die forgings for automotive applications, Mater. Tehnol. 49 (2015) 267–273.

[18] A. H. Musfirah, A. G. Jaharah, Magnesium and Aluminum Alloys in Automotive Industry, J. Appl. Sci. Res. 8 (2012) 4865–4875.

[19] S. Fleming, An Overview of Magnesium based Alloys for Aerospace and Automotive Applications, (2012) 1–36.

[20] J.F. King, Magnesium: commodity or exotic? Mater. Sci. Technol. 23 (2007) 1–14.

[21] P.D. Caton, Magnesium- an old material with new applications, Mater. Des. 12 (1991) 137–139.

[22] D.S. Kumar, C.T. Sasanka, K. Ravindra, K.N.S. Suman, Magnesium and Its Alloys in Automotive Applications – A Review, American J. Mat. Sci. Tech, 4 (2015) 12–30.

[23] B. Mordike, T. Ebert, Magnesium, Mater. Sci. Eng. A. 302 (2001) 37–45.

[24] W.A. Monteiro, S.J. Buso, L. V Silva, Application of Magnesium Alloys in Transport, Provisional book chapter (1998) 1–14.

[25] N. Stanford, K. Sotoudeh, P.S. Bate, Deformation mechanisms and plastic anisotropy in magnesium alloy AZ31, Acta Materialia, 59 (2011) 4866-4874.

[26] T.B. Britton, F.P.E. Dunne, A.J. Wilkinson, On the mechanistic basis of deformation at the microscale in hexagonal close-packed metals, Proc. R. Soc. A, 471 (2015) 1-29.

[27] M.R. Barnett, N. Stanford, P. Cizek, A. Beer, Z. Xuebin, Z. Keshavarz, Deformation mechanisms in Mg alloys and the challenge of extending room-temperature plasticity, JOM. 21 (2009) 19-24.

[28] M. Liao, B. Li, M.F. Horstemeyer, Interaction Between Basal Slip and γ-Mg17Al12 Precipitate in Magnesium, 45 (2014) 3661–3669.

[29] C.H. Caceres, D.M. Rovera, Solid solution strengthening in concentrated Mg-Al alloys, J. Light Met. 1 (2001) 151–156.

[30] S. Celotto, T.J. Bastow, Study of precipitation in aged binary Mg-Al and ternary Mg-Al-Zn alloys using 27Al NMR spectroscopy, Acta Mater. 49 (2001) 41–51.

[31] D. Yu, D. Zhang, J. Sun, Y. Luo, J. Xu, Improving mechanical properties of ZM61 magnesium alloy by aging before extrusion, J. Alloys Compd. 690 (2017) 553–560.

[32] M. Mondet, E. Barraud, S. Lemonnier, J. Guyon, N. Allain, T. Grosdidier, Microstructure and mechanical properties of AZ91 magnesium alloy developed by Spark Plasma Sintering, Acta Mater. 119 (2016) 55–67.

[33] M. Qian, A. Das, Grain refinement of magnesium alloys by zirconium : Formation of equiaxed grains, Scr. Mater. 54 (2006) 881–886.

[34] U. Joshi, N. Hari Babu, The grain refinement potency of bismuth in magnesium, J. Alloys Compd. 695 (2017) 971–975.

[35] K. Kubota, M. Mabuchi, K. Higashi, Review Processing and mechanical properties of fine-grained magnesium alloys, J. Mater. Sci. 34 (1999) 2255–2262.

[36] T. Reguła, E. Czekaj, A. Fajkiel, K. Saja, M. Lech-grega, M. Bronicki, Application of heat treatment and hot extrusion processes to improve mechanical properties of the AZ91 alloy, 10 (2010) 141–146.

[37] J. A. Del Valle, M.T. Pérez-Prado, J.R. Bartolomé, F. Peñalba, O. A. Ruano, Grain Refinement in a Mg AZ91 Alloy via Large Strain Hot Rolling, Mater. Trans. 44 (2003) 2625–2630.

[38] S. Yang, W. Wu, D. Wang, Effect of Extrusion Speed on the Microstructure and Tensile Properties of AZ31 Alloy, MATEC Web of Conferences, 67, (2016) 1-8.

[39] C.W. Chung, R.G. Ding, Y.L. Chiu, W. Gao, Effect of ECAP on microstructure and mechanical properties of cast AZ91 magnesium alloy, J. Phys. Conf. Ser. 241 (2010) 012101.

[40] B. Chen, D.-L. Lin, L. Jin, X.-Q. Zeng, C. Lu, Equal-channel angular pressing of magnesium alloy AZ91 and its effects on microstructure and mechanical properties, Mater. Sci. Eng. A. 483–484 (2008) 113–116.

[41] K. Máthis, J. Gubicza, N.H. Nam, Microstructure and mechanical behavior of AZ91 Mg alloy processed by equal channel angular pressing, J. Alloys Compd. 394 (2005) 194–199.

[42] R. Kocich, M. Greger, Development of structure and mechanical properties in AZ91 alloy using by ARB process, Acta Metall. Slovaca. 3 (2005) 277–283.

[43] A.S.J. Al-Zubaydi, A.P. Zhilyaev, S.C. Wang, P.A.S. Reed, Superplastic behaviour of AZ91 magnesium alloy processed by high-pressure torsion, Mater. Sci. Eng. A. 637 (2015) 1–11.

[44] H.S. Nayaka, G.P. Chaudhari, B.S.S. Daniel, Grain Growth Kinetics of Accumulative Roll Bonded AZ61 Alloy, Adv. Mater. Res. 585 (2012) 387–391.

[45] A.P. Zhilyaev, T.R. McNelley, O.A. Ruano, Microstructure and Texture Evolution in Metals and Alloys during Intense Plastic Deformation, Mater. Sci. Forum. 715–716 (2012) 51–60.

[46] D. Yadav, R. Bauri, N. Chawake, Fabrication of Al-Zn solid solution via friction stir processing, Mater. Charact. 136 (2018) 221–228.

[47] A. Alavi Nia, S.H. Nourbakhsh, Microstructure and Mechanical Properties of AZ31/SiC and AZ31/CNT Composites Produced by Friction Stir Processing, Trans. Indian Inst. Met. 69 (2016) 1435–1442.

[48] B. Mordike, H. Friedrich, Magnesium Technology, Springer, Verlag Berlin Heidelberg, 2006.

[49] Serguei Erchov, Research on the Mechanical Properties of the Sand Cast Magnesium Alloy AZ91, (2001).

[50] T.J. Chen, R.Q. Wang, Y. Ma, Y. Hao, Semisolid Microstructure Evolution of AZ91D Magnesium Alloy Refined by Al-Ti-B, Mater. Res. 14 (2011) 532–540. doi:10.1590/S1516-14392011005000085.

[51] R. Zeng, Precipitation hardening in AZ91 magnesium alloy, (2013).

[52] M.S. Dargusch, K. Pettersen, K. Nogita, M.D. Nave, G.L. Dunlop, The Effect of Aluminium Content on the Mechanical Properties and Microstructure of Die Cast Binary Magnesium-Aluminium Alloys, Mater. Trans. 47 (2006) 977–982.

[53] Unal Ogun, Characterization of Tensile Deformation in AZ91 Mg Alloy Castings, (2016).

[54] E. Gariboldi, Toughness characteristics of as-die-cast AM60B alloy, Metall. Sci. Technol. 21 (2003) 16–24.

[55] M. Ahadlin Mohd Daud, M.Z. Selamat, Z. Sajuri, Plane Strain Fracture toughness Determination For magneSium alloy, J. Mech. Eng. Technol. 4 (2012) 45–51.

[56] S. Barbagallo, E. Cerri, Evaluation of the KIC and JIC fracture parameters in a sand cast AZ91 magnesium alloy, Eng. Fail. Anal. 11 (2004) 127–140.

[57] K. Purazrang, K.U. Kainer, B.L. Mordike, Fracture toughness behaviour of a magnesium alloy metal-matrix composite produced by the infiltration technique, Composites. 22 (1991) 456–462.

[58] D. Regener, G. Dietze, Crack Resistance Behaviour of Pressure Die Cast Magnesium Alloys, ECF14, Cracow (2002)

[59] E. Schick, D. Regener, Fracture mechanics testing of magnesium alloy ingots and die castings, ECF13, San Sebastian 2000. 42 (2013).

[60] M.O. Pekguleryuz, K.U. Kainer, A. Arslan Kaya, F. Witte, Fundamentals of Magnesium Alloy Metallurgy, (2013).

[61] S. Begum, D.L. Chen, S. Xu, A.A. Luo, Effect of strain ratio and strain rate on low cycle fatigue behavior of AZ31 wrought magnesium alloy, Mater. Sci. Eng. A. 517 (2009) 334–343.

[62] X.Z. Lin, D.L. Chen, Strain controlled cyclic deformation behavior of an extruded magnesium alloy, Mater. Sci. Eng. A. 496 (2008) 106–113.

[63] M. Kuffová, Fatigue Endurance of Magnesium Alloys, in: F. Czerwinski, Magnes. Alloy. - Des. Process. Prop., InTech, (2011) 129–162.

[64] H. Mohammad, M. Al, Composition and Microstructure Effects on Superplasticity in Magnesium Alloys, (2010).

[65] R.B. Figueiredo, S. Sabbaghianrad, A. Giwa, J.R. Greer, T.G. Langdon, Evidence for exceptional low temperature ductility in polycrystalline magnesium processed by severe plastic deformation, Acta Mater. 122 (2017) 322–331.

[66] V.N. Chuvil'deev, T.G. Nieh, M.Y. Gryaznov, V.I. Kopylov, A.N. Sysoev, Superplasticity and internal friction in microcrystalline AZ91 and ZK60 magnesium alloys processed by equal-channel angular pressing, J. Alloys Compd. 378 (2004) 253–257.

[67] V.N. Chuvil'deev, T.G. Nieh, M.Y. Gryaznov, A.N. Sysoev, V.I. Kopylov, Low-temperature superplasticity and internal friction in microcrystalline Mg alloys processed by ECAP, Scr. Mater. 50 (2004) 861–865.

[68] M. Furui, H. Kitamura, H. Anada, T.G. Langdon, Influence of preliminary extrusion conditions on the superplastic properties of a magnesium alloy processed by ECAP, Acta Mater. 55 (2007) 1083–1091.

[69] H.K. Lin, J.C. Huang, T.G. Langdon, Relationship between texture and low temperature superplasticity in an extruded AZ31 Mg alloy processed by ECAP, Mater. Sci. Eng. A. 402 (2005) 250–257.

[70] Y. Miyahara, Z. Horita, T.G. Langdon, Exceptional superplasticity in an AZ61 magnesium alloy processed by extrusion and ECAP, Mater. Sci. Eng. A. 420 (2006) 240–244.

[71] M. Kato, Hall-Petch Relationship and Dislocation Model for Deformation of Ultrafine-Grained and Nanocrystalline Metals, Mater.Trans. 55 (2014) 19–24.

[72] E.O. Hall, The Deformation and Ageing of Mild Steel: III Discussion of Results, Proc. Phys. Soc. Sect. B. 64 (2002) 747–753.

[73] N.J. Petch, The cleavage strength of polycrystals, J. Iron Steel Inst. 174 (1953) 25–28.

[74] R.W. Armstrong, 60 Years of Hall-Petch: Past to Present Nano-Scale Connections, Mater. Trans. 55 (2014) 2–12.

[75] J.A. del Valle, F. Carreño, O.A. Ruano, Influence of texture and grain size on work hardening and ductility in magnesium-based alloys processed by ECAP and rolling, Acta Mater. 54 (2006) 4247–4259.

[76] H. Somekawa, K. Nakajima, A. Singh, T. Mukai, Ductile fracture mechanism in fine-grained magnesium alloy, Philos. Mag. Lett. 90 (2010) 831–839.

[77] J. Pelleg, Mechanical Properties of Materials, Springer Netherlands, Dordrecht, (2013).

[78] A. Akhtar, E. Teghtsoonian, Solid solution strengthening of magnesium single crystals—ii the effect of solute on the ease of prismatic slip, Acta Metall. 17 (1969) 1351–1356.

[79] J.M. Rosalie, H. Somekawa, A. Singh, T. Mukai, The effect of size and distribution of rod-shaped β′ precipitates on the strength and ductility of a Mg–Zn alloy, Mater. Sci. Eng. A. 539 (2012) 230–237.

[80] J.M. Rosalie, H. Somekawa, A. Singh, T. Mukai, Effect of precipitation on strength and ductility in a Mg–Zn–Y alloy, J. Alloys Compd. 550 (2013) 114–123.

[81] S. Jain, A. Gokhale, J. Jain, S.S. Singh, K. Hariharan, Fatigue behavior of aged and solution treated AZ61 Mg alloy at small length scale using nanoindentation, Mater. Sci. Eng. A. 684 (2017) 652–659.

[82] P. Palai, N. Prabhu, P.D. Hodgson, B.P. Kashyap, Grain Growth and β-Mg17Al12 Intermetallic Phase Dissolution During Heat Treatment and Its Impact on Deformation Behavior of AZ80 Mg-Alloy, J. Mater. Eng. Perform. 23 (2014) 77–82.

[83] J.F. Nie, Effects of precipitate shape and orientation on dispersion strengthening in magnesium alloys, Scr. Mater. 48 (2003) 1009–1015.

[84] D. Duly, J.P. Simon, Y. Brechet, On the competition between continuous and discontinuous precipitations in binary Mg-Al alloys, Acta Metall. Mater. 43 (1995) 101–106.

[85] C.H. Caceres, C.J. Davidson, J.R. Griffiths, C.L. Newton, Effects of solidification rate and ageing on the microstructure and mechanical properties of AZ91 alloy, Mater. Sci. Eng. A. 325 (2002) 344–355.

[86] M.A. Gharghouri, G.C. Weatherly, J.D. Embury, J. Root, Study of the mechanical properties of Mg-7.7at.% Al by in-situ neutron diffraction, Philos. Mag. A. 79 (1999) 1671–1695.

[87] C.G. Schmidt, A.K. Miller, The effect of solutes on the strength and strain hardening behavior of alloys, Acta Metall. 30 (1982) 615–625.

[88] H. Dini, As-cast AZ91D Magnesium Alloy Properties- Effect of Microstructure and Temperature, (2015).

[89] T.Y.T. Su, Deformation twinning in magnesium using nano-indentation, (2013).

[90] M. Majkut, A study of deformation twinning in magnesium alloy AZ31B, (2013).

[91] P.A. Juan, Twinning in hexagonal materials: application to magnesium and zirconium, (2015).

[92] J. Jain, W.J. Poole, C.W. Sinclair, The deformation behaviour of the magnesium alloy AZ80 at 77 and 293 K, Mater. Sci. Eng. A. 547 (2012) 128–137.

[93] J. Jain, J. Zou, C.W. Sinclair, W.J. Poole, Double tensile twinning in a Mg-8Al-0.5Zn alloy, J. Microsc. 242 (2011) 26–36.

[94] D. Sun, M. Ponga, K. Bhattacharya, M. Ortiz, Proliferation of twinning in hexagonal close-packed metals: Application to magnesium, J. Mech. Phys. Solids. 112 (2018) 368–384.

[95] T. Tsuru, D.C. Chrzan, Effect of solute atoms on dislocation motion in Mg: An electronic structure perspective, Sci. Rep. 5, 8793 (2015) 1–8.

[96] M. Liao, B. Li, M.F. Horstemeyer, Interaction between prismatic slip and γ Mg17Al12 precipitate in magnesium, Comput. Mater. Sci. 79 (2013) 534–539.

[97] T.G. Langdon, Grain boundary sliding revisited: Developments in sliding over four decades, J. Mater. Sci. 41 (2006) 597–609.

[98] B.P. Kashyap, A. Arieli, A.K. Mukherjee, Microstructural aspects of superplasticity, J. Mater. Sci. 20 (1985) 2661–2686.

[99] J.A. del Valle, O.A. Ruano, Effect of Annealing Treatments on Strain Rate Sensitivity and Anisotropy in a Magnesium Alloy Processed by Severe Rolling, Mater. Sci. Forum. 638–642 (2010) 1524–1529.

[100] R.D. Doherty, D.A. Hughes, F.J. Humphreys, J.J. Jonas, D. Juul Jensen, M.E. Kassner, W.E. King, T.R. McNelley, H.J. McQueen, A.D. Rollett, Current issues in recrystallization: A review, Mater. Sci. Eng. A. 238 (1997) 219-274.

[101] E. Knauer, J. Freudenberger, T. Marr, A. Kauffmann, L. Schultz, Grain Refinement and Deformation Mechanisms in Room Temperature Severe Plastic Deformed Mg-AZ31, Metals (Basel). 3 (2013) 283–297.

[102] K. V Jata, S.L. Semiatin, Continuous dynamic recrystallization during friction stir welding of high strength aluminum alloys, Scr. Mater. 43 (2000) 743–749.

[103] K. Huang, R.E. Logé, A review of dynamic recrystallization phenomena in metallic materials, Mater. Des. 111 (2016) 548–574.

[104] J. Zrnik, S.V. Dobatkin, I. Mamuzic, Processing of metals by severe plastic deformation (spd) – structure and mechanical properties respond, Metalugija, 47 (2008) 211-216.

[105] W. Chengpeng, L. Fuguo, C. Bo, Y. Zhanwei, L. Hongya, Severe Plastic Deformation Techniques for Bulk Ul- trafine-grained Materials, Rare Met. Mater. Eng. 41 (2012) 941–946.

[106] R.. Mishra, M.. Mahoney, S.. McFadden, N.. Mara, A.. Mukherjee, High strain rate superplasticity in a friction stir processed 7075 Al alloy, Scr. Mater. 42 (1999) 163–168.

[107] W.M.W. Thomas, I. Norris, E.D. Nicholas, J.C. Needham, M.G. Murch, P. Temple-Smith, C.J. Dawes, Friction stir welding process developments and variant techniques, Google Patents. (1991) 1–21.

[108] R.S. Mishra, Z.Y. Ma, Friction stir welding and processing, Mater. Sci. Eng. R. 50 (2005) 1–78.

[109] R. Bauri, G.D.J. Ram, D. Yadav, C.N.S. Kumar, Effect of Process Parameters and Tool Geometry on Fabrication of Ni Particles Reinforced 5083 Al Composite by Friction Stir Processing, Mater. Today Proc. 2 (2015) 3203–3211.

[110] Y.N. Zhang, X. Cao, S. Larose, P. Wanjara, Review of tools for friction stir welding and processing, Can. Metall. Q. 51 (2012) 250–261.

[111] H. Fujii, L. Cui, M. Maeda, K. Nogi, Effect of tool shape on mechanical properties and microstructure of friction stir welded aluminum alloys, Mater. Sci. Eng. A. 419 (2006) 25–31.

[112] K. Elangovan, V. Balasubramanian, M. Valliappan, Effect of Tool Pin Profile and Tool Rotational Speed on Mechanical Properties of Friction Stir Welded AA6061 Aluminium Alloy Effect of Tool Pin Profile and Tool Rotational Speed on Mechanical Properties of Friction St, Mater. Manuf. Process. 23 (2008) 251–260.

[113] G. Padmanaban, V. Balasubramanian, Selection of FSW tool pin profile, shoulder diameter and material for joining AZ31B magnesium alloy – An experimental approach, Mater. Des. 30 (2008) 2647–2656.

[114] M.A. García-Bernal, R.S. Mishra, R. Verma, D. Hernández-Silva, Influence of friction stir processing tool design on microstructure and superplastic behavior of Al-Mg alloys, Mater. Sci. Eng. A. 670 (2016) 9–16.

[115] S. Mironov, Y. Motohashi, T. Ito, A. Goloborodko, K. Funami, R. Kaibyshev, Feasibility of Friction Stir Welding for Joining and Microstructure Refinement in a ZK60 Magnesium Alloy, (2007).

[116] N. Othman, M. Ishak, L. Shah, Effect of shoulder to pin ratio on magnesium alloy, in: IOP Conf. Ser. Mater. Sci. Eng., (2017).

[117] H. Patle, R. Dumpala, B. Ratna Sunil, Machining characteristics and corrosion behavior of grain refined AZ91 Mg alloy produced by Friction Stir Processing: Role of Tool Pin Profile, Trans. Indian Inst. Met. 71 (2018) 951-959.

[118] Y.-H. Zhao, S.-B. Lin, L. Wu, F.-X. Qu, The influence of pin geometry on bonding and mechanical properties in friction stir weld 2014 Al alloy, (2005).

[119] P. Sevvel, V. Jaiganesh, Impact of process parameters during friction stir welding of AZ80A Mg alloy, Sci. Technol. Weld. Join. 21 (2016) 83-90.

[120] N. Dialami, M. Cervera, M. Chiumenti, A. Segatori, W. Osikowicz, Experimental validation of an FSW model with an enhanced friction law: Application to a threaded cylindrical pin tool, Metals (Basel). 7 (2017) 1–14.

[121] A. Alavi Nia, H. Omidvar, S.H. Nourbakhsh, Investigation of the effects of thread pitch and water cooling action on the mechanical strength and microstructure of friction stir processed AZ31, Mater. Des. 52 (2013) 615–620.

[122] S.M. Chowdhury, D.L. Chen, S.D. Bhole, X. Cao, Tensile properties of a friction stir welded magnesium alloy: Effect of pin tool thread orientation and weld pitch, Mater. Sci. Eng. A. 527 (2010) 6064–6075.

[123] R. Johnson, Friction Stir Welding of Magnesium Alloys, Mater. Sci. Forum. 419–422 (2003) 365–370.

[124] E. Cerri, P. Leo, Effect of Friction Stir Processing on microstructure and mechanical properties of a HPDC magnesium alloy, Mater. Sci. F. 786 (2014) 1735–1740.

[125] C.I. Chang, C.J. Lee, J.C. Huang, Relationship between grain size and Zener–Holloman parameter during friction stir processing in AZ31 Mg alloys, Scr. Mater. 51 (2004) 509–514.

[126] F.Y. Lan, H.M. Chen, W.P. Guo, J. Zhang, Y.X. Jin, Effects of Friction Stir Processing on Mechanical Properties and Damping Capacities of AZ31 Magnesium Alloys, IOP Conf. Series: Materials Science and Engineering, 230 (2017) 1-5.

[127] A. Hütter, W. Huemer, C. Ramskogler, F. Warchomicka, A. Lachehab, R. Vallant, C. Sommitsch, Surface Modification of Pure Magnesium and Magnesium Alloy AZ91 by Friction Stir Processing, Key Eng. Mater. 651–653 (2015) 796–801.

[128] Y.N. Wang, C.I. Chang, C.J. Lee, H.K. Lin, J.C. Huang, Texture and weak grain size dependence in friction stir processed Mg–Al–Zn alloy, Scr. Mater. 55 (2006) 637–640.

[129] W.H. Loke, R. Ibrahim, S. Lathabai, Improving the Microstructure and Mechanical Properties of A Cast Mg- 9Al-1Zn alloy using Friction Stir Processing, (2016) 214–219.

[130] L.L. Hutsch, J. Hutsch, J.F. dos Santos, N. Huber, Increased room temperature formability of Mg AZ31 by high speed.pdf, Mater. Des. 54 (2014) 980–988.

[131] M.M. El-Rayes, E.A. El-Danaf, The influence of multi-pass friction stir processing on the microstructural and mechanical properties of Aluminum Alloy 6082, J. Mater. Process. Technol. 212 (2012) 1157–1168.

[132] S. Ramaiyan, U. Mani, R. Chandran, S. Kumar, Optimization of Corrosion Behavior in Submerged Friction Stir Processed Magnesium Az31B Alloy, in: Int. Mech. Eng. Congr. Expo., ASME, (2017) 1–9.

[133] L. Long, G. Chen, S. Zhang, T. Liu, Q. Shi, Finite-element analysis of the tool tilt angle effect on the formation of friction stir welds, J. Manuf. Process. 30 (2017) 562–569.

[134] P. Rey, D. Gesto, J. A. del Valle, D. Verdera, O. A. Ruano, Fine and Ultra-Fine Grained AZ61 and AZ91 Magnesium Alloys Obtained by Friction Stir Processing, Mater. Sci. Forum. 706–709 (2012) 1002–1007.

[135] A. Alavi Nia, H. Omidvar, S.H. Nourbakhsh, Effects of an overlapping multi-pass friction stir process and rapid cooling on the mechanical properties and microstructure of AZ31 magnesium alloy, Mater. Des. 58 (2014) 298–304.

[136] X. Luo, G. Cao, W. Zhang, C. Qiu, D. Zhang, Ductility Improvement of an AZ61 Magnesium Alloy through Two-Pass Submerged Friction Stir Processing, Materials (Basel). 10 (2017) 1–12.

[137] J. Shen, D. Wu, M.-B. Zhou, L. Cheng, J.-X. Sang, Development of liquid-nitrogen-cooling friction stir spot welding for AZ31 magnesium alloy joints, Int. J. Miner. Metall. Mater. 24 (2017) 1169–1176.

[138] P. Asadi, M.K. Besharati Givi, N. Parvin, A. Araei, M. Taherishargh, S. Tutunchilar, On the role of cooling and tool rotational direction on microstructure and mechanical properties of friction stir processed AZ91, Int J Adv Manuf Technol. 63 (2012) 987–997.

[139] M. Abbasi, B. Bagheri, M. Dadaei, H.R. Omidvar, M. Rezaei, The effect of FSP on mechanical, tribological, and corrosion behavior of composite layer developed on magnesium AZ91 alloy surface, Int. J. Adv. Manuf. Technol. 77 (2015) 2051–2058.

[140] S. Rouhi, M. Dadashpour, A. Mostafapour, A. Doniavi, Effects of multi-pass FSP on the β phase (Mg 17 Al 12) distribution and mechanical properties of AZ91C magnesium alloy, 82 (2017) 77–85.

[141] Y.S. Sato, S.H.C. Park, A. Matsunaga, A. Honda, H. Kokawa, Novel production for highly formable Mg alloy plate, J. Mater. Sci. 40 (2005) 637–642.

[142] J.-Q. Su, T.W. Nelson, C.J. Sterling, Friction stir processing of large-area bulk UFG aluminum alloys, Scr. Mater. 52 (2005) 135–140.

[143] M. Govindaraju, P.R. K, U. Chakkingal, K. Balasubramanian, Effect of Distance between Passes in Friction Stir Processing of Magnesium Alloy, Adv. Mater. Res. 585 (2012) 397–401.

[144] G. Venkateswarlu, D. Devaraju, M.J. Davidson, B. Kotiveerachari, G.R.N. Tagore, Effect of overlapping ratio on mechanical properties and formability of friction stir processed Mg AZ31B alloy, Mater. Des. 45 (2013) 480–486.

[145] A. Tripathi, A. Tewari, A.K. Kanjarla, N. Srinivasan, G.M. Reddy, S.M. Zhu, J.F. Nie, R.D. Doherty, I. Samajdar, Microstructural Evolution During Multi-Pass Friction Stir Processing of a Magnesium Alloy, Metall. Mater. Trans. A. 47 (2016) 2201–2216.

[146] R. Kumar, V. Pancholi, R.P. Bharti, Material flow visualization and determination of strain rate during friction stir welding, 255 (2018) 470–476.

[147] H.N.. Schmidt, T.. Dickerson, Hattel J.H, Material flow in butt friction stir welds in AA2024-T3, Acta Mater. 54 (2006) 1199–1209.

[148] P. Asadi, R.A. Mahdavinejad, S. Tutunchilar, Simulation and experimental investigation of FSP of AZ91 magnesium alloy, Mater. Sci. Eng. A. 528 (2011) 6469–6477.

[149] J. Gandra, R.M. Miranda, P. Vilaç, Effect of overlapping direction in multipass friction stir processing, Mater. Sci. Eng. A. 528 (2011) 5592–5599.

[150] Z.Y. Ma, A.L. Pilchak, M.C. Juhas, J.C. Williams, Microstructural refinement and property enhancement of cast light alloys via friction stir processing, Scr. Mater. 58 (2008) 361–366.

[151] A.H. Feng, Z.Y. Ma, Enhanced mechanical properties of Mg–Al–Zn cast alloy via friction stir processing, Scr. Mater. 56 (2007) 397–400.

[152] S. Kleiner, O. Beffort, P.J. Uggowitzer, Microstructure evolution during reheating of an extruded Mg–Al–Zn alloy into the semisolid state, Scr. Mater. 51 (2001) 405–410.

[153] B.M. Darras, M.K. Khraisheh, F.K. Abu-Farha, M.A. Omar, Friction stir processing of commercial AZ31 magnesium alloy, J. Mater. Process. Technol. 191 (2007) 77–81.

[154] J.D. Robson, S. Cui, Z.W. Chen, Incipient melting during friction stir processing of AZ91 magnesium castings, Mater. Sci. Eng. A. 527 (2010) 7299–7304.

[155] W. Yuan, S.K. Panigrahi, R.S. Mishra, Achieving High Strength and High Ductility in Friction Stir-Processed Cast Magnesium Alloy, Metall. Mater. Trans. A. 44 (2013) 3675–3684.

[156] D. Yadav, R. Bauri, Microstructure Development in Single and Double-Pass Friction Stir Processing of Aluminium, Mater. Sci. Forum. 753 (2013) 50–53.

[157] S.H.C. Park, Y.S. Sato, H. Kokawa, Microstructural evolution and its effect on Hall-Petch relationship in friction stir welding of thixomolded Mg alloy AZ91D, J. Mater. Sci. 38 (2003) 4379–4383.

[158] W. Zhang, J. Lu, W. Huo, Y. Zhang, Q. Wei, Microstructural evolution of AZ31 magnesium alloy subjected to sliding friction treatment, Philos. Mag. 98 (2018) 1576–1593.

[159] W. Zhang, Q. Wei, W.T. Huo, J.W. Lu, J.J. Hu, Y.S. Zhang, Dynamic recrystallization in nanocrystalline AZ31 Mg-alloy, Vaccum. 143 (2017) 236–240.

[160] D. Yadav, R. Bauri, Effect of friction stir processing on microstructure and mechanical properties of aluminium, Mater. Sci. Eng. A. 539 (2012) 85–92.

[161] D. Yadav, R. Bauri, Microstructural characterisation of friction stir processed aluminium, Mater. Sci. Technol. 27 (2011) 1163–1169.

[162] P. Asadi, M.K. Besharati Givi, M. Akbari, Simulation of dynamic recrystallization process during friction stir welding of AZ91 magnesium alloy, Int. J. Adv. Manuf. Technol. (2015).

[163] F. Chai, D. Zhang, Y. Li, W. Zhang, Microstructure evolution and mechanical properties of a submerged friction-stir-processed AZ91 magnesium alloy, J. Mater. Sci. 50 (2015) 3212–3225.

[164] A. Tripathi, A. Tewari, N. Srinivasan, G.M. Reddy, S.M. Zhu, J.F. Nie, R.D. Doherty, I. Samajdar, Microstructural Origin of Friction Stir Processed Zone in a Magnesium Alloy, Metall. Mater. Trans. A. 46 (2015) 3333–3336.

[165] J.A. del Valle, P. Rey, D. Gesto, D. Verdera, J.A. Jiménez, O.A. Ruano, Mechanical properties of ultra-fine grained AZ91 magnesium alloy processed by friction stir processing, Mater. Sci. Eng. A. 628 (2015) 198–206.

[166] A.H. Feng, B.L. Xiao, Z.Y. Ma, R.S. Chen, Effect of Friction Stir Processing Procedures on Microstructure and Mechanical Properties of Mg-Al-Zn Casting, Metall. Mater. Trans. A. 40 (2009) 2447–2456.

[167] A.M. Jamili, A. Zarei-Hanzaki, H.R. Abedi, P. Minárik, R. Soltani, The microstructure, texture, and room temperature mechanical properties of friction stir processed Mg-Y-Nd alloy, (2017).

[168] M. Vargas, S. Lathabai, P.J. Uggowitzer, Y. Qi, D. Orlov, Y. Estrin, Microstructure, crystallographic texture and mechanical behaviour of friction stir processed Mg-Zn-Ca-Zr alloy ZKX50, Mater. Sci. Eng. A. 685 (2017) 253–264.

[169] W. Woo, H. Choo, D.W. Brown, P.K. Liaw, Z. Feng, Texture variation and its influence on the tensile behavior of a friction-stir processed magnesium alloy, Scr. Mater. 54 (2006) 1859–1864.

[170] Z. Yu, H. Choo, Z. Feng, S.C. Vogel, Influence of thermo-mechanical parameters on texture and tensile behavior of friction stir processed Mg alloy, Scr. Mater. 63 (2010) 1112–1115.

[171] W. Woo, H. Choo, M. Prime, Z. Feng, B. Clausen, Microstructure, texture and residual stress in a friction-stir-processed AZ31B magnesium alloy, Acta Materialia, 56 (2008) 1701-1711.

[172] V. Jain, R.. Mishra, A.. Gupta, Gouthama, Study of β-precipitates and their effect on the directional yield asymmetry of friction stir processed and aged AZ91C alloy, Mater. Sci. Eng. A. 560 (2013) 500–509.

[173] V. Jain, W. Yuan, R.S. Mishra, Gouthama, A.K. Gupta, Directional Anisotropy in the Mechanical Behavior of Friction Stir Processed and Aged AZ91 Alloy, Mater. Sci. Forum. 702–703 (2011) 64–67.

[174] Y. Muto, K. Matsumoto, T. Shiraiwa, M. Enoki, Detection of Crack Propagation by AE and Evaluation of Fracture Toughness in Various Mg Alloys, J. Japan Inst. Met. Mater. 78 (2014) 381–387.

[175] X. Guo, K. Chang, L.Q. Chen, M. Zhou, Determination of fracture toughness of AZ31 Mg alloy using the cohesive finite element method, Eng. Fract. Mech. 96 (2012) 401–415.

[176] Y. Xia, L. Yulong, L. Li, Effect of grain refinement on fracture toughness and fracture mechanism in AZ31 magnesium alloy, 3 (2014) 1780–1785.

[177] M. Dadashpour, A. Mostafapour, R. Yeşildal, S. Rouhi, Effect of process parameter on mechanical properties and fracture behavior of AZ91C/SiO2 composite fabricated by FSP, Mater. Sci. Eng. A. 655 (2016) 379–387.

[178] H. Mayer, M. Papakyriacou, B. Zettl, S.E. Stanzl-Tschegg, Influence of porosity on the fatigue limit of die cast magnesium and aluminium alloys, Int. J. Fatigue. 25 (2003) 245–256.

[179] I. Serrano-Munoz, J.-Y. Buffiere, C. Verdu, Y. Gaillard, P. Mu, Y. Nadot, Influence of surface and internal casting defects on the fatigue behaviour of A357-T6 cast aluminium alloy, Int. J. Fatigue. 82 (2016) 361–370.

[180] A. Borbély, H. Mughrabi, G. Eisenmeier, H.W. Höppel, A finite element modelling study of strain localization in the vicinity of near-surface cavities as a cause of subsurface fatigue crack initiation, Int. J. Fract. 115 (2002) 227–232.

[181] Z. Xu, W. Wen, T. Zhai, Effects of Pore Position in Depth on Stress/Strain Concentration and Fatigue Crack Initiation, Metall. Mater. Trans. A. 43 (2012) 2763–2770.

[182] S. Sharma, Z.. Ma, R.. Mishra, Effect of friction stir processing on fatigue behavior of A356 alloy, Scr. Mater. 51 (2004) 237–241.

[183] A. Tajiri, Y. Uematsu, T. Kakiuchi, Y. Tozaki, Y. Suzuki, A. Afrinaldi, Effect of friction stir processing conditions on fatigue behavior and texture development in A356-T6 cast aluminum alloy, Int. J. Fatigue. 80 (2015) 192–202.

[184] D.R. Ni, D. Wang, A.H. Feng, G. Yao, Z.Y. Ma, Enhancing the high-cycle fatigue strength of Mg–9Al–1Zn casting by friction stir processing, Scr. Mater. 61 (2009) 568–571.

[185] P. Cavaliere, P.P. De Marco, Fatigue behaviour of friction stir processed AZ91 magnesium alloy produced by high pressure die casting, Mater. Charact. 58 (2007) 226–232.

[186] A. Afrinaldi, T. Kakiuchi, R. Itoh, Y. Mizutani, Y. Uematsu, The effect of friction stir processing and post-aging treatment on fatigue behavior of Ca-added flame-resistant magnesium alloy, Int J Adv Manuf Technol Mater. 95 (2017) 2379-2391.

[187] C. Wang, T.J. Luo, J.X. Zhou, Y.S. Yang, Anisotropic cyclic deformation behavior of extruded ZA81M magnesium alloy, Int. J. Fatigue. 96 (2017) 178–184.

[188] Y. Uematsu, K. Tokaji, K. Fujiwara, H. Shibata, Fatigue behaviour of cast magnesium alloy AZ91 microstructurally, Fatigue Fract. Eng. Mater. Struct. 32 (2009) 541–551.

[189] F. Chai, D. Zhang, W. Zhang, Y. Li, Microstructure evolution during high strain rate tensile deformation of a fine-grained AZ91 magnesium alloy, Mater. Sci. Eng. A. 590 (2014) 80–87.

[190] P. Cavaliere, P.P. De Marco, Friction stir processing of AM60B magnesium alloy sheets, Mater. Sci. Eng. A. 462 (2007) 393–397.

[191] V. Jain, R.S. Mishra, Gouthama, Superplastic behavior and microstructural stability of friction stir processed AZ91C alloy, J. Mater. Sci. 48 (2013) 2635–2646.

[192] C.H. Caceres, D.S. Wilkinson, Large strain behaviour of a superplastic copper alloy-II. Cavitation and fracture, Acta Metall. 32 (1984) 423–434.

[193] J.A. Valle, P. Rey, D. Gesto, D. Verdera, J.A. Jiménez, O.A. Ruano, Mechanical properties of ultra- fi ne grained AZ91 magnesium alloy processed by friction stir processing, Mater. Sci. Eng. A. 628 (2015) 198–206.

[194] M. Mabuchi, K. Ameyama, H. Iwasaki, K. Higashi, Low temperature superplasticity of az91 magnesium alloy with non-equilibrium grain boundaries, Acta Mater. 47 (1999) 2047–2057.

[195] W.J. Kim, S.J. Yoo, H.K. Kim, Superplastic microforming of Mg–9Al–1Zn alloy with ultrafine-grained microstructure, Scr. Mater. 59 (2008) 599–602.

[196] F. Chai, D. Zhang, Y. Li, W. Zhang, High strain rate superplasticity of a fine-grained AZ91 magnesium alloy prepared by submerged friction stir processing, Mater. Sci. Eng. A. 568 (2013) 40–48.

[197] H. Watanabe, T. Mukai, K. Ishikawa, K. Higashi, High-Strain-Rate Superplasticity in an AZ91 Magnesium Alloy Processed by Ingot Metallurgy Route, Mater. Trans. 43 (2002) 78–80.

[198] D. Zhang, S. Wang, C. Qiu, W. Zhang, Superplastic tensile behavior of a fine-grained AZ91 magnesium alloy prepared by friction stir processing, Mater. Sci. Eng. A. 556 (2012) 100–106.

[199] P. Cavaliere, P.P. De Marco, Superplastic behaviour of friction stir processed AZ91 magnesium alloy produced by high pressure die cast, J. Mater. Process. Technol. 184 (2007) 77–83.

[200] M. Mabuchi, T. Asahina, H. Iwasaki, K. Higashi, Experimental investigation of superplastic behaviour in magnesium alloys, Mater. Sci. Technol. 13 (1997) 825–831.

[201] R. Chen, J.. Blandin, M. Suery, Q. Wang, E. Han, Thermomechanical processing and superplasticity of AZ91 magnesium alloy, J. Mater. Sci. Technol. 20 (2004) 295–297.

[202] M. Mabuchi, K. Kubota, K. Higashi, Superplasticity in an AZ91 alloy extrusion processed from machined chips, J. Mater. Sci. Lett. 12 (1993) 1831–1832.

[203] Y.H. Wei, Q.D. Wang, Y.P. Zhu, H.T. Zhou, W.J. Ding, Y. Chino, M. Mabuchi, Superplasticity and grain boundary sliding in rolled AZ91 magnesium alloy at high strain rates, Mater. Sci. Eng. A. 360 (2003) 107–115.

[204] S. Fudetani, S. Mizunari, M. Katoh, M. Horihata, Y. Torisaka, M. Hirohashi, Superplastic Flow at Elevated Temperatures in As-Rolled AZ91 Sheet, ISIJ Int. 47 (2007) 1692–1698.

[205] B. Mansoor, A.K. Ghosh, Microstructure and tensile behavior of a friction stir processed magnesium alloy, Acta Mater. 60 (2012) 5079–5088.

[206] D. Witkin, Z. Lee, R. Rodriguez, S. Nutt, E. Lavernia, Al – Mg alloy engineered with bimodal grain size for high strength and increased ductility, Scr. Mater. 49 (2003) 297–302.

[207] M.S. Oskooie, H. Asgharzadeh, H.S. Kim, Microstructure, plastic deformation and strengthening mechanisms of an Al-Mg-Si alloy with a bimodal grain structure, J. Alloys Compd. 632 (2015) 540–548.

[208] Y. Wang, M. Chen, F. Zhou, E. Ma, High tensile ductility in a nanostructured metal, Nature. 419 (2002) 912–914.

[209] C.H. Cáceres, B.I. Selling, Casting defects and the tensile properties of an AlSiMg alloy, Mater. Sci. Eng. A. 220 (1996) 109–116.

[210] S. Begum, D.L. Chen, S. Xu, A.A. Luo, Low cycle fatigue properties of an extruded AZ31 magnesium alloy, Int. J. Fatigue. 31 (2009) 726–735.

[211] A. Perron, O. Politano, V. Vignal, Grain size , stress and surface roughness, Surf. Interface Anal. 40 (2008) 518–521.

[212] W.C. Liu, J. Dong, P. Zhang, A.M. Korsunsky, X. Song, W.J. Ding, Improvement of fatigue properties by shot peening for Mg-10Gd-3Y alloys under different conditions, Mater. Sci. Eng. A. 528 (2011) 5935–5944.

[213] K. Edalati, T. Masuda, M. Arita, M. Furui, X. Sauvage, Z. Horita, R.Z. Valiev, Room-Temperature Superplasticity in an Ultrafine-Grained Magnesium Alloy, Sci. Rep. 7 (2017) 2662.

[214] H. Watanabe, H. Tsutsui, T. Mukai, M. Kohzu, S. Tanabe, K. Higashi, Deformation mechanism in a coarse-grained Mg-Al-Zn alloy at elevated temperatures, Int. J. Plast. 17 (2001) 387–397.

[215] X. Wu, Y. Liu, Superplasticity of coarse-grained magnesium alloy, Scr. Mater. 46 (2002) 269–274.

[216] W. Fan, B.P. Kashyap, M.C. Chaturvedi, Effect of layered microstructure and its evolution on superplastic behaviour of AA 8090 Al-Li alloy, Mater. Sci. Technol. 17 (2001) 439–445.

[217] V. Pancholi, B. Kashyap, Effect of local strain distribution on concurrent microstructural evolution during superplastic deformation of Al–Li 8090 alloy, Mater. Sci. Eng. A. 351 (2003) 174–182.

[218] S. Pradeep, V. Pancholi, Superplastic Forming of Multipass Friction Stir Processed Aluminum-Magnesium Alloy, Metall. Mater. Trans. A. 45 (2014) 6207–6216.

[219] M. Álvarez-Leal, A. Orozco-Caballero, F. Carreño, O.A. Ruano, Superplasticity in a commercially extruded ZK30 magnesium alloy, Mater. Sci. Eng. A. 710 (2018) 240–244.

[220] A. Zindal, J. Jain, R. Prasad, S.S. Singh, Effect of pre-strain and grain size on the evolution of precipitate free zones (PFZs) in a Mg-8Al-0.5Zn alloy, Mater. Lett. 201 (2017) 207–210.

[221] A. Zindal, J. Jain, R. Prasad, S.S. Singh, P. Cizek, Correlation of grain boundary precipitate characteristics with fracture and fracture toughness in an Mg-8Al-0.5 Zn alloy, Mater. Sci. Eng. A. 706 (2017) 192–200.

[222] G. Vukelić, J. Brnić, J -Integral As Possible Criterion in Material Fracture Toughness Assessment, Eng. Rev. 31 (2011) 91–96.

[223] ASTM E1820, Standard Test Method for Measurement of Fracture Toughness, (2018) 1-55.

[224] G. Nicoletto, R.Konecna and A. Pirondi, Fatigue crack paths in coarse-grained magnesium, Fatigue Fract Engng Mater Struct (2005) 237–244.

[225] R.O. Ritchie, Mechanisms of fatigue-crack propagation in ductile and brittle solids, Int. J. Fract. 100 (1999) 55–83.

[226] R. Ritchie, J. Lankford, Small fatigue cracks: Mechaincs, mechanisms and applications, Elsevier science Ltd, Kidlington, UK (1986).

[227] D. Regener, G. Dietze, Fracture Toughness Behaviour of As-Cast and Long-Term Annealed Pressure Die Cast Magnesium Alloys, Magnesium. (2005) 396–401.

[228] G.R. Cui, Z.Y. Ma, S.X. Li, Periodical plastic flow pattern in friction stir processed Al–Mg alloy, Scr. Mater. 58 (2008) 1082–1085.

[229] W.W. Hu, Z.Q. Yang, H.Q. Ye, ⟨c+a⟩ dislocations and their interactions with other crystal defects in a Mg alloy, Acta Mater. 124 (2017) 372-382.

[230] G. Bhargava, W. Yuan, S.S. Webb, R.S. Mishra, Influence of texture on mechanical behavior of friction-stir-processed magnesium alloy, Metall. Mater. Trans. A Phys. Metall. Mater. Sci. 41 (2010) 13–17.

[231] A.H. Feng, Z.Y. Ma, Microstructural evolution of cast Mg–Al–Zn during friction stir processing and subsequent aging, Acta Mater. 57 (2009) 4248–4260.

[232] J.A. Del Valle, M.T. Pérez-Prado, O.A. Ruano, Deformation mechanisms responsible for the high ductility in a Mg AZ31 alloy analyzed by electron backscattered diffraction, Metall. Mater. Trans. A. 36A (2005) 1427–1438.

[233] S. Pradeep, V. Pancholi, Effect of microstructural inhomogeneity on superplastic behaviour of multipass friction stir processed aluminium alloy, Mater. Sci. Eng. A. 561 (2013) 78–87.

[234] S. Pradeep, S.K. Sharma, V. Pancholi, Microstructural and Mechanical Characterization of Friction Stir Processed 5086 Aluminum Alloy, Mater. Sci. Forum. 710 (2012) 253–257.

[235] S. Pradeep, S.K. Sharma, V. Pancholi, Influence of Friction Stir Processing Parameters on Anisotropic Behavior Property of 5086-O Aluminum Alloy, Mater. Sci. Forum. 702–703 (2011) 348–351.

[236] K.N. Ramesh, S. Pradeep, V. Pancholi, Multipass Friction-Stir Processing and its Effect on Mechanical Properties of Aluminum Alloy 5086, Metall. Mater. Trans. A. 43 (2012) 4311–4319.

[237] S. Swaminathan, K. Oh-Ishi, A.P. Zhilyaev, C.B. Fuller, B. London, M.W. Mahoney, T.R. McNelley, Peak stir zone temperatures during friction stir processing, Metall. Mater. Trans. A Phys. Metall. Mater. Sci. 41 (2010) 631–640.

[238] S.R. Agnew, C.N. Tom, Study of slip mechanisms in a magnesium alloy by neutron diffraction and modeling, Scr. Mater. 48 (2003) 1003–1008.

[239] N. Afrin, D.L. Chen, X. Cao, M. Jahazi, Strain hardening behavior of a friction stir welded magnesium alloy, Scr. Mater. 57 (2007) 1004–1007.

[240] N. Afrin, D.L. Chen, X. Cao, M. Jahazi, Microstructure and tensile properties of friction stir welded AZ31B magnesium alloy, Mater. Sci. Eng. A. 472 (2008) 179–186.

[241] H. Somekawa, H.S. Kim, A. Singh, T. Mukai, Fracture toughness in direct extruded Mg–Al–Zn alloys, J. Mater. Res. 22 (2007) 2598–2607.

[242] H. Somekawa, T. Mukai, Effect of grain refinement on fracture toughness in extruded pure magnesium, Scr. Mater. 53 (2005) 1059–1064.

[243] H. Somekawa, Y. Osawa, T. Mukai, Effect of solid-solution strengthening on fracture toughness in extruded Mg – Zn alloys, Scr. Mater. 55 (2006) 593–596.

[244] H. Somekawa, A. Singh, T. Mukai, Effect of precipitate shapes on fracture toughness in extruded Mg – Zn – Zr magnesium alloys, J. Mater. Res. 22 (2007) 965–973.

[245] A.A. Willoughby, Significance of Pop-In fracture toughness testing, Int. J. Fract. 30 (1986) 3–6.

[246] F. Cao, F. Xia, G. Xue, Hot tensile deformation behavior and microstructural evolution of a Mg–9.3Li–1.79Al–1.61Zn alloy, Mater. Des. 92 (2016) 44–57.

[247] F.P.E. Dunne, Inhomoneneity of microstructure in superplasticity and its effect on ductility, Int. J. Plast. 14 (1998) 413–433.

[248] V. Pancholi, A. Raja, K. Rohit, Deformation behavior of inhomogeneous layered microstructure, 879 (2017) 1437-1442.

[249] V. Pancholi, K. Rohit, A. Raja, Effect of Different Proportion of Coarse and Fine Grain Microstructure on Superplastic Forming Characteristics, Mater. Sci. Forum. 838–839 (2016) 528–533.

[250] S. Gourdet, F. Montheillet, A model of continuous dynamic recrystallization, Acta Mater. 51 (2003) 2685–2699.

[251] H. Hallberg, M. Wallin, M. Ristinmaa, Modeling of continuous dynamic recrystallization in commercial-purity aluminum, Mater. Sci. Eng. A. 527 (2010) 1126–1134.

[252] Q. Guo-Zheng, Characterization for Dynamic Recrystallization Kinetics Based on Stress-Strain Curves, in: P. Wilson (Ed.), Recent Dev. Study Recryst., InTech, London, UK, (2013) 61–88.

[253] M.A. Rust, R.I. Todd, Surface studies of Region II superplasticity of AA5083 in shear: Confirmation of diffusion creep, grain neighbour switching and absence of dislocation activity, Acta Mater. 59 (2011) 5159–5170.

[254] K. Sotoudeh, P.S. Bate, Diffusion creep and superplasticity in aluminium alloys, Acta Mater. 58 (2010) 1909–1920.

[255] A.J. Carpenter, A.R. Antoniswamy, J.T. Carter, L.G. Hector, E.M. Taleff, A mechanism-dependent material model for the effects of grain growth and anisotropy on plastic deformation of magnesium alloy AZ31 sheet at 450 °C, Acta Mater. 68 (2014) 254–266.

[256] D.S. Wilkinson, C.H. Caceres, Large strain behaviour of a superplastic copper alloy - 1. Deformation, Acta Metall. 32 (1984) 415–422.

[257] D.S. Wilkinson, C.H. Caceres, On the mechanism of strain-enhanced grain growth during superplastic deformation, Acta Metall. 32 (1984) 1335–1345.

[258] C.H. Cáceres, P. Lukáč, Strain hardening behaviour and the Taylor factor of pure magnesium, Philos. Mag. 88 (2008) 977–989.

[259] S. Kandalam, R.K. Sabat, N. Bibhanshu, G.S. Avadhani, S. Kumar, S. Suwas, Superplasticity in high temperature magnesium alloy WE43, Mater. Sci. Eng. A. 687 (2017) 85–92.

[260] H. Watanabe, T. Uesugi, Y. Takigawa, K. Higashi, Texture change during superplastic deformation in fine-grained magnesium alloys, Mater. Sci. Forum. 838–839 (2016) 59–65.

[261] M.K. Rao, A.K. Mukherjee, On the evaluation of parameters of the constitutive equation for 7475AI alloy, J. Mater. Sci. 22 (1987) 459–465.

[262] M. Kawasaki, T.G. Langdon, Review: achieving superplasticity in metals processed by high-pressure torsion, J. Mater. Sci. 49 (2014) 6487–6496.

[263] B.P. Kashyap, A.K. Mukherjee, Strain Effect on Stress-Strain Rate Relations of Superplastic IN744 Steel, in: Strength Met. Alloy. (ICSMA 6), Elsevier, 1982: pp. 707–712.

[264] M. Suery, B. Baudelet, Rheological and metallurgical discussion of superplastic behaviour, Rev. Phys. Appliquée. 13 (1978) 53–66.

[265] A. Smolej, B. Skaza, M. Fazarinc, Determination of the strain-rate sensitivity and the activation energy of deformation in the superplastic aluminium alloy Al-Mg-Mn-Sc RMZ – Mater. Geoenvironment. 56 (2009) 389–399.

[266] W. Backofen, G. Murty, S. Zehr, Evidence for diffusional creep with low strain rate sensitivity.Trans. Met. Soc. AIME. 242 (1968) 329.

[267] J. Hedworth, M.J. Stowell, The Measurement of Strain-Rate Sensitivity in Superplastic Alloys, J. Mater. Sci. 6 (1971) 1061–1069.

[268] O.A. Kaibyshev, B.V. Rodionov, R.Z. Valiev, Peculiarities of dislocation slip during superplastic deformation of Zn-Al alloys, Acta Metall. 26 (1978) 1877–1886.

[269] O.A. Kaibyshev, R.Z. Valiev, V. V. Astanin, On the nature of superplastic deformation, Phys. Status Solidi. 35 (1976) 403–413.

[270] L.E. Murr, Interfacial Phenomena in Metal and Alloys, Wiley-Blackwell, (1977).

[271] A. Tripathi, I. Samajdar, J.F. Nie, A. Tewari, Study of grain structure evolution during annealing of a twin-roll-cast Mg alloy, Mater. Charact. 114 (2016) 157–165.